Scuola dottorale di Ingegneria Sezione Scienze dell'Ingegneria Civile

XXVII
CICLO DEL CORSO DI DOTTORATO

Numerical Modeling of Hydro-acoustic Waves for a Tsunami Early Warning System

Nome e Cognome del dottorando firma
ALI ABDOLALI

Docente Guida/Tutor: Prof. firma
Leopoldo Franco
Giorgio Bellotti

Coordinatore: Prof. firma
Aldo Fiori

Collana delle tesi di Dottorato di Ricerca (For the Ph.D. Degree)
In Ingegneria Civile (In Civil Engineering)
Università degli Studi Roma Tre (Roma Tre University)
Tesi n° 49

Dedications

This work is dedicated to my parents, Fatemeh Sohrabpour and Ahmad Reza Abdolali. They always encouraged and supported me in my decisions, although it meant that I would be living far away on different continents.

Acknowledgements

I would like to thank my advisors Prof. Leopoldo Franco and Prof. Giorgio Bellotti not only for their guidance and support throughout the work on this thesis, but also for giving me the opportunity to work within a leading group of researchers in the framework of coastal engineering on highly demanding/challenging topics i.e. tsunami and wave energy. It was a great experience and changed my life in many positive ways.

I also thank Prof. James T. Kirby and Prof. Paolo Sammarco for their great contribution in my research. Their expertise, guidance, and feedback were much appreciated for the improvement of my work. Furthermore, I would like to thank Prof. Francesco Chierici for our constructive discussions on tsunami modeling and Prof. Frederic Dias and Dr. Emiliano Renzi for our wonderful cooperation on wave energy project.

I would like to thank my colleagues and friends at Roma Tre University (Pietro Prestininzi, Claudia Cecioni, Alessando Romano, Federico Lombardo, Antonio Zarlenga, Elisabetta Romano, Michele Di Lazzaro, Melkamu Alebachew Ali, Fiseha Behulu Muluneh and Saghy Saeid Tehrani) and at Center for Applied Coastal Research (CACR), University of Delaware (Babak Tehranirad, Mohammad Keshtpour, Zhen Cheng, Zheyu Zhou, Nick DiCosmo, Saeideh Banihashemi, Patricia Chardon, Morteza Derakhti, Yeulwoo Kim, Ryan Mieras, Aline Pieterse, Xiao Yu, Jack Puleo, Fenyan Shi and Jia-lin Chen) for their supports and encouragements.

I thank my parents (Fatemeh and Ahmadreza), my beloved brother and sisters (Atefeh, Hamed and Mahshad) and friends for their encouragement and help (Ali Samiei, Shahriar Mohammadizadeh, Mohammad Reza Mohammadizadeh, Morteza Jandaghi Alaee, Negin Nakhlimahal and Morvarid Mahmoodabadi). We had wonderful time in ancient Rome together. Funding for this work was provided by Italian Ministry for University and Scientific Research (MIUR) within research project FIRB

2008-FUTURO IN RICERCA (Design, construction and operation of the Submarine Multidisciplinary Observatory experiment SMO project). This research was also supported by National Institute of Geophysics and Volcanology (INGV).
Furthermore, I would like to express my gratitude to my friends at Ocean Network Canada for provision of the valuable data to test my model. Their kind invitation/hospitality to visit their unique deep sea observatory facilities and present my work for the most prestigious worldwide tsunami scientists leaded to a significant progress in my work. Finally, I would also like to express my sincere gratitude to Prof. Franco and Bellotti for their helpful comments on my dissertation.

Ali Abdolali

January 2015

Abstract

Tsunamigenic fast movements of the sea-bed generate pressure waves in weakly compressible sea water, namely hydro-acoustic waves, which travel at the sound celerity in water (about 1500 m/s). These waves travel much faster than the counterpart long free-surface gravity waves and contain significant information on the source. Measurement of hydro-acoustic waves can therefore anticipate the tsunami arrival and significantly improve the capability of Tsunami Early Warning Systems (TEWS). However, applications to real cases require detailed numerical modelling in order to clearly define the time series at point A due to a source at point B. Three-dimensional models are straightforward to use, but require unrealistic computational times when applied to large-scale geographical areas, i.e. they cannot be used for a systematic investigation on an oceanic scale of prediction. The problem is further complicated by the effects of compressible viscous sediment layer at the sea bottom, which have a deep influence on the hydroacoustic waves propagation over large distances. The present work provides the derivation of two numerical models suitable for hydro-acoustic waves simulation and the application of model on large scale domain. The Mild-Slope Equation in Weakly Compressible fluid (*Sammarco et al.*, 2013 and *Abdolali et al.*, 2014) is presented first. It reduces the computational problem from three to two dimensions, hence reducing dramatically the computational costs. Then the capabilities of the model is extended by including the effects of a sediment layer at the bottom (*Abdolali et al.*, 2015b). Finally, two applications to real bathymetries are presented. In the first, the model is applied to simulate the hydro-acoustic wave propagation in the central and eastern Mediterranean Sea, generated by two main destructive historical earthquakes: the 365 AD Crete event and the 1693 Sicily event (*Abdolali et al.*, 2014 and *Cecioni et al.*, 2015). In the second application the model is used to reproduce the 28 October 2012 7.8 Mw earthquake occurred

off the West coast of Haida Gwaii archipelago, Canada. For this event deep water field measurements are available for comparison *Abdolali et al.*, 2015a). On the basis of the numerical results for these real cases, several conclusions on the possible use of hydro-acoustic waves as support to Tsunami Early Warning Systems can be drawn.

Contents

1 Introduction **3**

2 Depth-Integrated Equation for Large Scale Modeling of Tsunami in Weakly Compressible Fluid for Rigid Bottom **7**

2.1 Hydro-acoustic Wave Model 8
2.2 Sample computations 14
2.3 Conclusions 15

3 Large-scale numerical modeling of hydro-acoustic waves generated by tsunamigenic earthquakes: Mediterranean Historical Events **17**

3.1 Mediterranean sea Historical Events 18
  3.1.1 Deep Sea Observatories in Mediterranean Sea 18
  3.1.2 The 365 west Crete scenario 23
  3.1.3 The 1693 east Sicily scenario 25
3.2 Conclusions 32

4 Hydro-acoustic and tsunami waves generated by the 2012 Haida Gwaii earthquake: modeling and in-situ measurements **35**

4.1 2012 Haida Gwaii earthquake: analysis of in situ observations 36
4.2 Numerical simulations 41
  4.2.1 Hydro-acoustic wave model 45
  4.2.2 Tsunami waves 52
4.3 Conclusions 57

5 Depth-Integrated Equation for Hydro-acoustic Waves with Bottom Damping **59**

5.1 The role of the sediment layer 60
5.2 The mild-slope equation for damped hydro-acoustic waves . . 62
    5.2.1 Governing equations 64
    5.2.2 Derivation of the mild slope equation 64
5.3 Sample computations 68
5.4 Conclusions 72

6 Stratified Sedimentary Layer role on Formation and Dissipation of Hydro-acoustic Waves 75
6.1 hydro-acoustic wave model for multi-layer system 75
6.2 Damping Behaviour 82
6.3 Conclusions 84

7 Summary 87
7.1 Conclusion Remarks 87
7.2 Future Outlook 88

Appendix A Dispersion Relation for One Layer System 91

Appendix B Dispersion Relation for Two Layers System 99

List of Figures

1.1 Results at x=50 km of a sample computation carried out using a three-dimensional flow solver. The propagation acts as a filter showing energy only at the propagating eigenmodes of the system. 4

2.1 Schematic view of fluid domain. 9
2.2 Free surface elevation time series at 50 km from the tsunamigenic source as they result from the three models. . . . 11
2.3 Free surface elevation time series at 100 km from the tsunamigenic source as they result from the three models . . . 12
2.4 Upper panel: computational domain. Lower panels: free surface elevation time series at 400 km from the tsunamigenic source as they result from the two models. 13

3.1 Mediterranean Sea bathymetry. Domain 1 and 2 represent the computational domain for scenario 365 west Crete and 1693 east Sicily respectively. Points CTS and CP are deep sea observatory stations at Catania (-2000 m) and Capo Passero (-3400 m) 19
3.2 Residual vertical sea bed dislocation, $\zeta_0(m)$, for the 365 west Crete earthquake (right) and 1693 east Sicily earthquake (left) as reconstructed by *Tonini et al.* (2011). 21
3.3 Water depth (h) and Residual sea-bed displacement (ζ_0) for the vertical section 1, which crosses the two CP and CTS stations for 1693 Eastern Sicily event. The arbitrary points A, B, C and D are shown in Figure 3.2. 22

3.4 Pressure time series (left column) and their frequency spectra (right column) at CTS (a; b) and at CP (c; d). Comparison between the solution of the 3-D reference model (upper plots) and the solution of the depth-integrated equation (lower plots). 24

3.5 Sea bed pressure spectra at point A (h=1990 m), B (h=2283 m), C (h=3401 m) and D (h=1950 m) of Figure 3.3. The dashed lines indicate the natural acoustic frequencies corresponding to observation depth while the solid lines represent the normal acoustic modes for the source depth. . . 26

3.6 Snapshots of the free surface (η) hydro-acoustic perturbation (a) and gravity wave (b) given by the 365 west Crete earthquake. t = 0 refers to the time of occurrence of the earthquake 28

3.7 Snapshots of the free surface (η) hydro-acoustic perturbation (a) and gravity wave (b) given by the 1693 Catania earthquake. t = 0 refers to the time of occurrence of the earthquake 30

3.8 The bottom pressure spectrogram at Catania Test Site point (upper panel) and at Capo Passero point (lower panel), resulting from the numerical solution of the depth-integrated Eq. (2.16) over the whole domain. Both plots are normalized divided by the maximum value (Scenario 365 west Crete). . . 31

3.9 The bottom pressure spectrogram at Catania Test Site point (upper panel) and at Capo Passero point (lower panel), resulting from the numerical solution of the depth-integrated Eq. (2.16) over the whole domain. Both plots are normalized divided by the maximum value (Scenario 1693 east Sicily). . . 33

4.1 a) Surface projection of the slip distribution. The red lines indicate major plate boundaries. Black star is the epicenter location. b) Cross-section of slip distribution. The strike direction of the fault plane is indicated by the black arrow. The slip amplitude are showed in color. Contours show the rupture initiation time in seconds. c) Residual vertical bottom displacement distributed on 180 subfaults. d) Visual representation of the focal mechanism derived from the estimated moment tensor. e) Moment Rate Function, describing the rate of moment release with time after earthquake origin. The plots are taken from National Earthquake Information Center (NEIC) of United States Geological Survey (USGS). 37

4.2 Bathymetry data of the west Canadian and USA coast (ETOPO1 data). The epicenter position is marked with a black star. The black dashed line delimits, together with the coastline, the domain of the numerical computations. 39

4.3 Bottom pressure records (black lines) measured at the three stations of Ocean Network Canada (N_{BC}, N_{89} and N_{27} from top (a), to bottom (c)) and the corresponding spectrum from (d) to (f), the pressure perturbation (blue lines) obtained by the vertical component of the sea-bed velocity during earthquake (equation 4.1). The black vertical dashed lines represent the computed arrival time at each stations from the earthquake epicenter of the hydro-acoustic signal traveling at c_s velocity. The red vertical dashed lines represent the characteristic gravitational wave frequency f_g and first hydro-acoustic mode $f^{(1)}$ 42

4.4 Vertical residual sea-bed displacement on the numerical domain. The points N_{27}, N_{89} and N_{BC} represent the Ocean Network Canada observatories location, the points D_{19} and D_{04} represent the DART Buoys locations and the points P_1, P_2 and P_3 represent the selected points in front of activated fault in deep sea. 44

4.5 Residual sea-bed displacement (ζ_0) and water depth (h_b) for the two vertical sections of Figure 4.4, which cross the 2012 Haida Gwaii earthquake epicenter with each of the two DART stations. As it can be noted the earthquake's horizontal extension for these sections is about 200 km. 45

4.6 Pressure time series (left column) and their frequency spectra (right column) at D_{19} (a, b) and at D_{04} (c, d). Comparison between the solution of the 3-D reference model (upper plots) and the solution of the depth-integrated equation (lower plots). 47

4.7 Sea bed pressure spectra computed solving the 3D wave equation. The panel (b) to (e) respectively refer to points A (h=1220 m), B (h=2916 m), C (h=2945 m) and D (h=2705 m) along the section reported in the upper panel (a). The dashed lines indicate the natural acoustic frequencies corresponding to observation depth while the solid lines represent the first acoustic mode for the minimum water depth between generation area and observation point. 48

4.8 Snapshots of the free surface (η) hydro-acoustic perturbation given by the 2012 Haida Gwaii earthquake. The three points identify the positions of the three Neptune stations, while the two crosses the positions of the DART stations. t = 0 refers to the time of occurrence of the earthquake. 49

4.9 Spectrograms of the bottom pressure normalized by dividing by maximum value (P/P_{max}). The first column refer to the in-situ bottom pressure recorded at N_{BC}, N_{89} and N_{27}; the second and third columns of plots refer to the simulated hydro-acoustic bottom pressure at the Neptune stations and at points P_1, P_2, P_3 depicted in Figure 4.4. 51

4.10 Maximum absolute values of the free surface (η_{max}) of the hydro-acoustic wave generated by the Haida Gwaii earthquake on October 28, 2012. 52

4.11 Pressure time series as measured by the NEPTUNE observatories (gray lines) and as calculated by the model for gravity wave (red lines). Panels (a), (b) and (c) correspond to N_{BC}, N_{89} and N_{27} respectively. t = 0 refers to the time of occurrence of the earthquake. 53

4.12 Pressure time series as measured at DART buoys (gray lines) and as calculated by the model for gravity wave (red lines). The panels (a) and (b) correspond to D_{19} and D_{04} stations respectively. t = 0 refers to the time of occurrence of the earthquake. 54

4.13 Snapshots of the free surface (η) gravity wave perturbation given by the 2012 Haida Gwaii earthquake. The three points identify the positions of the three Neptune stations, while the two crosses the positions of the DART stations. t = 0 refers to the time of occurrence of the earthquake. 56

5.1 schematic view of fluid domain 60

5.2 Bottom pressure records at a distance of $x = 96km$ from epicenter, results of a sample computation carried out using a 3D flow solver in a constant depth, $h = 2200m$, $a = 1000m$, $c = 1500m/s$, $c_s = 2000m/s$, $\rho = 1000kg/m^3$, $\rho_s = 1850kg/m^3$ for a unit source area with semi-length $b = 112km$ and rising time $\tau = 1\ s$, showing (a) Time series of a one layer compressible water model in light gray and a coupled model of compressible water and inviscid compressible sediment in black, $\mu = 0$, (b) the corresponding frequency spectrum of panel (a), (c) Time series of a one layer compressible water model with partial reflection boundary condition (Eq. 5.4) at bottom in light gray and a coupled model of compressible water and viscous compressible sediment, $\mu_s = 2 \times 10^8 Pas$, in black and (d) the corresponding frequency spectrum of panel (c). The vertical dashed lines at panels (b) and (d) represents the frequency peaks calculated by Eqs. (5.1) and (5.2) in light gray and black respectively. 63

5.3 Results for the free surface elevation time series at 96 km from tsunamigenic source from 3D (light gray) and depth integrated (black) models in a constant depth, $h_p = 2200m$, $a = 1000m$, $c = 1500m/s$, $c_s = 2000m/s$, $\rho = 1000kg/m^3$, $\rho_s = 1850kg/m^3$, for a unit source area with semi-length $b = 112km$ and rising time $\tau = 1\ s$. (a, b) Time series and corresponding spectra of free surface elevation where $\mu_s = 0$ and (c, d) $\mu_s = 2 \times 10^8 Pas$ with $\gamma_1 = \omega_1/2\pi = 0.15Hz$. 69

5.4 The case of varying sea bottom and sediment thickness with tsunamigenic source at shallower part. (a) The computational domain. Results for the free surface elevation time series at 400 km from tsunamigenic source from 3D (light gray) and depth integrated models (black), $c = 1500 m/s$, $c_s = 2000 m/s$, $\rho = 1000 kg/m^3$, $\rho_s = 1850 kg/m^3$ and $\mu_s = 0$ for a unit source area with semi-length $b = 15 km$ and rising time $\tau = 1\ s$. (b, c) Results for impermeable sea bottom and (d, e) for coupled model. 71

5.5 The case of varying sea bottom and sediment thickness with tsunamigenic source at deeper part. (a) The computational domain. Results for the free surface elevation time series at point A, 100 km from tsunamigenic source at 3.5 km water depth (black) and point B, 400 km from tsunamigenic source at 2 km water depth (light gray) obtained from depth integrated models. The water and sediment characteristics are the same as Fig. 5.4. (b, c) results for impermeable sea bottom and (d, e) for coupled model. 73

6.1 Schematic view of fluid domain. 76

6.2 Rising mechanism starting at $t = t_0$ for period of τ with residual displacement of ζ_0. (a) Bottom displacement time series. (b) bottom velocity time series. 77

6.3 Results for the free surface elevation time series (left column) and their relative frequency spectra (right column) at a distance of $x = 96\ km$ from epicenter, results of a sample computation carried out using a 3D flow solver with computation parameters reported in Tab. 6.1. Panels show the case of (a, b) no sedimentary layer, $i = 0$, compressible water model with rigid bottom; (c, d) a coupled model of compressible water and a viscous compressible sediment, $i = 1$, $\mu_s^{(1)} = 0$; (e, f) a coupled model of compressible water and two viscous compressible sedimentary layers, $i = 2$, $\mu_s^{(1,2)} = 0$. The vertical dashed lines at the right column of panels represent the peak frequencies $f^{(n)}$ calculated by Eq. (6.8) at panel (b), $\gamma_1^{(n)}$ calculated by Eq. (6.9) at panel (d) and $\gamma_2^{(n)}$ calculated by Eq. (6.10) at panel (f). 79

6.4 Time series of free surface elevation normalized by the maximum value (η/η_{max}) for the case of $h = 2200\ m$ water column overlying a single sedimentary layer ($a^{(1)} = 1000\ m$). The other parameters are $c = 1500\ m/s$, $c_s^{(1)} = 2000\ m/s$, $\rho = 1028\ kg/m^3$, $\rho_s^{(1)} = 1850\ kg/m^3$ and $\mu_s^{(1)} = 2 \times 10^8$ for a unit source area with semi-length $b = 112\ km$ and rising time $\tau = 2\ s$. Blue dots represent temporal variation of the peak amplitudes. Red line is the fitting curve representing an exponential function ($e^{-\theta\omega t}$). 81
6.5 Variation of peak frequencies for different damping term (ϵ). The light gray dashed lines represent the natural modes for rigid bottom $f^{(n)}$ and two layered system $\gamma_1^{(n)}$ shown in Tab.6.2. 83
6.6 Variation of dimensionless damping rate θ as is shown in Fig. 6.4 for different damping terms ϵ. 85

A.1 Dispersion relation for β real greater that zero 93
A.2 Dispersion relation for β imaginary, $\beta = i\bar{\beta}$ 95

List of Tables

3.1 Magnitude M_w and seismic moment M_0 for the two scenarios as determined by *Tonini et al.* (2011) 20
3.2 Seismic parameters of 365 west Crete earthquake, as reconstructed by *Tonini et al.* (2011), for the North segment 1 and South segment 2 shown in Figure 3.2. 23
3.3 Seismic parameters of the 1693 east Sicily earthquake, as reconstructed by *Tonini et al.* (2011), for the four segments from North to South shown in Figure 3.2. 23

6.1 Sample computation parameters 80
6.2 Spectral peak frequencies for $i = 0, 1, 2$ sedimentary layer(s) given by Eqs. 6.8, 6.9 and 6.10, relative to the first three hydro-acoustic modes 80

Chapter 1

Introduction

A sudden movement of the seabed, triggered by underwater earthquakes, compresses the water column generating long gravity waves (tsunami) which can travel for long distances and are known for their dramatic effects on coastal areas. Aside from tsunami waves, pressure waves (hydro-acoustic waves), which oscillate between the sea-bed and the free-surface are generated due to the compressibility of sea water. These low-frequency waves are precursors of tsunamis, since their propagation speed, i.e. sound velocity in water, is significantly larger than that of the long gravity waves and contain significant information on the source. Via proper inversion technique, it can be possible to interpret the time series of low frequency pressure waves at point A due to a source at point B and subsequently estimate following tsunami waves.

In addition to the motivation for enhancement of available Tsunami Early Warning Systems (TEWS) performance, a correct modeling of the wave field generated by sea-bed movement is mandatory to understand the physics of the tsunami and its propagation. Most of the hydraulic tsunami models make use of the water incompressibility hypothesis. Therefore, considering the compressibility of water especially in the very early stages of generation process can improve our understanding and accuracy of tsunami models. Consider a sample computation carried out using a full three dimensional solver in a constant depth domain, where an earthquake is modelled as a unit sudden elevation of the sea bottom. The results are depicted in Figure 1.1, which shows the free surface elevation η and the corresponding frequency spectrum of the ocean at 50 km from the earthquake. Hydro-acoustic waves reach the point about 40 s after the initial time of bottom movement while

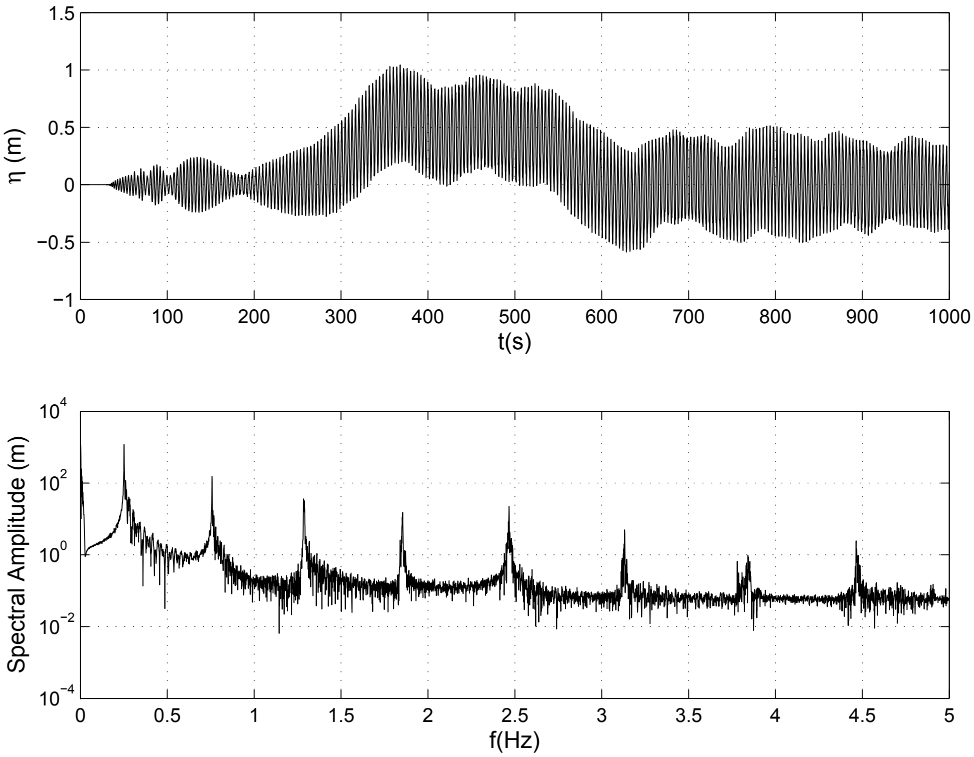

Figure 1.1: Results at x=50 km of a sample computation carried out using a three-dimensional flow solver. The propagation acts as a filter showing energy only at the propagating eigenmodes of the system.

tsunami arrives almost 300 s later. Hydro-acoustic waves appear to exist at some narrow frequency bands, with peaks at the cut-off modal frequencies given by *Stiassnie* (2010) which will be discussed later in chapter 2.

State of the art of tsunami warning procedures currently relies on seismic and sea level measurements. Nevertheless seismic networks may lead to issue warnings, that can be later canceled by the sea level records. The near-field prediction of tsunami propagation is challenging, given the limited time to spread the alarm: it is therefore unfeasible to wait the measurement of the tsunami itself before spreading the alert. The records of the faster hydro-acoustic waves can cope with the shortening decision time of spreading the alarm (*Cecioni et al.*, 2014).

The correct detection of hydro-acoustic waves can therefore significantly enhance the efficiency and promptness of TEWS. However, a well understanding of hydro-acoustic wave characteristics is needed to ensure the application of this method for TEWS design, i.e. Inherently, hydro-acoustic waves cannot propagate upslope. Therefore, measurement should be done in the deep sea in order to avoid depth effects on arriving signals (*Abdolali et al.*, 2014). Recent advances in deep sea observatory technologies provides a unique opportunity to study hydro-acoustic waves.

The idea of using measurements of hydro-acoustic waves for tsunami alert purpose, dates back to the work of *Ewing et al.* (1950). The idea was to provide of an additional component of the warning process for the following tsunami. Hydro-acoustic waves are expected to leave a measurable signature on bottom-pressure records (*Hendin and Stiassnie*, 2013). i.e. Hydro-acoustic waves helped to identify 1998 Papua New Guinea tsunami source as a landslide (*Synolakis et al.*, 2002).

The earlier studies on the tsunami evolution in weakly compressible water have been carried out by *Miyoshi* (1954), *Sells* (1965) and *Yamamoto* (1982). Later, analytical studies have solved the potential fluid problem in weakly compressible water, with fast rising motion of the sea bed (*Nosov*, 1999; *Stiassnie*, 2010; *Chierici et al.*, 2010), clarifying that there exists a relationship between the tsunamigenic source and the hydro-acoustic waves (*Chierici et al.*, 2010). *Stiassnie* (2010) found an analytical expression for the case of a rigid constant seabed. Later on, *Kadri and Stiassnie* (2012) analyzed pressure wave propagation for the case of a step-like discontinuity. Besides the work on pressure waves resulting from tsunamigenic ground motions, *Renzi and Dias* (2014) have proposed a theory for hydro-acoustic waves generated by surface pressure disturbances by storms. The analytical models, although extremely useful to investigate the features of hydro-acoustic wave generation and propagation processes, are not suited for reproduction of such phenomena at real-geographical scale.

Experimental registration of low-frequency hydro-acoustic waves generated by the sea-bed motion, has been measured during the Tokachi-Oki 2003 tsunami event (*Nosov et al.*, 2007), by the JAMSTEC (Japan Agency for Marine-earth Sciences and TEChnology) observatory. *Nosov and Kolesov* (2007) and *Bolshakova et al.* (2011) have processed the in-situ bottom pressure records in order to estimate amplitude, duration and velocity of bottom displacement. Simulation of hydro-acoustic waves in realistic domains requires the use of an arbitrary seabed geometry $h(x, y, t)$. *Nosov*

and Kolesov (2007) have used a detailed three-dimensional (3D) numerical model to study the Tokachi Oki 2003 tsunami event. Three-dimensional models (*Nosov and Kolesov*, 2007) are straightforward to use, but require unrealistic computational times when applied to large-scale geographical areas, i.e. they cannot be used for a systematic investigation on an oceanic scale of prediction. Hence the necessity of a two-dimensional model, that can retain all the physical features, yet at the same time be the basis of an efficient prediction tool. The 2D model therefore can overcome the computational difficulties of three-dimensional models.
This manuscript is structured as follows:

To start with, derivation of a hyperbolic mild slope equation for weakly compressible fluid (MSEWC) with rigid bottom assumption is described in chapter 2. The MSEWC could be able to overcome computational difficulties and limits of analytical solutions. The model was successfully verified against a 3D numerical model and the analytical solution of *Stiassnie* (2010). The contents of this chapter are also reported in *Sammarco et al.* (2013).

In chapter 3, the MSEWC has subsequently been used to simulate hydro-acoustic wave fields over real bathymetry for two historical catastrophic earthquake scenarios in the Mediterranean Sea. The outcomes of this work provided suggestions for deep sea observatory in Mediterranean Sea. The contents of this chapter are published in *Cecioni et al.* (2015) and *Abdolali et al.* (2014).

In chapter 4, the MSEWC has been used to reproduce the 28 *October* 2012 7.8 Mw earthquake occurred off the West coast of $Haida\ Gwaii$ archipelago, $Canada$. For this event, deep water field measurements were available for comparison. The contents of this chapter are reported in *Abdolali et al.* (2015a).

Although the MSEWC was able to reproduce tsunami wave field satisfactorily, there were still discrepancies for hydro-acoustic waves. In chapter 5, the underlying viscous sedimentary layer is taken into account and the hyperbolic mild slope equation for dissipative weakly compressible fluids (MSEDWC) is derived. The content of this chapter is reported in *Abdolali et al.* (2015b).

In chapter 6, the role of stratified sedimentary layers on the formation, propagation and dissipation of hydro-acoustic waves is investigated. The contents of this chapter are reported in *Abdolali et al.* (2015c).

The thesis ends with a summary and future outlook in Chapter 7.

Chapter 2

Depth-Integrated Equation for Large Scale Modeling of Tsunami in Weakly Compressible Fluid for Rigid Bottom

In this chapter, a depth-integrated equation for the mechanics of propagation of low frequency hydro-acoustic waves due to a sudden bottom displacement associated to earthquakes is presented. The model equation can be used for numerical prediction in large scale domains, overcoming computational difficulties of three dimensional models and so creating a solid base for Tsunami Early Warning Systems.

The numerical model proposed is based on the solution of the 2DH Mild Slope Equation in Weakly Compressible fluid over a rigid bottom (MSEWC), proposed by *Sammarco et al.* (2013).

The chapter is structured as follows: Section 2.1 describes the mathematical formulation of weakly compressible mild slope equation for rigid bottom. Section 2.2 describes the validation of MSEWC in comparison with analytical formula, valid for constant depth and fully three dimensional model for varying bottom through sample computations. In Section 2.3 discussions and conclusions are given.

2.1 Hydro-acoustic Wave Model

Consider the problem of wave propagation in a weakly compressible inviscid fluid over a mild varying sea bottom as shown in Fig. 2.1, where waves are generated by a moving bottom. The seabed vertical distance from the mean water level $z = 0$ as a function of horizontal coordinates and time is shown by $z = -h(x, y, t)$. The continuity and momentum within fluid can be written as:

$$\begin{cases} \frac{\partial\rho}{\partial t} + \nabla \cdot (\rho \vec{U}) = 0 \\ \frac{\partial\vec{U}}{\partial t} + \vec{U}\nabla \cdot \vec{U} = -\frac{1}{\rho}\nabla P - \vec{g} \end{cases}, \tag{2.1}$$

Where ρ is fluid density, $\vec{U}$ fluid velocity vector, P pressure, ν the kinematic viscosity and ν_s second viscosity. ∇ and ∇^2 are respectively the gradient and the Laplacian and g is the gravity acceleration. Assume that the fluid density (ρ) is sum of a constant density ρ_0 and a perturbation $\rho_1 << \rho_0$ and the fluid is barotropic:

$$\begin{cases} \rho = \rho_0 + \rho_1 \\ P(\rho) = P(\rho_0) + c_s^2\rho_1 + O(\rho_1{}^2) \end{cases}, \tag{2.2}$$

where $c_s = \partial P/\partial\rho$ is sound speed in the fluid. Neglecting second order terms, in the framework of irrotational fluid, Eq. (2.1) can be written in term of fluid velocity potential ($\vec{U} = \nabla\phi$) as:

$$\begin{cases} \frac{\partial\rho_1}{\partial t} + \rho_0\nabla^2\phi = 0 \\ \phi_t + \frac{\rho_1}{\rho_0}c_s^2 + gz = C(t), \end{cases} \tag{2.3}$$

Combining the time derivative of momentum with continuity, we obtain the weakly compressible wave equation in water. The free surface, bottom and outgoing boundary conditions are:

$$\begin{cases} \phi_{tt} - c_s^2\nabla^2\phi - c_s^2\phi_{zz} = 0 & \\ \phi_{tt} + g\phi_z = 0 & \text{at} \quad z = 0 \\ \phi_z + \nabla h \cdot \nabla\phi + h_t = 0 & \text{at} \quad z = -h\,(x, y, t) \\ \nabla_h\phi + \frac{1}{c_s}\phi_t = 0 & \text{at} \quad x = L \end{cases} \tag{2.4}$$

where subscripts with the independent variables denotes partial derivatives. The waves must also be outgoing at infinity (L).

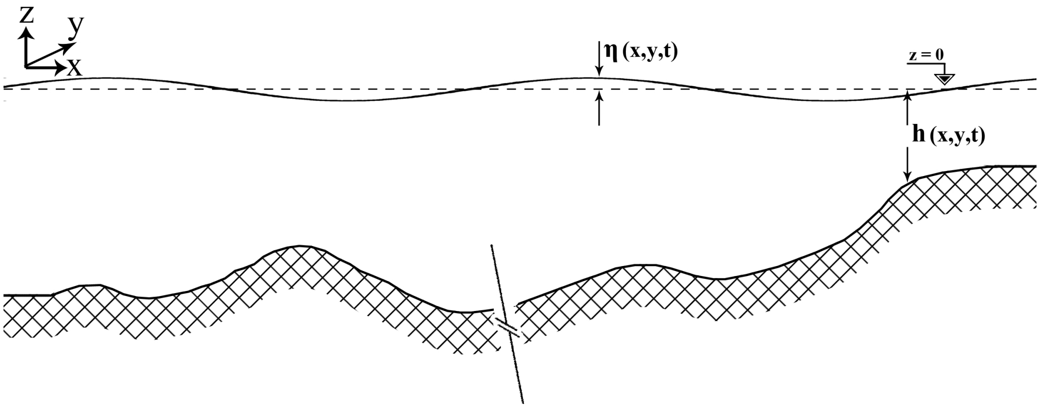

Figure 2.1: Schematic view of fluid domain.

Expanding in a series of orthogonal functions $f_n(z)$, the classic eigenfunctions of the constant depth homogeneous problem, but with the local depth $h = h\,(x, y, t)$:

$$f_n(z) = \frac{\cosh\left[\beta_n\left(h + z\right)\right]}{\cosh\left(\beta_n h\right)}, \tag{2.5}$$

where the β_n's are the roots of the dispersion relation

$$\beta_n = \begin{cases} n = 0 & \beta_n = \beta_0 \quad \omega^2 = g\beta_0 \tanh\left(\beta_0 h\right) \\ n \geq 1 & \beta_n = i\bar{\beta_n} \quad \omega^2 = -g\bar{\beta_n} \tan\left(\bar{\beta_n} h\right). \end{cases} \tag{2.6}$$

Derivation of dispersion relation for weakly compressible sea with rigid bottom is described in Appendix 1.

Indeed, the hypothesis of a mild slope allows us to seek the solution in the form:

$$\phi\left(x, y, z, t\right) = \sum_{n=0}^{\infty} \phi_n\left(x, y, z, t\right) = \sum_{n=0}^{\infty} \psi_n\left(x, y, t\right) f_n\left(z\right). \tag{2.7}$$

The forcing bottom displacement in term of eigenfunctions $f_n(z)$ can be rewritten as:

$$h\left(x, y, t\right) = \sum_{n=0}^{\infty} h_n\left(x, y, t\right) f_n\left(z\right) \quad \text{for any } z \in [-h, 0] \tag{2.8}$$

Using the orthogonality property of the f_n leads to obtain n^{th} expansion coefficient:

$$h_n\left(x,y,t\right)=h\left(x,y,t\right)\frac{\int\limits_{-h}^{0} f_n dz}{\int\limits_{-h}^{0} f_n^2 dz}=h\left(x,y,t\right)\frac{2\sinh\left(2\beta_n h\right)}{2\beta_n h+\sinh\left(2\beta_n h\right)}. \tag{2.9}$$

Since

$$\phi_{n_{zz}}=\beta_n^2\phi_n, \tag{2.10}$$

As a result, the governing equation and boundary conditions shown in Eq. (2.4) are rewritten in term of ψ_n's and f_n's as:

$$\begin{cases} \frac{1}{c_s^2}\psi_{n_{tt}}f_n-\nabla^2\psi_n f_n-\psi_n f_{n_{zz}}=0 & \\ \psi_{n_{tt}}f_n+g\psi_n f_{n_z}=0 & \text{at}\quad z=0 \\ \psi_n f_{n_z}+\nabla h\cdot\nabla\psi_n f_n+h_{n_t}f_n=0 & \text{at}\quad z=-h\left(x,y,t\right). \end{cases} \tag{2.11}$$

Multiplying the first equation of (2.11) by f_m, integration in depth yields to:

$$\int\limits_{-h}^{0}\left(\frac{1}{c_s^2}\phi_{n_{tt}}f_m-\nabla^2\phi_n\right)f_m dz-\int\limits_{-h}^{0}\beta_n^2\phi_n f_m dz=\int\limits_{-h}^{0}\left(\phi_{n_{zz}}f_m-\phi_n f_{m_{zz}}\right)dz \tag{2.12}$$

Applying second Green's identity to the right hand side (RHS) terms of (2.12) yields:

$$\int\limits_{-h}^{0}\left(\frac{1}{c_s^2}\phi_{n_{tt}}-\nabla^2\phi_n-\beta_n^2\phi_n\right)f_m dz=\left[f_m\phi_{n_z}-\phi_n f_{m_z}\right]_0-\left[f_m\phi_{n_z}-\phi_n f_{m_z}\right]_{-h} \tag{2.13}$$

The values of $f_n(z)$ at boundaries are:

$$\begin{array}{lll} f_n=1, & f_{n_z}=\beta_n\tanh\left(\beta_n h\right) & \text{at}\quad z=0 \\ f_n=1/\cosh\left(\beta_n h\right), & f_{n_z}=0, & \text{at}\quad z=-h \end{array} \tag{2.14}$$

Substituting boundary values at free surface and bottom in first and second RHS term of (2.13) and by virtue of Leibniz's rule the second term

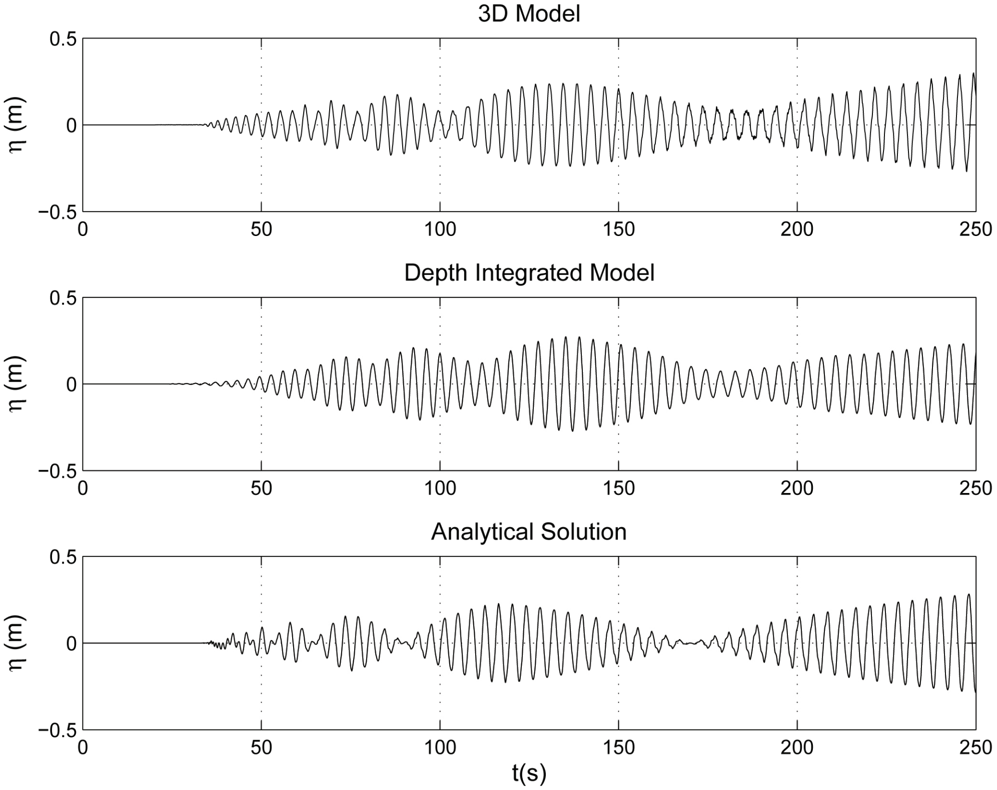

Figure 2.2: Free surface elevation time series at 50 km from the tsunamigenic source as they result from the three models.

of the LHS combines with the third term of the RHS, so that Eq. (2.13) becomes:

$$\begin{gathered}\psi_{n_{tt}}\tfrac{C_n}{c_s^2}-\nabla\left(C_n\nabla\psi_n\right)-\beta_n^2C_n\psi_n+\tfrac{1}{g}\psi_{n_{tt}}+\tfrac{\omega^2}{g}\psi_n-\tfrac{h_{nt}}{\cosh^2(\beta_n h)}=\\ \left[f_n\psi_n\nabla h\cdot\nabla f_n\right]_{-h}+\psi_n\int\limits_{-h}^{0}f_n\nabla^2f_n\,dz,\end{gathered}\tag{2.15}$$

After doing some math and neglecting higher order terms $O\left(|\nabla h|^2,\nabla^2 h\right)$, the final form of the equation describing all the hydro-acoustic and tsunami

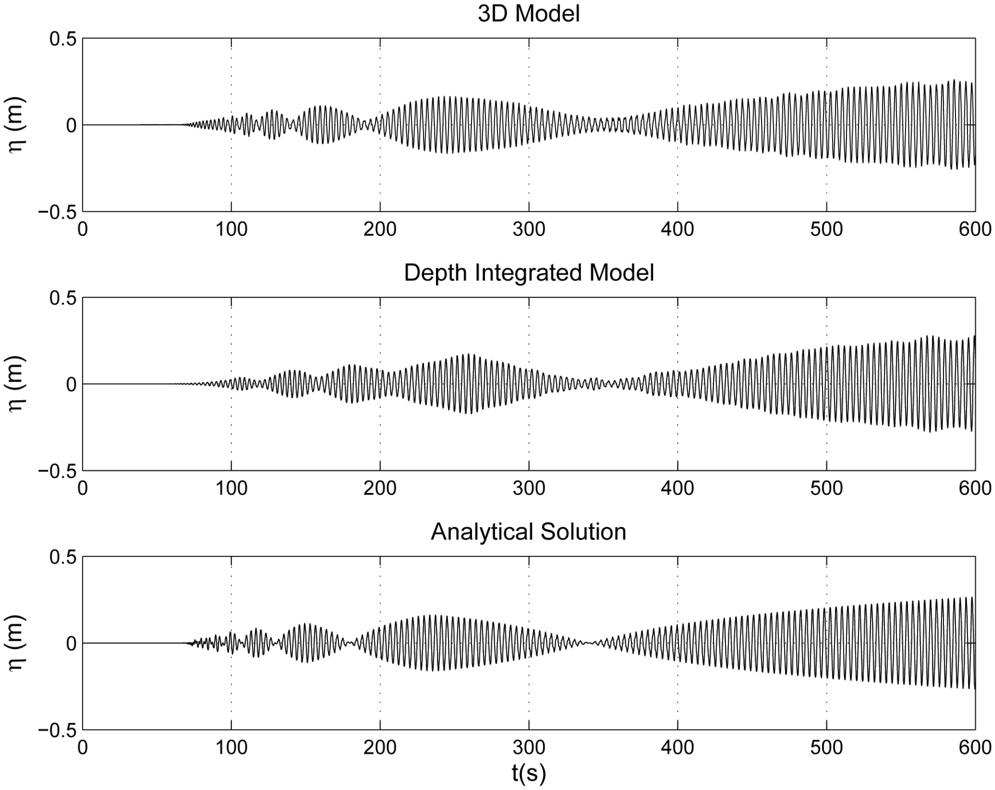

Figure 2.3: Free surface elevation time series at 100 km from the tsunamigenic source as they result from the three models

mechanics in the horizontal x, y plane:

$$\psi_{n_{tt}}\left(\frac{C_n}{c_s^2}+\frac{1}{g}\right)-\nabla\left(C_n\nabla\psi_n\right)+\left(\frac{\omega^2}{g}-\beta_n^2C_n\right)\psi_n=h_tD_n, \tag{2.16}$$

where $C_n(x,y)$ and $D_n(x,y)$ are given by:

$$C_n(x,y)=\frac{2\beta_nh+\sinh\left(2\beta_nh\right)}{4\beta_n\cosh^2\left(\beta_nh\right)}, \tag{2.17}$$

$$D_n(x,y)=\frac{4\tanh\left(\beta_nh\right)}{\left(2\beta_nh+\sinh\left(2\beta_nh\right)\right)}. \tag{2.18}$$

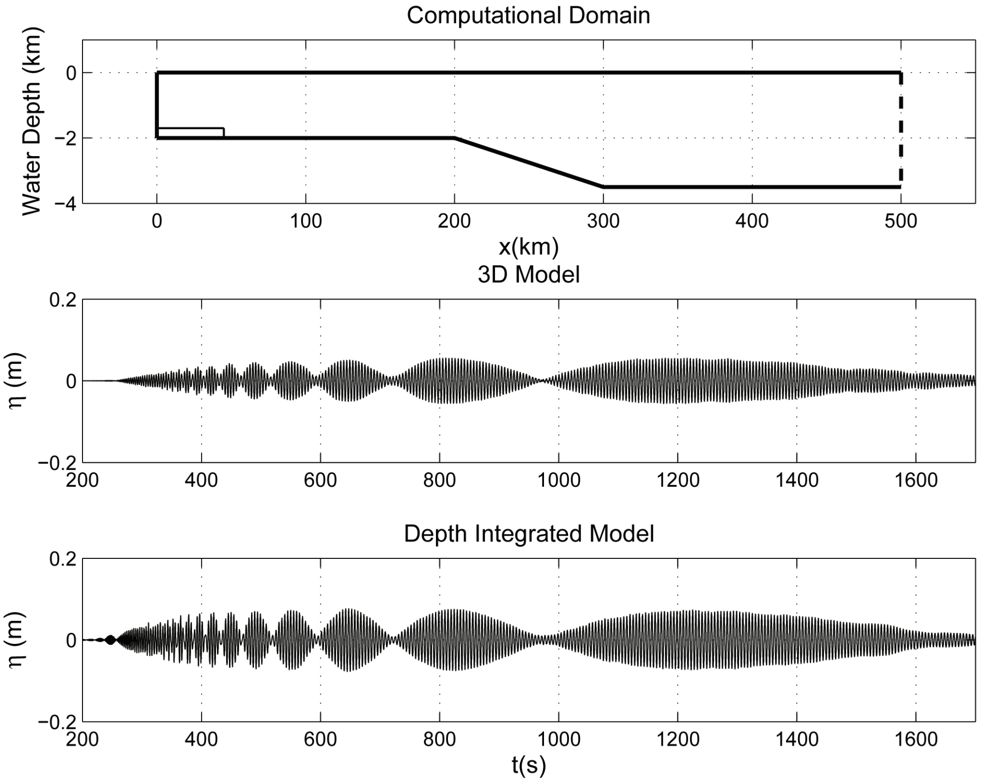

Figure 2.4: Upper panel: computational domain. Lower panels: free surface elevation time series at 400 km from the tsunamigenic source as they result from the two models.

The subscript n indicates that Eq. (2.16) is valid for the generic n^{th} mode, the gravity one and the hydro-acoustic ones. The mathematical problem is solved for a single frequency ω and corresponding forcing spectrum for narrow frequency band. The superimposition of the results of many equations as Eq. (2.16), one for each mode, will lead to complete modeling of the free surface fluid potential generated by a fast sea-bed motion. For incompressible fluid, i.e. in the limit $c_s \to \infty$, the MSEWC reduces to the Mild Slope Equation (MSE) for surface gravity waves (*Berkhoff*, 1974) extended to allow for bottom motion (*Cecioni and Bellotti*, 2010a; *Cecioni and Bellotti*, 2010b).

2.2 Sample computations

Sample computations have been carried out to verify if the model equation (2.16) can be safely applied instead of more computationally expensive three-dimensional ones. Herein we present the results for two different domains, one with a constant water depth and the other with a varying sea bottom. In the constant water depth computation, two models have been used for comparison: a finite element solver of the full three-dimensional mathematical problem (2.4) and the analytical solution of *Stiassnie* (2010). The simplified earthquake effect is modeled as a displacement in the vertical direction of the bottom; water depth is 1500 m. The area's width of the raising bottom is 30 km; the bottom velocity is 1 m/s for a total displacement of 1 m. Frequency bands of width 0.02 Hz have been selected to discretize the forcing spectrum. The numerical solvers are applied on a computational domain 500 km long; given the symmetry of the problem about the middle of the earthquake ($x = 0$), computations are undertaken only for half of the physical domain. An appropriate boundary condition is applied at the open end of the domain, so that the waves leave the domain freely. At x=0, a fully reflective boundary condition is used in order to preserve symmetry. In order to correctly reproduce the wave field, the maximum mesh size is 200 m, for a total of 1250 degrees of freedom (DOF) in the case of the depth-integrated model (2.16), and more than 10000 DOF for the three-dimensional one (2.4). The time step is $t = 0.1$ s and the computational time to reproduce 1000 s of real-time simulation was about 1 hour for (2.16) and about 10 hours for (2.4); a computer equipped with an i7 2:67 GHz CPU and 12GB RAM has been used.

The results are presented in the Figures 2.2-2.3 in terms of free surface elevation η. At x=50 km (Figure 2.2) the two numerical models are in optimal agreement. Both the general structure of the time series and the values of the η are almost identical. The analytical solution by *Stiassnie* (2010) is still very similar to the two numerical results but some differences exist. At x=100 km (Figure 2.3) there is agreement between the three solutions. However, the depth-integrated model shows the modulation not as properly as in the other two sample results. Nevertheless the general structure of the time series is still in very good agreement as well as the values attained by the η.

In the second case of varying sea bottom, the domain's geometry, depicted in the upper plot of Figure 2.4, has a 200 km area with a constant water depth of 2 km, an area of 100 km with a sloping bottom, and another area of 200 km with constant water depth of 3.5 km. The model is compared only with the three-dimensional numerical model, as an analytical solution is not readily found. The earthquake model occurs in the shallower area (2 km water depth), it has a width of 45 km and it moves vertically with bottom velocity equal to 2 m/s for a total displacement of 2 m. The maximum mesh size is again 200 m, for a total of 3000 DOF in the case of the depth-integrated model (2.16), and 30000 DOF for the three-dimensional one (2.4). The time step and the discretization of the spectra are the same of the constant depth case. The computational time to reproduce 3000 s of real-time simulation was about 2 hours for (2.16) and about 24 hours for (2.4), using the same computer of the previous simulation. The results are presented in Figure 2.4 in terms of free surface elevation η, at a distance x=400 km from the moving sea bed area. The two time series are in good agreement, both in terms of amplitude and modulation of the signal.

2.3 Conclusions

The correct detection of hydro-acoustics waves generated by sudden displacement of the ocean bottom could enhance significantly the efficiency and promptness of Tsunamis Early Warning Systems. Hence the necessity of a full modelization of the phenomenon in the Oceans and Seas. We have therefore considered a weakly compressible inviscid fluid in which waves are generated by a moving bottom and then propagate over a mildly sloped sea bed. Via a proper application of the averaging technique, we have derived the hyperbolic Mild Slope Equation for Weakly Compressible fluids, MSEWC. Solution of the equation allows the description of all the mechanics in the x, y plane, overcoming at the same time both analytical and numerical difficulties. Indeed on the one hand, by expanding in series of the vertical eigenfunctions, the MSWEC retains semi-analytical and can be applied to more complex geometries other than the horizontal or piecewise horizontal in the x, z vertical plane as in the seminal work of *Stiassnie* (2010) and *Kadri and Stiassnie* (2012). On the other hand, because computational time savings is so dramatic, i.e. one order of magnitude shorter than fully numerical 3D model, systematic applications supporting a TEWS in the Oceans and Sea of geophysical interest will be viable. Indeed, once a bottom displacement time series and spectrum is given, the computations can be carried out by dividing the spectrum in frequency bands, propagating each harmonic separately and then using superposition. So far the MSWEC has been compared with analytical solutions and three-dimensional numerical model results. Work is in progress to obtain reliable field measurements of hydro-acoustic waves (*Simeone and Viola*, 2011; *Riccobene*, 2012) related to seismic events, to measure the MSWEC performances against more realistic benchmark data sets. Moving to more realistic events, the presented MSEWC is used to simulate hydro-acoustic wave field in real bathymetry:

1- In Chapter 3, MSEWC is used to reconstruct the hydro-acoustic wave propagation generated by two main tsunamigenic destructive historical earthquakes occurred in the Mediterranean Sea: the 365 AD Crete event and the 1693 Sicily event.

2- In chapter 4, MSEWC is used to reconstruct the 2012 Haida Gwaii event.

For both cases The depth-integrated model has been validated through comparison with the solution of the full three-dimensional weakly compressible wave problem in real-bathymetry, along vertical (2D) sections of the sea. The comparison allowed to set up some computational parameters in order to optimize the depth-integrated model.

Chapter 3

Large-scale numerical modeling of hydro-acoustic waves generated by tsunamigenic earthquakes: Mediterranean Historical Events

In this chapter the numerical model presented in Chapter 2 for reproduction of hydro-acoustic waves is applied to analyze the generation and propagation in real bathymetry of these pressure perturbations for two historical catastrophic earthquake scenarios in Mediterranean Sea. The model is based on the solution of a depth-integrated equation and therefore results computationally efficient in reconstructing the hydro-acoustic waves propagation scenarios. Herein, the results and the physical implications of the first large geographical scale application of the numerical model based on the depth-integrated equation of *Sammarco et al.* (2013) are illustrated. The model is applied to simulate the hydro-acoustic wave propagation generated by two main tsunamigenic destructive historical earthquakes occurred in the Mediterranean sea: the 365 west Crete and the 1693 east Sicily events. The depth-integrated model has been validated through comparison with the solution of the full three-dimensional weakly compressible wave problem in real-bathymetry, along vertical sections of the sea. The comparison allowed to set up some computational parameters in order to optimize the depth-integrated model. The simulation of hydro-acoustic waves propagation in real bathymetry enables to investigate the correlation between the hydro-acoustic waves and the generation mechanism, the source location, the bottom topography and the depth of the pressure recording point. Moreover, in the portion of Mediterranean sea considered in the present research, two deep-sea observatories are located off-shore the East Sicilian coast. These observatories, described later in more details, are equipped, among others instruments, with low-frequency and large-bandwidth hydrophones. Therefore the numerically reproduced scenario provide indications on the attended hydro-acoustic signals in the case of submarine earthquake occurrence. The chapter is structured as follows: section 3.1 describes the large scale numerical simulations of the two selected historical tsunamis; in section 3.2 discussions and conclusions are given.

3.1 Mediterranean sea Historical Events

A first large geographical scale application of the numerical model based on Eq. (2.16) is presented in this section. The model is applied to simulate the gravity and hydro-acoustic wave propagation generated by two main destructive historical earthquakes, occurred in the Mediterranean sea: the 365 west Crete event, and the 1693 east Sicily event. Their seismic parameters are reported in Table 3.1. Figure 3.1 shows the bathymetric data, used in the numerical simulation. These are taken from the National Geophysical Data Center (NGDC) data base, ETOPO1. The computational domain is a portion of the Mediterranean Sea. Dashed black lines represent the open sea boundaries, where a condition of waves free exit is imposed. The larger domain 1 is related to 365 west Crete earthquake whereas for 1693 east Sicily event, the numerical domain is restricted to the smaller domain 2. In Fig. 3.1 two points are indicated, namely CTS and CP, which correspond to the position of two submarine observatories, equipped with hydrophones.

3.1.1 Deep Sea Observatories in Mediterranean Sea

The Catania Test Site (CTS) observatory (N 37°30.008’, E 15°23.034’ North site, N 37°32.861’, E 15°23.844’ South site) is located around 25 km offshore the harbor of Catania and at a water depth of 2 km. The Capo Passero (CP) observatory (N 36°17’33.57”, E 15°58’53.02”), is located 100 km offshore the Capo Passero village and at 3400 m below the mean sea level. Both

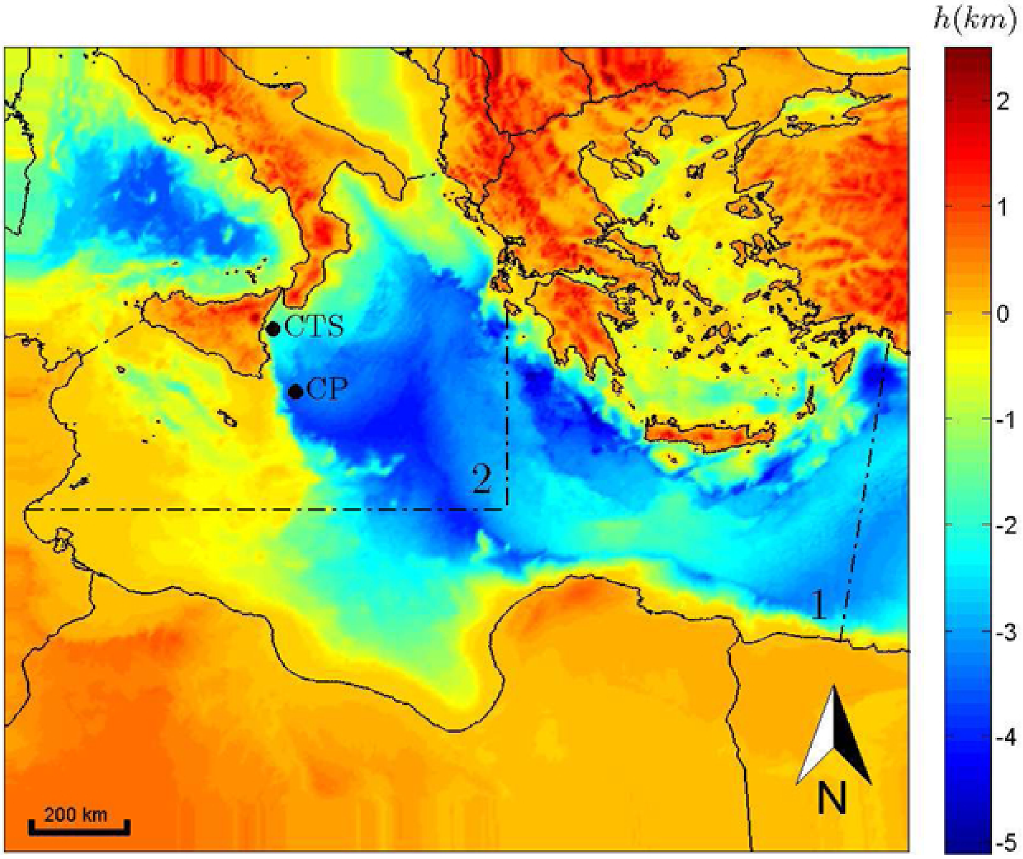

Figure 3.1: Mediterranean Sea bathymetry. Domain 1 and 2 represent the computational domain for scenario 365 west Crete and 1693 east Sicily respectively. Points CTS and CP are deep sea observatory stations at Catania (-2000 m) and Capo Passero (-3400 m)

Table 3.1: Magnitude M_w and seismic moment M_0 for the two scenarios as determined by *Tonini et al.* (2011)

Scenario	M_w	M_0 (Nm)
365 west Crete	8.5	$6.32\ 10^{21}$
1693 east Sicily	7.2	$7.07\ 10^{19}$

observatories are connected to shore through a submarine electro-optical cable. The observatories located in the Catania Test Site are dedicated to multi-disciplinary activities, equipped with low-frequency (0.1 Hz-1 kHz) and large-bandwidth (10 Hz-70 kHz) hydrophones, seismometers, CTDs, magnetometers and current-meters (*Cecioni et al.*, 2015).

The Capo Passero submarine observatory has been designed and constructed by INFN in the framework of the NEMO and KM3neT-Italia (www.km3net.org) projects. Aboard this observatory an antenna of large bandwidth hydrophone (10 Hz-70 kHz) has been installed within the activities of the SMO (Submarine Multidisciplinary Observatory) FIRB research project, funded by the Italian Ministry for University and Scientific Research (MIUR). SMO aims at collecting real-time acoustic data for three main scientific areas: astrophysics, for the neutrino detection, bio-acoustics, for the whale tracking and geophysics for the recording of hydro-acoustic wave generated by submerged earthquakes. The SMO has been installed in March 2013 and since then has been acquiring data in real time. The position of the two observatories has been used to analyze the numerically reproduced hydro-acoustic signals generated by the two historical earthquakes.
The model has been validated through comparison with the solution of the full three-dimensional weakly compressible wave problem in real-bathymetry along a vertical section (2D). The comparison allows to validate and optimize the depth-integrated model. From the simulated hydro-acoustic wave signals it has been possible to identify some general characterization of these pressure waves depending on the generation mechanism, the source location, the bottom topography and the depth of the pressure recording point. Furthermore the numerically reproduced scenarios provide preliminary indications for the implementation of innovative TEWS based on hydro-acoustic wave measurements. Details on each earthquake-tsunami event and their modeling, are given in the following subsections.

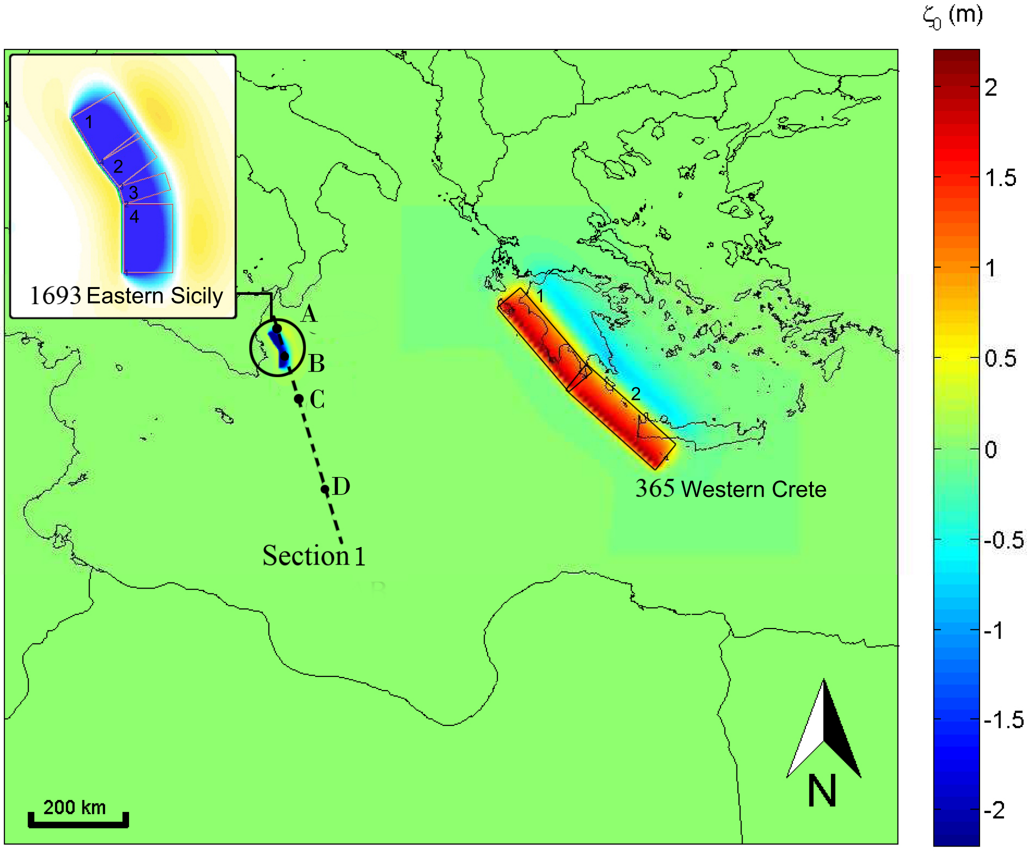
ζ_0 (m)
2
1.5
1
0.5
0
-0.5
-1
-1.5
-2
1
2
3
4
1693 Eastern Sicily
A
B
C
D
Section 1
1
2
365 Western Crete
N
200 km

Figure 3.2: Residual vertical sea bed dislocation, $\zeta_0(m)$, for the 365 west Crete earthquake (right) and 1693 east Sicily earthquake (left) as reconstructed by *Tonini et al.* (2011).

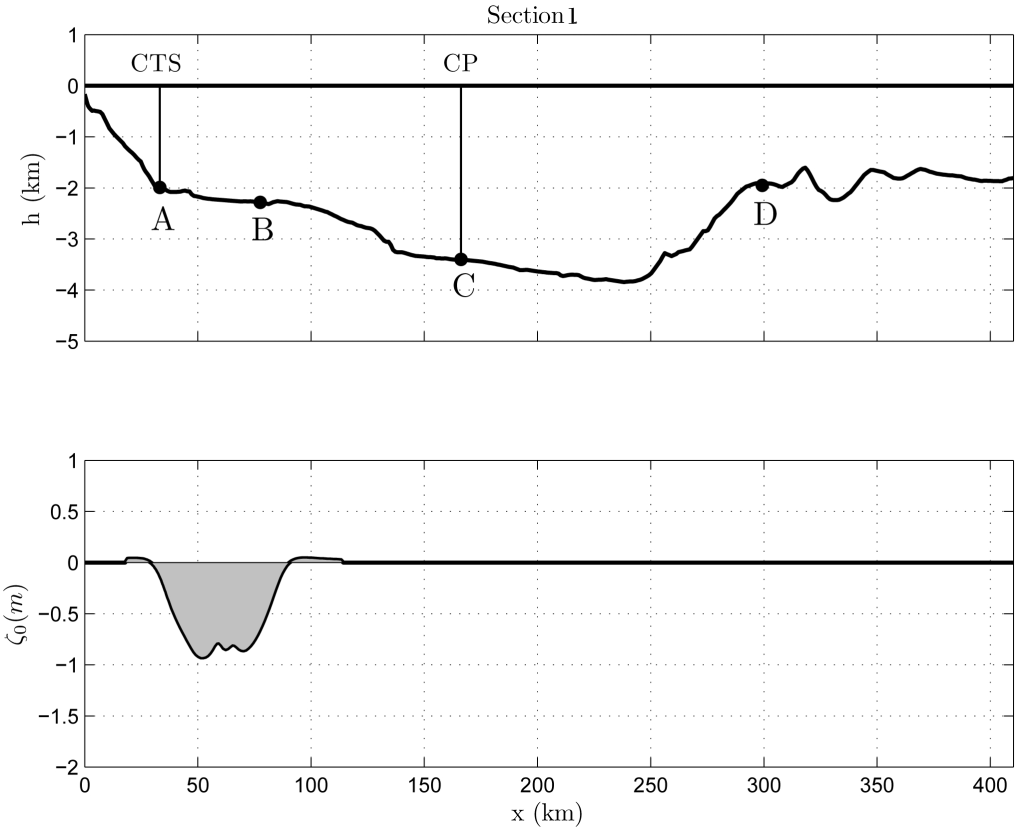

Figure 3.3: Water depth (h) and Residual sea-bed displacement (ζ_0) for the vertical section 1, which crosses the two CP and CTS stations for 1693 Eastern Sicily event. The arbitrary points A, B, C and D are shown in Figure 3.2.

Table 3.2: Seismic parameters of 365 west Crete earthquake, as reconstructed by *Tonini et al.* (2011), for the North segment 1 and South segment 2 shown in Figure 3.2.

Seismic parameters	Segment 1	Segment 2
Length (m)	230	230
Width (m)	90	90
Strike (°)	312	320
Dip (°)	21	21
Rake (°)	90	90
Slip (m)	5	5
Upper edge depth (km)	5	5

Table 3.3: Seismic parameters of the 1693 east Sicily earthquake, as reconstructed by *Tonini et al.* (2011), for the four segments from North to South shown in Figure 3.2.

Seismic parameters	Segment 1	Segment 2	Segment 3	Segment 4
Length (m)	14.7	8.8	5	19.2
Width (m)	16.5	16.5	16.5	16.5
Strike (°)	329	322	343	360
Dip (°)	35	35	35	35
Rake (°)	270	270	270	270
Slip (m)	3	3	3	3
Upper edge depth (km)	0.5	0.5	0.5	0.5

3.1.2 The 365 west Crete scenario

The undersea 365 west Crete earthquake occurred on July, 21^{st} 365 west Crete in the Eastern Mediterranean, with an assumed hypo-center located off western Crete, along a major thrust fault parallel to the western Hellenic trench. Geologists today estimate that the quake intensity was 8.5 on the Richter Scale or higher, causing widespread destruction in central and southern Greece, Libya, Egypt, Cyprus, and Sicily. In Crete nearly all towns were destroyed. This earthquake was followed by a tsunami which devastated the Mediterranean coasts, killing thousands of people and hurling ships 3 km inland.

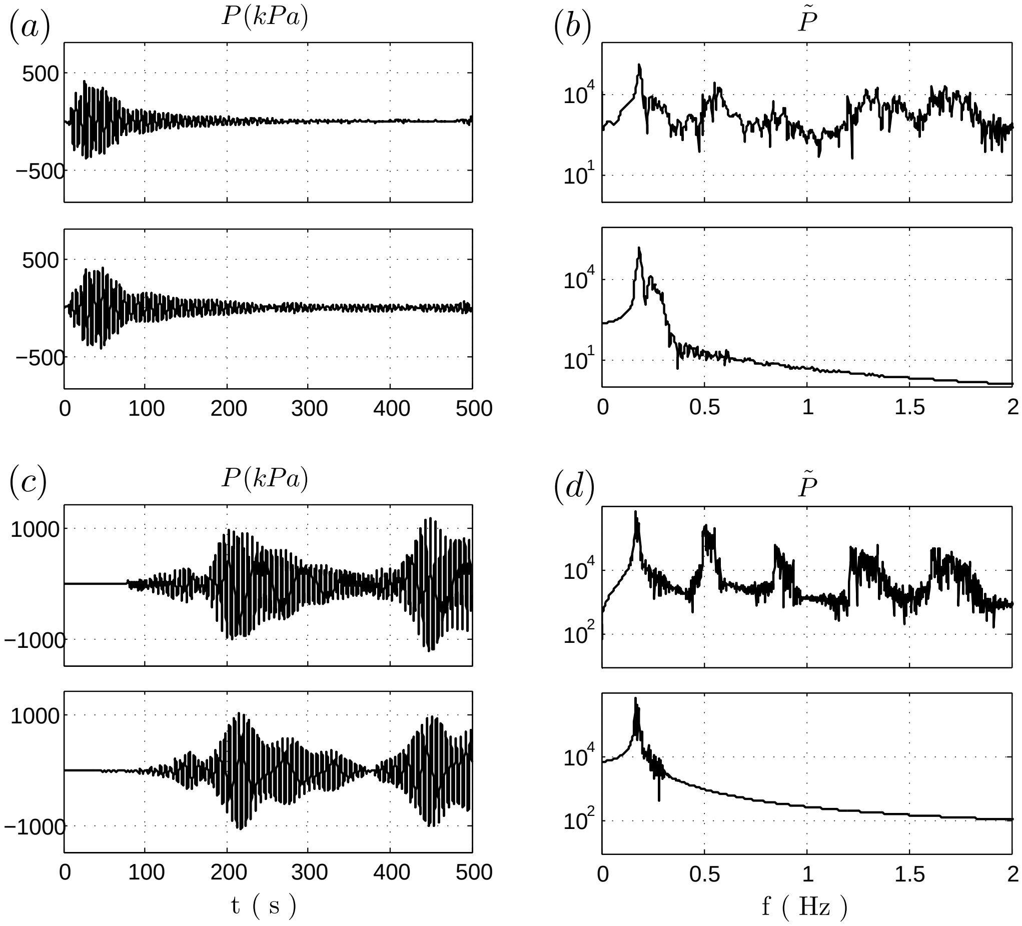

Figure 3.4: Pressure time series (left column) and their frequency spectra (right column) at CTS (a; b) and at CP (c; d). Comparison between the solution of the 3-D reference model (upper plots) and the solution of the depth-integrated equation (lower plots).

This work considers a reconstructed scenario of this earthquake, in order to numerically reproduce the generated hydro-acoustic waves. Following the works of *Shaw et al.* (2008) and *Tonini et al.* (2011), we consider almost the whole rupture of the western Hellenic arc. Making use of the simplified fault model of *Tonini et al.* (2011), the seismic parameters are described in table 3.2. The reconstructed residual sea-bed dislocation, ζ_0 has been calculated by means of the *Okada* (1985) formulas and it is shown in Fig. 3.2. The transient bottom motion is described by:

$$h_t = -\zeta_t = -\frac{\zeta_0}{\tau}\left[H\left(t\right) - H\left(t-\tau\right)\right], \tag{3.1}$$

where H is the Heaviside step function, $\zeta_0\left(x, y\right)$ is the residual displacement, τ is the duration of the sea-bed motion and the sea-bed velocity is assumed constant, as ζ_0/τ.

3.1.3 The 1693 east Sicily scenario

On January 11, 1693 a powerful earthquake occurs offshore the East coast of Sicily, Italy. This earthquake was preceded by a damaging fore-shock on January 9. It had an estimated magnitude of 7.2, one of the most powerful in Italian history, destroying at least 70 towns and cities and causing the death of about 60,000 people. The earthquake was followed by tsunamis that devastated the coastal villages at the Ionian Sea coasts and in the Strait of Messina (*Tinti et al.*, 2004). The strongest effects were concentrated around Augusta, where the initial withdrawal of the water left the harbor dry, followed by a wave of at least 2.4 m height, possibly as much as 8 m, that inundated part of the town. The maximum inundation of about 1.5 km was recorded at Mascali. The identification of the tsunami source is still an open issue; *Tonini et al.* (2011) carried out the Worst-case Credible Tsunami Scenario Analysis on the basis of a possible earthquake and a possible submerged landslide. For the analysis of the hydro-acoustic wave generation, the reconstructed earthquake scenario assumed by *Tonini et al.* (2011) has been chosen. The seismic parameters of Table 3.3 are taken as the wave generation condition. Fig. 3.2 shows the plan distribution of the vertical residual sea-bed motion in the overall numerical domain, which occurs downward, differently from the 365 west Crete scenario.

The depth-integrated model is tested by comparison with the 3D solution along a vertical section of the sea. The position of section 1 crossing points

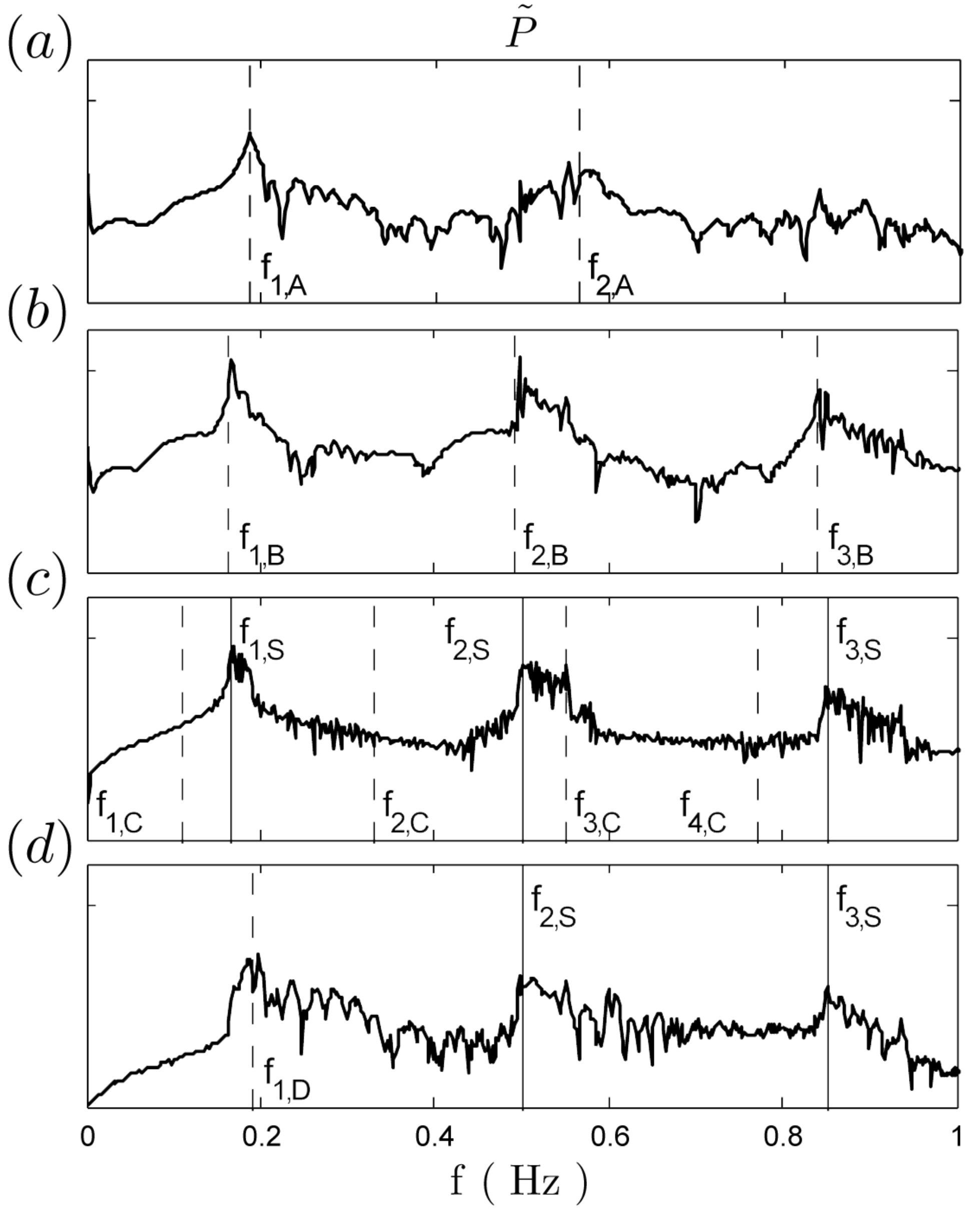

Figure 3.5: Sea bed pressure spectra at point A (h=1990 m), B (h=2283 m), C (h=3401 m) and D (h=1950 m) of Figure 3.3. The dashed lines indicate the natural acoustic frequencies corresponding to observation depth while the solid lines represent the normal acoustic modes for the source depth.

CTS and CP is represented in Fig. 3.2, while Fig. 3.3 shows the water depth and the vertical residual sea-bed dislocation over the section 1. From the comparison between the solution of the complete 3D equation and of the MSEWC, a good agreement is found over all the points of both sections. The results at Catania Test Site and Capo Passero on the section 1 are presented.

Fig.3.4 represents the pressure time series (left column) and the frequency spectra (right column) at Catania Test Site submarine station (upper plots) and at Capo Passero submarine station (lower plots). The depth-integrated results in the time domain almost perfectly reproduce the solution of the 3D mathematical problem. As it can be noted by looking at the spectra, the comparison is in a good agreement for the MSEWC reproduced frequency range (0.15 - 0.3 Hz). In the depth-integrated modeling the reproduction of frequencies out of this range, and relative to the second and higher hydro-acoustic mode, increases the computational time without providing a relevant improvement in the wave simulation.

Since most of the sea-bed motion occurs at a water depth of 2 km, the generated hydro-acoustic waves oscillate at a frequency close to the cut-off value of the first hydro-acoustic mode, i.e. $f_1 = 0.18Hz$ calculated by Eq. (3.2).

$$f_n = \frac{(2n-1)c_s}{4h} \tag{3.2}$$

This signal is however filtered when traveling on shallower waters depth, which allow the propagation only of higher frequency waves (*Abdolali et al.*, 2015a).

Given the complex bathymetry where waves are generated and propagate, the hydro-acoustic wave spectrum presents different frequency bands where energy is localized. In order to investigate the variable depth effect on the spectrum of bottom pressure, four points along section 1 have been selected at different water depths and distances from the epicenter. As can be seen in Figure 3.3, point A is located on the lateral part of shaking fault at a depth of 2000 m while point B is located on the earthquake zone at 2283 m of water depth, point C and D are off epicenter at 3400 and 1950 m water depth respectively. Fig. 3.5 shows the spectra of the numerically reproduced bottom pressure. The source area covers the water depth ranging from 1800 - 2300 m, the minimum frequency for the first mode is 0.16 Hz (for the depth of 2300 m). While the low-frequency wave is traveling to reach the observatory points, the sea-mounts do not let the lower frequencies

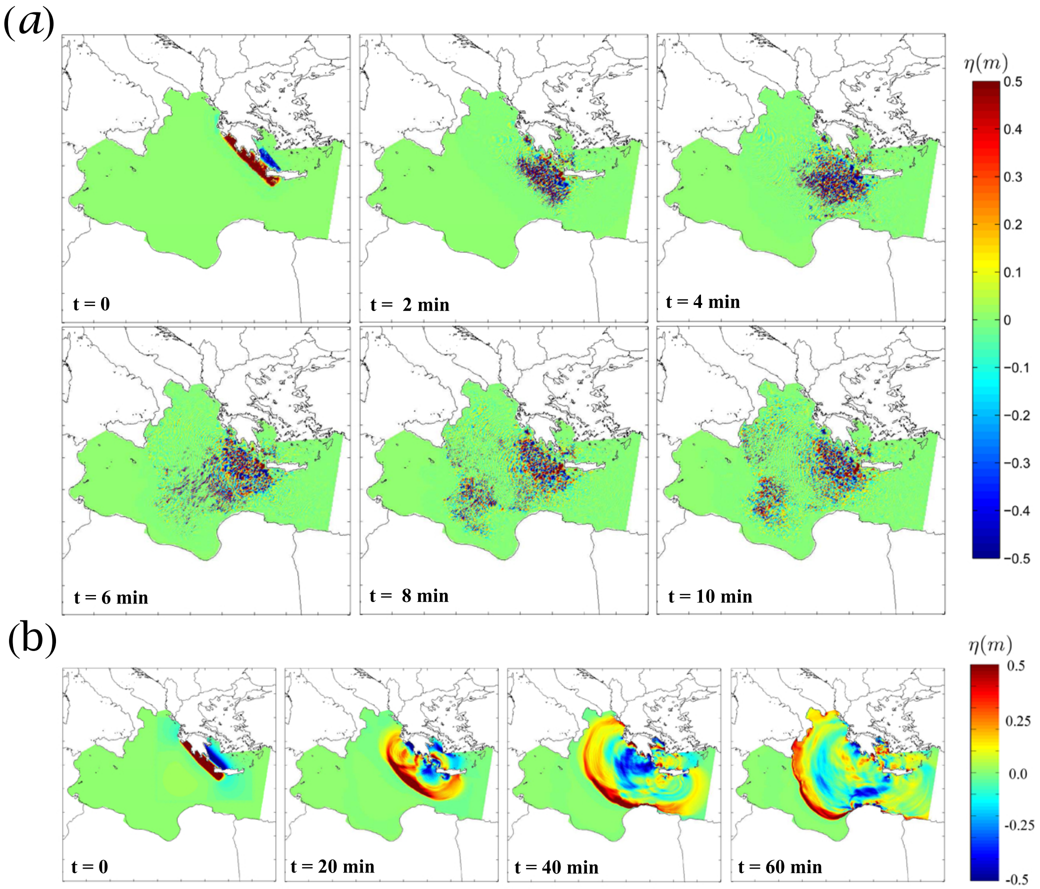
(a)
t = 0
t = 2 min
t = 4 min
t = 6 min
t = 8 min
t = 10 min
$\eta(m)$
0.5
0.4
0.3
0.2
0.1
0
−0.1
−0.2
−0.3
−0.4
−0.5
(b)
t = 0
t = 20 min
t = 40 min
t = 60 min
$\eta(m)$
0.5
0.25
0.0
-0.25
-0.5

Figure 3.6: Snapshots of the free surface (η) hydro-acoustic perturbation (a) and gravity wave (b) given by the 365 west Crete earthquake. t = 0 refers to the time of occurrence of the earthquake

approximated by Eq. (3.2) for $n = 1$ to pass. From the first panel of Fig. 3.5, the observatory is located in shallower depth. As a result, the frequencies larger than first natural mode corresponding to local depth can be observed ($f_{1,A} = 0.19Hz$). In the second panel where the observation point is located on the maximum dislocation at 2283 m of water depth, the spectral peaks are settled on the first three acoustic modes $f_{1,B} = 0.16, f_{2,B} = 0.49$ and $f_{3,B} = 0.83$ (dashed lines). This indicates that at a certain point in the source area, the elastic waves are formed with normal frequencies determined by the local water depth. Spreading from the source zone, the spectrum can be enriched and filtered by higher frequencies representing shallower water normal modes. To reach point C at deeper area passing no sea-mount higher than generation area, whole generated frequencies have been permitted to cross and reach observatory point. The spectrum coincides with first three acoustic modes shown by solid lines corresponding to generation area depth ($f_{1,S} = 0.16$, $f_{2,S} = 0.49$ and $f_{3,S} = 0.83Hz$). On the other hand, the first four acoustic modes corresponding to observatory depth are shown by dashed lines ($f_{1,C} = 0.11$, $f_{2,C} = 0.33$, $f_{3,C} = 0.55$ and $f_{3,C} = 0.77Hz$). The fourth panel emphasizes that the shallower depth of observatory ($h_D = 1950m$ has barricaded propagation of pressure waves with frequencies less than $0.19Hz$ ($f_{1,D}$). The second and third natural mode related to source area can reach the observatory point. Subsequently, the spectrum is peaked at $f_{2,S} = 0.49$ and $f_{3,S} = 0.83Hz$.

In order to correctly reproduce the hydro-acoustic wave field in the numerical domains of Figure 3.1, a maximum element mesh size of 1.2 km has been chosen, for a total number of 2,250,000 and 1,100,000 triangular elements for 365 west Crete and 1993 east Sicily events respectively. The computations have been done for frequency range 0-0.05 Hz for surface gravity wave and 0.05 - 0.5 Hz for hydro-acoustic ones. Solutions were obtained using a high-speed computer equipped with 12 cores i7 3.20 GHz CPU and 64 GB RAM. The MUMPS solver (MUltifrontal Massively Parallel sparse direct Solver) has been used. The results of this large scale simulation are shown in Fig. 3.6 for 365 west Crete and Fig. 3.7 for 1693 east Sicily events in term of free-surface elevation, $\eta(x, y, t)$. At the time $t = 0$ the earthquake occurs, then the hydro-acoustic wave travels at the sound celerity in water, 1500 m/s, while the surface gravity wave front travels with $V_g \approx \sqrt{gh}$ in the Mediterranean sea. Snapshots of the free-surface elevations for gravity waves ($n = 0$ and hydro-acoustic modes ($n \geq 1$) are represented with 10 and 2 minute time interval respectively. For the case of

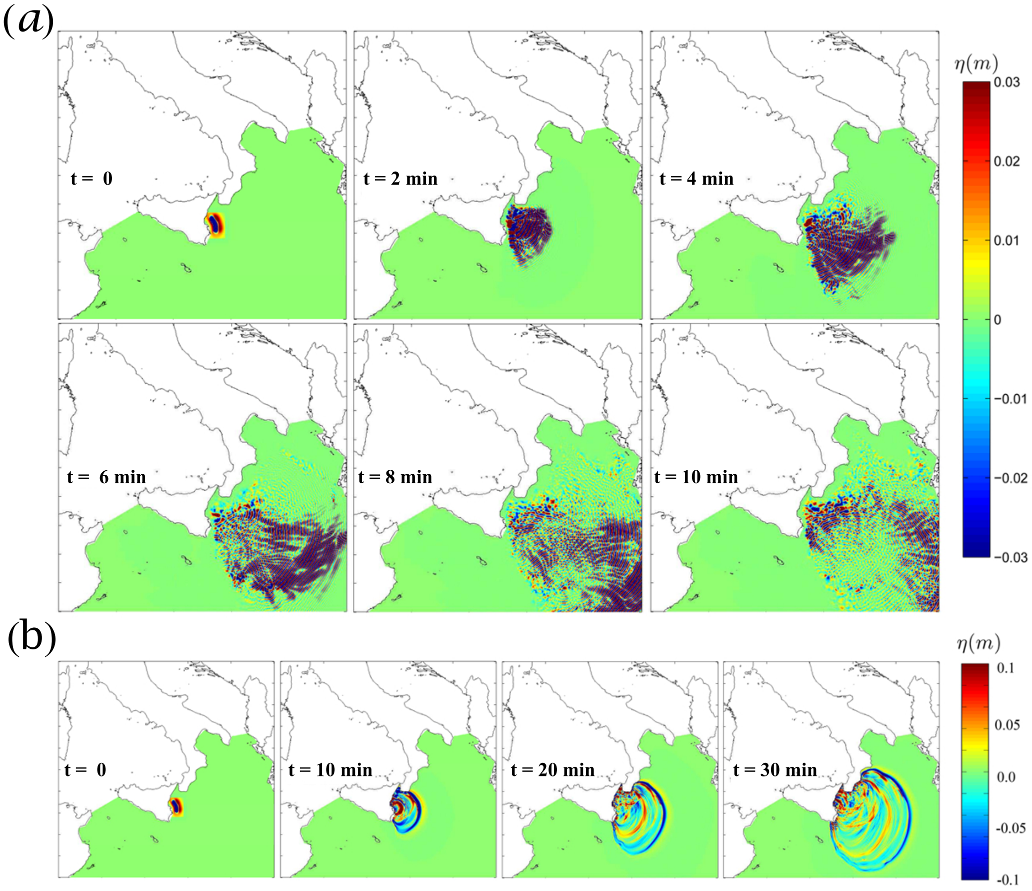
(a)
t = 0
t = 2 min
t = 4 min
t = 6 min
t = 8 min
t = 10 min
η(m)
0.03
0.02
0.01
0
−0.01
−0.02
−0.03
(b)
t = 0
t = 10 min
t = 20 min
t = 30 min
η(m)
0.1
0.05
0.0
-0.05
-0.1

Figure 3.7: Snapshots of the free surface (η) hydro-acoustic perturbation (a) and gravity wave (b) given by the 1693 Catania earthquake. t = 0 refers to the time of occurrence of the earthquake

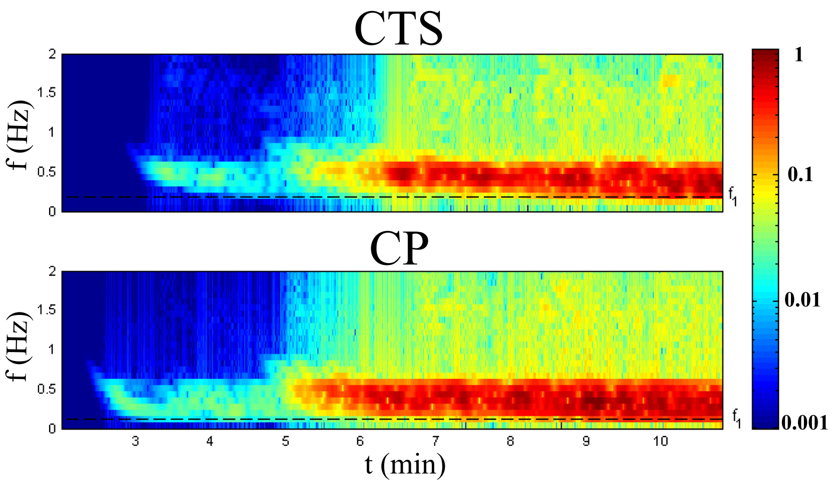

Figure 3.8: The bottom pressure spectrogram at Catania Test Site point (upper panel) and at Capo Passero point (lower panel), resulting from the numerical solution of the depth-integrated Eq. (2.16) over the whole domain. Both plots are normalized divided by the maximum value (Scenario 365 west Crete).

365 west Crete event, a complicated pressure wave perturbation is formed at the free surface and propagates with the sound celerity in water (panel *a*). It covers the entire domain 12 minutes after the event whereas the surface gravity waves reach Italian coasts 1 hr after (panel *b*). The hydro-acoustic wave field shows that these waves tend to propagate towards deeper areas; maximum values of hydro-acoustic wave amplitude are in deeper water close to the generation area. For 1693 east Sicily scenario shown in Fig. 3.7, the reflection backcattering of hydro-acoustic waves occurs and it covers the entire computational domain 8-10 minutes after event (panel *a*) and the gravity waves reaches the Greek coasts almost 40 minutes later (panel *b*).

Spectrograms of bottom pressure are presented in Figures 3.8 for 365 west Crete and 3.9 for 1693 east Sicily scenarios for Catania and Capo passero observatories, as shown in Figure 3.1. Each spectrogram is normalized by dividing the maximum value among two points in order to show the ratio of wave amplitudes at different distances and depths. The local first acoustic modes f_1 are shown by horizontal lines. The arrival time of low-frequency hydro-acoustic signals, traveling with sound celerity in water from the assumed fault is correctly estimated by the model. For the case of 365 west Crete, at both points the hydro-acoustic signal arrives around 5 minutes after the earthquake occurrence, while the long free-surface tsunami waves arrive after about 40 minutes, assuming a constant velocity of $\sqrt{gh}$ in a mean water depth of 2.5 km. Since most of the sea-bed motion occurs at a water depth of 3 km, the generated hydro-acoustic waves oscillate at a frequency close to the cut-off value of the first hydro-acoustic mode, i.e. $f_1 = c_s/4h = 0.12$ Hz. This signal is however filtered when traveling on shallower water depths, which allow the propagation only of higher frequency components (*Kadri and Stiassnie*, 2012). The model results, shown in term of frequency spectra in Fig. 3.8, confirm this water depth filtering effect: the CTS is located at a water depth of 2 km and therefore the cut-off frequency for propagating wave is $f_1 = 0.19$ Hz; the CP site is located at 3.4 km of water depth and records wave oscillation of 0.11 Hz. On the contrary, for the case of 1693 east Sicily event, the observatories are at water depth deeper than generation area and close to shaking fault where there is no sea-mount between them. The CTS point lies above the earthquake, while CP point is about 100 km distant from the epicenter: hence the hydro-acoustic signal arrives after about 1 minute from the earthquake occurrence (Fig. 3.9). Despite the time of arrival and a larger amplitude of the waves at CTS just after the earthquake occurrence, the two pressure signals are very similar. The generated signal has a peak frequency around 0.19 Hz, since the waves are generated at a water depth of 2 km, and at the same frequency are associated propagating modes at the deeper 3 km water depth (CP).

3.2 Conclusions

During history, the Mediterranean sea has experienced catastrophic submarine earthquakes and is potentially hosting active faults. Tsunamis triggered by seismic activities can therefore be destructive. Implementation of a fast Tsunami Early Warning System is mandatory and for the new generations of TEWS, precursor component of tsunami waves like hydro-acoustic waves should be taken into account. The importance of immediate and accurate alarm is magnified since the coastal areas are densely populated and the travel time of tsunamis are very short due to closeness of source and destination, i.e. the travel time of tsunami wave towards the coast is in the order of few minutes up to one hour. The proposed depth-

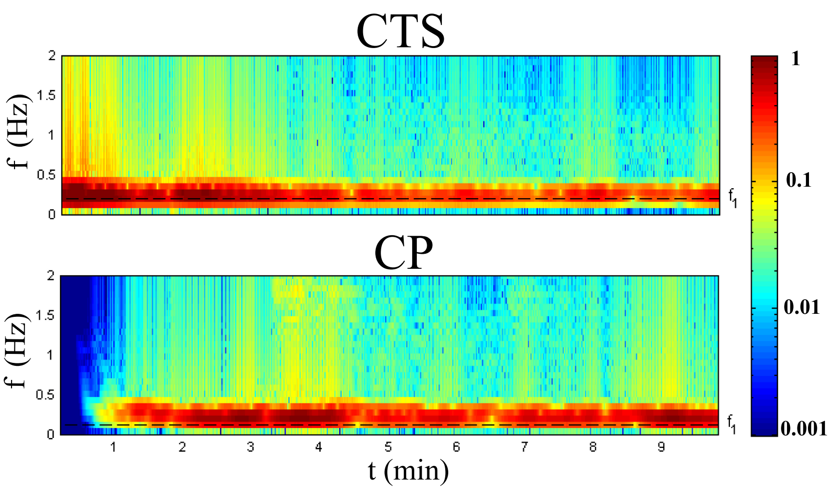

Figure 3.9: The bottom pressure spectrogram at Catania Test Site point (upper panel) and at Capo Passero point (lower panel), resulting from the numerical solution of the depth-integrated Eq. (2.16) over the whole domain. Both plots are normalized divided by the maximum value (Scenario 1693 east Sicily).

integrated model reproduces the mechanism of generation and propagation of surface gravity and hydro-acoustic waves independently due to their different frequency ranges. Solution of the Mild-Slope Equation in Weakly Compressible fluid (*Sammarco et al.*; 2013) is computationally efficient and accurate in comparison with the solution of fully three dimensional models. Simulation of low frequency hydro-acoustic waves in weakly compressible fluid, at real-scale domains is extremely important and leads to better understanding of the relevant phenomena. The depth-integrated equation has been already validated in chapter 2; however in this chapter a first application and validation in real bathymetry has been developed. The full modeling of the hydro-acoustic waves field generated by two historical tsunamigenic earthquake scenarios in the Mediterranean Sea, has been carried out. The numerical model results highlight that the sea-bed motion energy is transferred to hydro-acoustic waves mainly concentrated at the natural acoustic modes. Close to the generation area the frequency spectra clearly show energy peaks for each acoustic mode; spreading off the generation area, the sea-mounts and barriers shallower than the source depth filter out frequencies larger than the cut-off values. The simulation of the 1693 east Sicily earthquake scenario shows that 100 km far from the epicenter, at Capo Passero observation site, the hydro-acoustic waves recorded still allow to identify the energy associated to each acoustic mode since there is no barrier between source and observatory. The numerical simulation confirms that the first mode is the one which carries most of the energy. The hydro-acoustic modes propagate undisturbed in water layer equal or deeper than the one where they have been generated. As the waves propagate in shallower water depth, characterized by higher cut-off frequencies, the components with frequencies lower than the cut-off become evanescent: i.e. when hydro-acoustic waves propagate towards shallower sea depth, the water layer acts as a frequency filter.

To implement innovative TEWS based on measurement and analysis of hydro-acoustic signals, the complete modeling of hydro-acoustic waves in real bathymetry has proven to be extremely useful. The numerical simulations show that the hydrophones must be placed in waters deep enough to record larger frequency range and, if possible, not shielded by sea-mounts. However these instruments should be connected to the shore by submarine cables to guarantee fast data transmission, therefore their location can not be too far from the coastline: hence the model can help choosing the right positioning of the hydrophones system. For the portion of the Mediterranean sea here analyzed, the numerical simulation results suggest that offshore the Sicilian East coast, where the instruments have been placed, and offshore Greek West coast, the waters are deep enough to record and identify the hydro-acoustic waves generated by seismic activities in both the Hellenic arc and the Ionian Sea (South Italy).

Chapter 4

Hydro-acoustic and tsunami waves generated by the 2012 Haida Gwaii earthquake: modeling and in-situ measurements

In this chapter, we reconstruct the hydro-acoustic wave field generated by the 2012 Haida Gwaii tsunamigenic earthquake using the 2D horizontal numerical model, presented in chapter 2, based on the integration over the depth of the compressible fluid wave equation and considering a mild sloped rigid sea-bed. Spectral analysis of the wave field obtained at different water depths and distances from the source revealed the frequency range of low-frequency elastic oscillations of sea water. The resulting 2D numerical model gave us the opportunity to study the hydro-acoustic wave propagation in a large-scale domain with available computers and to support the idea of deep-sea observatory and data interpretation. The model provides satisfactory results, compared with in situ measurements, in the reproduction of the long-gravitational waves.

Recently, the 28 October, 2012 a $M_w = 7.8$ earthquake occurred off the West coast of Haida Gwaii archipelago, Canada. *Cassidy et al.* (2014) defined the event as the first major thrust recorded along the predominantly strike-slip fault plane, which generated a tsunami with a significant run up of over 7 m in several inlets on the archipelago. No significant damage resulted, as the region adjacent to the fault rupture is an uninhabited National Park, and the tsunami was limited to the west coast of the islands where there are no settlements or significant coastal structures. The seismic parameters of this earthquake have been analyzed by *Lay et al.* (2013); moreover, they solved the nonlinear shallow water equations with a vertical velocity term to account for weakly-dispersive waves by means of the finite difference model NEOWAVE (*Yamazaki et al.*, 2009), and successfully compared the results with the tsunami observations.

This chapter presents numerical modeling of tsunami and hydro-acoustic waves generated by the 2012 Haida Gwaii earthquake. The earthquake is modeled starting from the USGS data and by using the *Okada* (1985) formula to reconstruct the residual sea-bed displacement. The wave field is modeled solving depth-integrated mild-slope equation developed in Chapter 2 by means of the Finite Element Method. Model results are compared with field data recorded, during the 2012 Haida Gwaii event, by the Deep-ocean Assessment and Reporting of Tsunamis (DART) network (http://nctr.pmel.noaa.gov/queencharlotte20121027/) and by the Ocean Network Canada (http://www.oceannetworks.ca) at NEPTUNE observatories. Differences between numerical results and field data are probably due to lack of exact knowledge of sea bottom motion and to the rigid sea-bed approximation, indicating the need for further study of poro-elastic bottom effects. Model comparison with observatories motivated us to consider underlying sedimentary layer in model equations. In next chapter, a new depth integrated equation for two layered system is presented revealing a significant improvement in results. The chapter is structured as follows: Section 4.1 describes the 2012 Haida Gwaii earthquake and consequent waves and provides information on the instruments that recorded the event, whose data are then interpreted and used to compare the results of the numerical model. Section 4.2 describes the model to simulate the tsunami event in compressible fluid. In Section 4.3 discussions and conclusions are given.

4.1 2012 Haida Gwaii earthquake: analysis of in situ observations

On 28 October 2012, 03:04 UTC, a powerful $M_w = 7.8$ earthquake struck central Moresby Island in the Haida Gwaii archipelago, Canada (Figure 4.1).

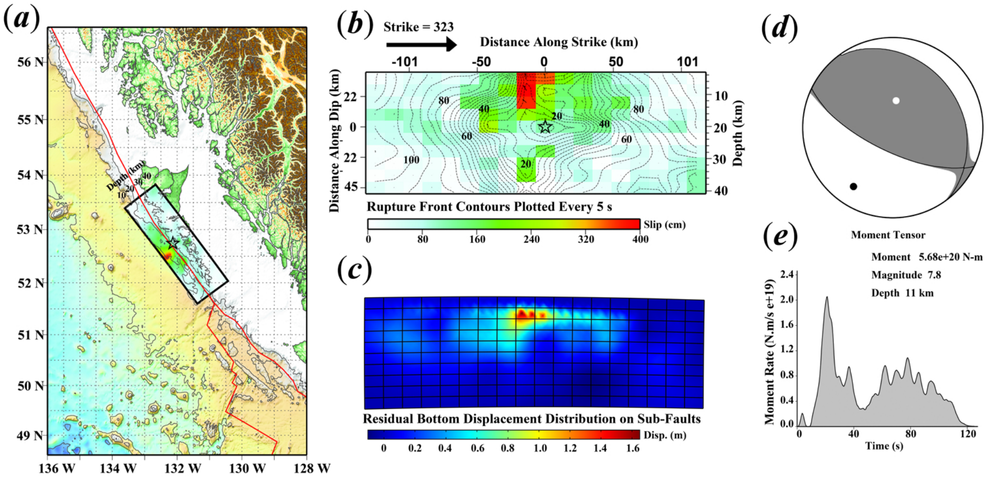

Figure 4.1: a) Surface projection of the slip distribution. The red lines indicate major plate boundaries. Black star is the epicenter location. b) Cross-section of slip distribution. The strike direction of the fault plane is indicated by the black arrow. The slip amplitude are showed in color. Contours show the rupture initiation time in seconds. c) Residual vertical bottom displacement distributed on 180 subfaults. d) Visual representation of the focal mechanism derived from the estimated moment tensor. e) Moment Rate Function, describing the rate of moment release with time after earthquake origin. The plots are taken from National Earthquake Information Center (NEIC) of United States Geological Survey (USGS).

The earthquake hypocenter was located (52.788 °N, 132.101 °W) at a depth of 14 km. This was the largest earthquake to hit Canada since 1949, when a 8.1 magnitude quake hit west of the Haida Gwaii Islands (epicenter at 53.62 °N, 133.27 °W). The 2012 earthquake occurred as an oblique-thrust faulting on the boundary between the Pacific and North America plates. The Pacific plate actually moves approximately north-northwest with respect to the North America plate at a rate of about 50 mm/yr. The National Earthquake Information Center (NEIC) reports a strike of 323° and dip of 25° for this earthquake event.

Figure 4.1 shows the main seismic parameters of the event. Panel *a* presents the surface projection of the slip distribution as determined by *Lay et al.* (2013). The slip distribution on the fault plane is shown in panel *b*.

Contours show the rupture initiation time in seconds with average rupture speed of $V_r = 2.3$ km/s (the rupture time ranges between 0.8 and 74.4 s). Panel *c* shows the residual vertical bottom displacement, calculated by the Okada formula (*Okada*, 1985). The bottom displacement took place in time intervals ranging from 2.4 s to 10 s. The rupture surface is approximately 130 km along the strike direction and 40 km along the dip, and has been divided in 180 subfault elements whose dimensions are 14 km and 10 km in the strike and dip directions respectively. In panel *d*, the moment tensor for nodal planes is shown. Shaded areas show quadrants of the focal sphere in which the P-wave first-motions are away from the source, and unshaded areas show quadrants in which the P-wave first-motions are toward the source. The dots represent the axis of maximum compressional strain (in black, called the "P-axis") and the axis of maximum extensional strain (in white, namely the "T-axis") resulting from the earthquake. Panel *e* describes the moment release rate in time after earthquake origin. All the mentioned seismic data are provided by the Advanced National Seismic System (ANSS) Comprehensive Catalog of the U.S.Geological Survey (USGS), available at web site reported in caption of Figure 4.1.

Free-surface and bottom pressure data have been collected during this earthquake by the DART network and by Ocean Network Canada. Both networks have instruments located approximately 600 km south the earthquake epicenter. Location of observatories which recorded the waves generated by the 2012 earthquake are shown in Figure 4.2, together with bathymetric information and the open-sea boundary of the numerical domain (dashed line) described below. The DART network has been deployed by the National Oceanic and Atmospheric Administration (NOAA), to support real-time forecasting of tsunami events. The closest DART instruments that recorded the 2012 earthquake event are: DART46419 (48°45'59" N 129°37'57" W) at 2775 m water depth and 480 km south of the epicenter, and DART46404 (45°51'18" N 128°46'30" W) at 2793 m water depth, 810 km south of the epicenter. Hereinafter the name of these two stations will be shortened respectively as D_{19} and D_{04}. Tsunami warning was issued after recording strong signatures, which began at 3:04 UTC, for a large stretch of the North and Central coast of the Haida Gwaii region and eastward to Hawaii. Later the tsunami alarm was limited, canceled or downgraded. Ocean Network Canada operates cabled observatories from 100 to 2600 m seaward of southwest coast of Vancouver Island in the northeast Pacific. In this chapter we consider data recorded by

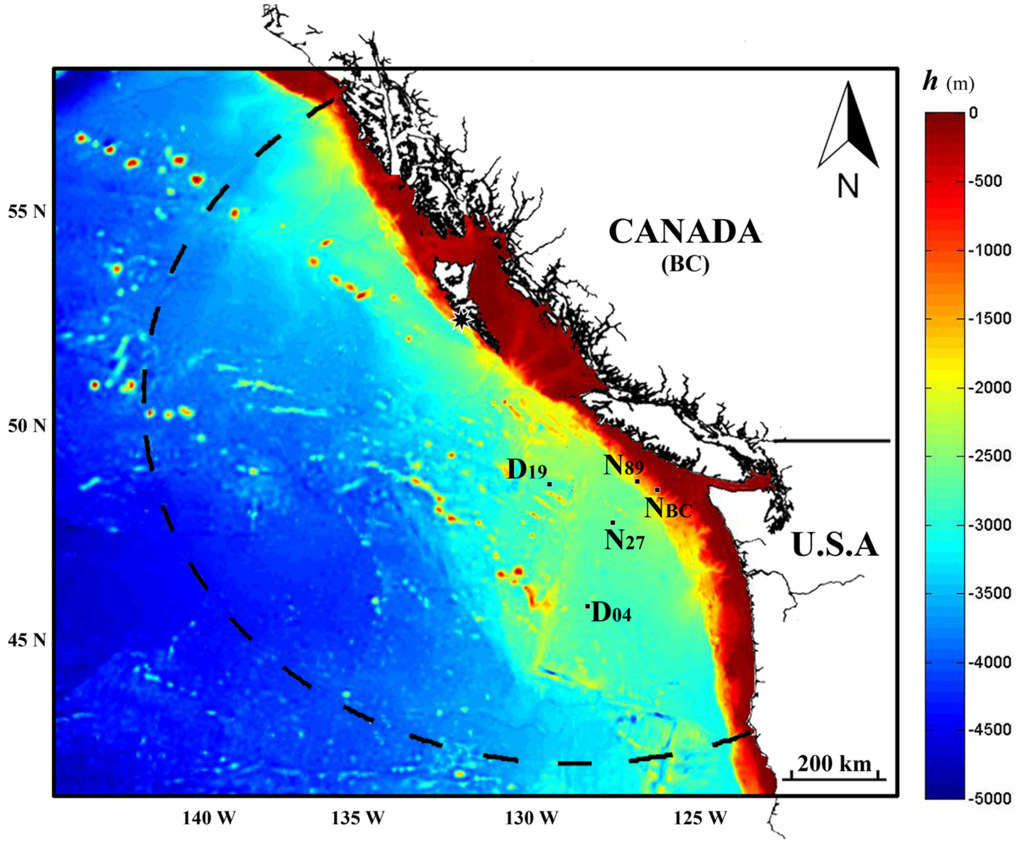
h (m)
0
-500
-1000
-1500
-2000
-2500
-3000
-3500
-4000
-4500
-5000
N
CANADA
(BC)
U.S.A
D19
N89
NBC
N27
D04
200 km
55 N
50 N
45 N
140 W
135 W
130 W
125 W

Figure 4.2: Bathymetry data of the west Canadian and USA coast (ETOPO1 data). The epicenter position is marked with a black star. The black dashed line delimits, together with the coastline, the domain of the numerical computations.

three submarine observatories: CORK ODP1027 located 640 km south of epicenter at Cascadia Basin (47°45.7560' N 127°45.5527'W) in 2660 m water depth (hereinafter N_{27}); Bullseye BPR 889, 590 km south of epicenter, at Clayoquot Slope (48°40.2501'N 126°50.8779W) in 1258 m water depth (N_{89}); Barkley Canyon (Upper Slope) 640 km far from epicenter close to the coast (48°25.6379'N 126°10.4851'W), in 392 m water depth (N_{BC}). These observatories are equipped with many instruments, including bottom pressure records and seismometers. In the hydro-acoustic wave frequency band, as introduced later, the bottom pressure component P_u generated by local ground motion can be obtained from the vertical component (Up-Down) of bottom velocity (u_{UD}), according to Joukowsi Formula (*Landau and Lifshitz*, 1987).

$$P_u = u_{UD} \rho c_s \tag{4.1}$$

where ρ and c_s are respectively the water density and the sound celerity in water, here assumed to be constant with values $\rho = 1030\ kg/m^3$ and $c_s = 1480\ m/s$. Note that the horizontal components of the sea bottom velocity (u_{EW} and u_{NS}) have a minor influence on the wave form and subsequently are excluded from further analysis. Pressure signals recorded by the bottom pressure records of the Ocean Network Canada P_b, are shown in Figure 4.3 as black lines. Panels a, b and c refer to the data at N_{BC}, N_{89} and N_{27} respectively. We have added in all the plots the pressure data P_u (blue lines), calculated using equation (4.1) from the on site seismometer data. On the right side panels, the corresponding spectra are plotted. In order to interpret the spectra, let us define characteristic frequencies for gravitational and hydro-acoustic waves. The characteristic gravitational wave frequency is $f_g = \sqrt{g/h}$, where h is the water depth and $g = 9.81 m/s^2$ is the gravitational acceleration. Additional resonators in compressible water column are characterized by a set of natural frequencies:

$$f^{(n)} = \frac{(2n-1)c_s}{4h} \tag{4.2}$$

where $n = 1, 2, ...$ is the index of the hydro-acoustic mode. The f_g is always smaller than the minimal natural frequency $f^{(1)}$. Therefore, three frequency bands are determined: "Gravitational waves" ($f < f_g$), "Forced oscillations" ($f_g < f < f^{(1)}$) and "Hydro-acoustic waves" ($f > f^{(1)}$). Bottom oscillations within "Gravitational waves" and "Forced oscillations" bands generate gravitational waves. "Forced oscillations" and "Hydro-acoustic waves" bands are responsible for generation of hydro-acoustic waves (*Matsumoto et al.*, 2012). The characteristic frequencies for each location are indicated by dashed vertical red lines in Figure 4.3. At N_{BC} shallow water node (392 m deep) the spectra of P_b and P_u show a good agreement within "Forced oscillations" range, although the $1Hz$ bottom pressure gauge cannot capture the first $0.96Hz$ hydro-acoustic mode. For N_{89} station ($f^{(1)}$=0.31 Hz), the P_b and P_u spectra are almost coincident for "Forced oscillations" ($f_g < f < f^{(1)}$) and "Hydro-acoustic waves" ($f > f^{(1)}$). For "Gravitational waves" band, the P_b and P_u spectra turn out to be different. It can be seen from Figure 4.3 that for the case of both N_{BC} and N_{89} stations, the time series plotted in panels a and b are generated locally within "Forced oscillations" and "Hydro-acoustic waves" bands (panels d and e). In other words, the pressure records are not contaminated by remote sources. The reason behind this fact is the "depth effect" introduced later in Section 4.2.1. These stations indeed are located very close to the fault boundary, and therefore ground shaking would be expected in that area. On the other hand, at N_{27} observatory (panel c), the bottom pressure perturbation is mainly generated in the remote areas including proposed sub-fault for 2012 Haida Gwaii earthquake shown in Figure 4.1. Moreover, station N_{27} is located in deeper water (2660 m), where the hydro-acoustic waves propagate without depth frequency filtering effects (*Cecioni et al.*, 2015). The tiny bottom motion at N_{27} position in contrast to N_{BC} and N_{89} stations proves that bottom pressure records at N_{27} are not generated locally. We note that the first signature of hydro-acoustic waves arrives sooner than the hydro-acoustic travel time from the epicenter, possibly indicating the contribution of faster propagating seismic waves within the solid Earth (*Maeda and Furumura*,2013; *Maeda et al.*,2013; *Kozdon and Dunham*,2014).

4.2 Numerical simulations

The Mild Slope Equation for Weakly Compressible fluid (MSEWC) presented in chapter 2 has been used to reconstruct Haida Gwaii event. The model equation 2.16 is solved for the first mode (n = 0), where β_0 is real. The zero mode is associated with the gravity surface wave, i.e. the tsunami; and for the other modes ($n \geq 1$), namely the hydro-acoustic modes, where β_n is purely imaginary and they are responsible for acoustic oscillations of the

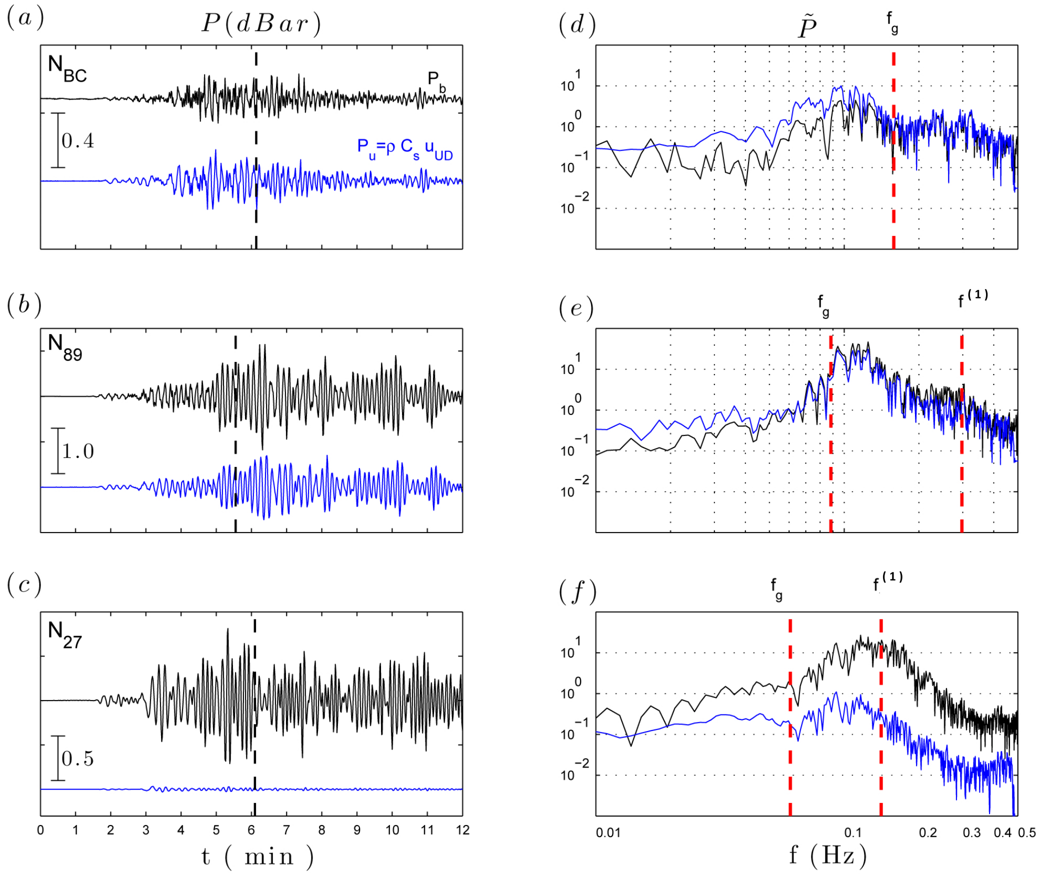

Figure 4.3: Bottom pressure records (black lines) measured at the three stations of Ocean Network Canada (N_{BC}, N_{89} and N_{27} from top (a), to bottom (c)) and the corresponding spectrum from (d) to (f), the pressure perturbation (blue lines) obtained by the vertical component of the sea-bed velocity during earthquake (equation 4.1). The black vertical dashed lines represent the computed arrival time at each stations from the earthquake epicenter of the hydro-acoustic signal traveling at c_s velocity. The red vertical dashed lines represent the characteristic gravitational wave frequency f_g and first hydro-acoustic mode $f^{(1)}$

water body. Superposition of the solutions, ψ_n, of equation (2.16) for each mode leads to complete modeling of the fluid potential generated by a fast sea-bed motion.

In the time domain, the MSEWC reproduces the fluid potential characteristic of a narrow frequency band wave spectrum, centered around the value of a carrier frequency ω, which determines the variables β_n (2.6), C_n (2.17) and D_n (2.18). A simulation of a broad spectrum thus requires that the problem be divided into a set of narrow frequency bands, and then equation (2.16) is solved for each band and the results are superimposed. Hereinafter in the following two subsections are discussed the solutions of equation (2.16) to reproduce the gravity wave ($n = 0$) and the hydro-acoustic wave ($n \geq 1$). In both cases a set of many equation as (2.16), one for each specific frequency, are solved. The results are presented separately because tsunami and hydro-acoustic wave energy occurs at different and not coincident frequency bands. The 2012 earthquake event at Haida Gwaii archipelago, Canada, has been reproduced numerically solving the MSEWC, equation (2.16). The model domain is reported in Figure 4.2; it covers an area of about $1.55 \cdot 10^6 km^2$ of the Pacific Ocean, bounded by the Canadian and USA coasts and by the dashed black line in the open ocean. Figure 4.2 shows the bathymetric data used in the numerical simulations, taken from the National Geophysical Data Center (NGDC) database ETOPO1 (*http : //www.ngdc.noaa.gov/mgg/global/global.html*). The sea-bed motion, reconstructed using Okada formula, is mainly an uplift movement, with a maximum value of $\zeta_0 = 1.6$ m. Unlike the traditional incompressible tsunami models, which often use the residual vertical displacement of the bottom as the initial free surface displacement, in this depth-integrated wave model, the transient time-spatial sea bottom motion is considered for both tsunami and hydro-acoustic modes. The vertical bottom velocity is assumed to be (*Nosov and Kolesov*, 2007):

$$\zeta_t = \frac{\zeta_0}{2}\left[1 - cos\left(\frac{2\pi(t-t_0)}{\tau}\right)\right]\left[H\left(t-t_0\right) - H\left(t-t_0-\tau\right)\right], \tag{4.3}$$

where $H(t)$ is the Heaviside step function and τ is the duration of the bottom displacement. Spreading of the rupture front, starting from epicenter to the far edge of earthquake zone, has been reproduced with a velocity of $V_r = 2.3\ km/s$. In the model the duration of the sea-bed displacement is assumed everywhere constant equal to $\tau = 6.28\ s$. t_0 is the initial time of sea-bed

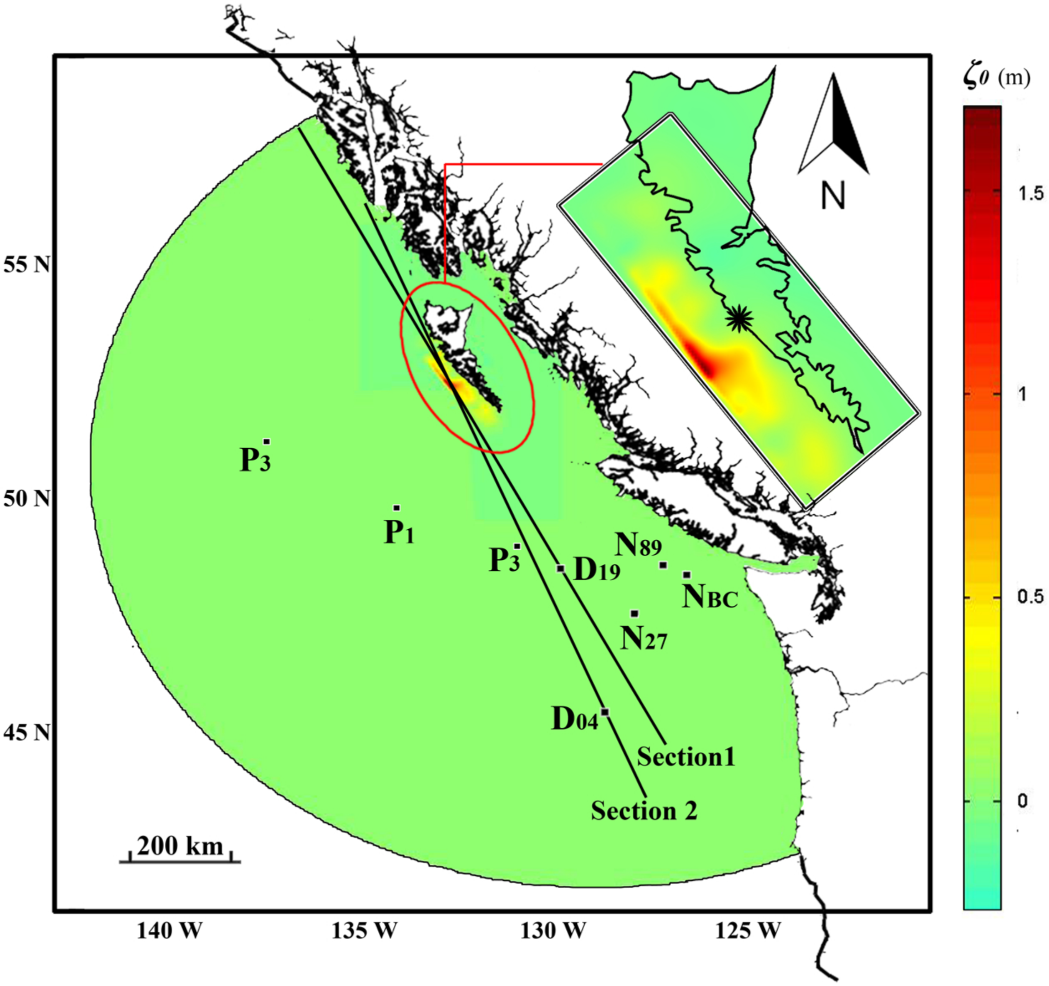
ζ0 (m)
1.5
1
0.5
0
N
55 N
50 N
45 N
140 W
135 W
130 W
125 W
P3
P1
P3
D19
N89
NBC
N27
D04
Section1
Section 2
200 km

Figure 4.4: Vertical residual sea-bed displacement on the numerical domain. The points N_{27}, N_{89} and N_{BC} represent the Ocean Network Canada observatories location, the points D_{19} and D_{04} represent the DART Buoys locations and the points P_1, P_2 and P_3 represent the selected points in front of activated fault in deep sea.

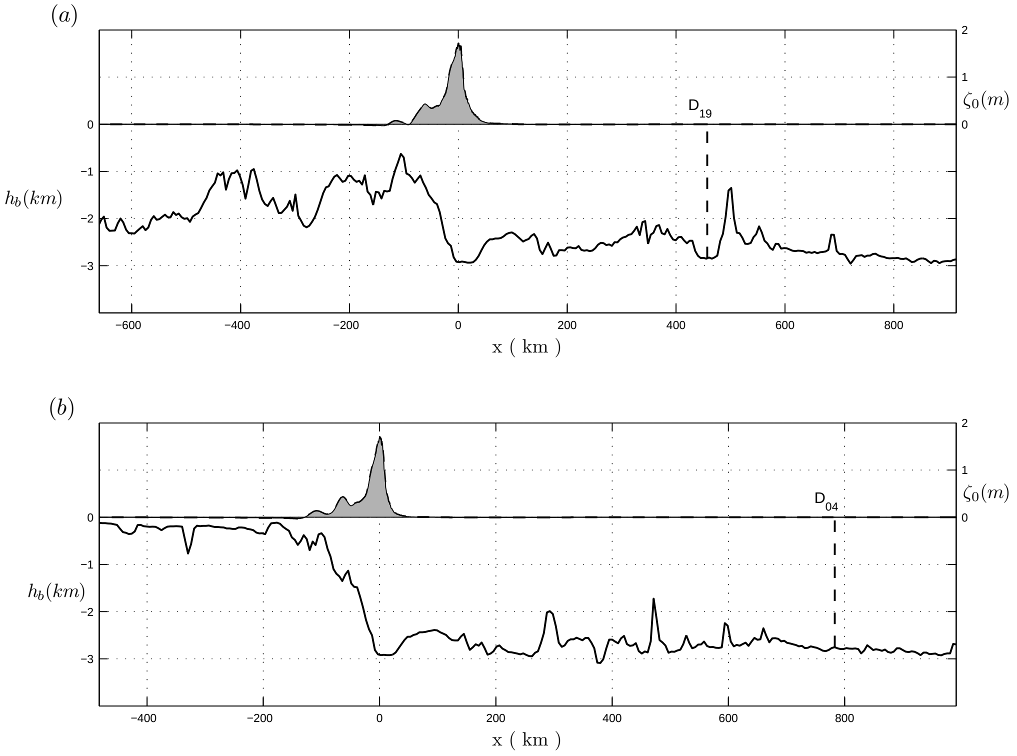

Figure 4.5: Residual sea-bed displacement (ζ_0) and water depth (h_b) for the two vertical sections of Figure 4.4, which cross the 2012 Haida Gwaii earthquake epicenter with each of the two DART stations. As it can be noted the earthquake's horizontal extension for these sections is about 200 km.

deformation, which for each point distant r from the epicenter, is obtained as $t_0 = r/V_r$.

4.2.1 Hydro-acoustic wave model

The modeling of hydro-acoustic waves has been carried out by solving the MSEWC (2.16) for $n \geq 1$ and for a number of frequencies within a finite range. The simulation of a full 3D model in the whole area of interest is unreasonably computationally expensive, therefore validation of MSEWC has been carried out by comparison with the solution of the complete 3D problem expressed by equation (2.4), along vertical cross sections of the computational domain. The orientation of these two sections is shown in Figure 4.4 and chosen as the line intersecting the earthquake epicenter and each of the two DART stations. Figure 4.5 shows the water depth, h_b, and the residual sea-bed dislocation, ζ_0, along the two cross sections. The comparison of the two models has been done for different points along both cross sections, presenting an overall good agreement. Figure 4.6 shows the comparison at the position of the two DART stations. The panel a and b refer to the results at D_{19} in section 1, while panel c and d refer to the results at D_{04} in section 2.

In Figure 4.6, the pressure signals at the sea-bottom both in time (panels a and c) and frequency (panels b and d) domains are shown. In each panel, the upper plot presents the solution of the 3D problem, while the lower plot presents the MSEWC solution. The two models provide similar results in the time domain, where arrival time and propagation features of the hydro-acoustic modes show good agreement, even if just the first hydro-acoustic mode has been reproduced and the limited frequency range $f = 0.1$ - $0.8\ Hz$ has been solved using the MSEWC. These comparisons validate the depth-integrated equation for real bathymetry and enable us to optimize the model. It has been further verified that the reproduction of frequencies outside of the range $f = 0.1$ - $0.8\ Hz$, and relative to second and higher hydro-acoustic modes, increases the computational costs without providing a substantial improvement of the results accuracy.

In order to investigate how the variable bathymetry affects the hydro-acoustic wave propagation, four positions along the vertical section 2 have been selected (see panel (a) of Figure 4.7): point A and B are located on the earthquake zone at 1200 and 2900 m water depth; point C and D are 250 and 500 km far from epicenter at 2950 and 2700 m water depth respectively. Figure 4.7 presents the frequency spectra of the numerically reproduced bottom pressure perturbations for these four positions: panels b, c, d an e respectively for the positions A, B, C and D.

Hydro-acoustic waves oscillate at the resonating frequency, given for each mode by equation (4.2), which is therefore inversely proportional to the water depth where these waves are generated. This resonating frequency $f^{(n)}$, namely cut-off frequency (*Tolstoy*; 1963), identifies at each water depth the lower limit of frequencies associated with propagating modes, whereas $f < f^{(n)}$ are characteristic of evanescent modes. In the case of section 2, where the source area covers the shallowest and deepest depths along the section, the minimum frequency for the first mode is 0.13 Hz for the

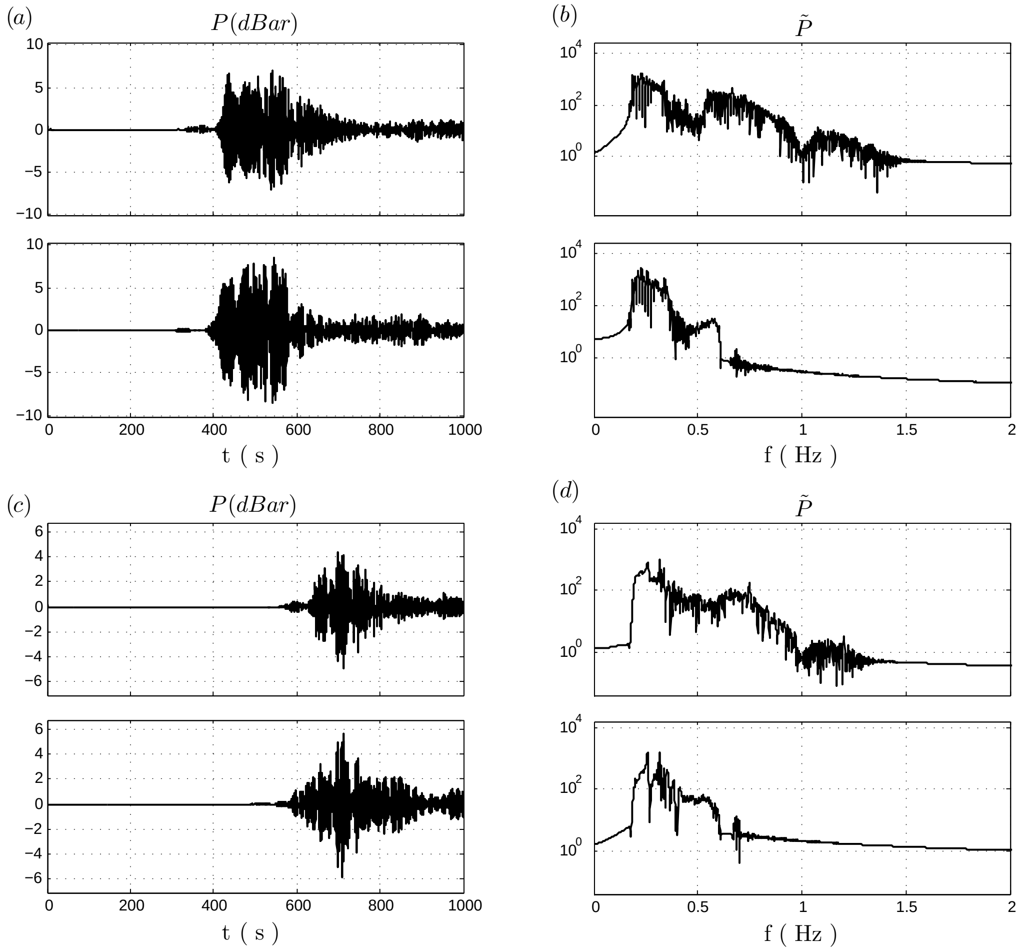

Figure 4.6: Pressure time series (left column) and their frequency spectra (right column) at D_{19} (a, b) and at D_{04} (c, d). Comparison between the solution of the 3-D reference model (upper plots) and the solution of the depth-integrated equation (lower plots).

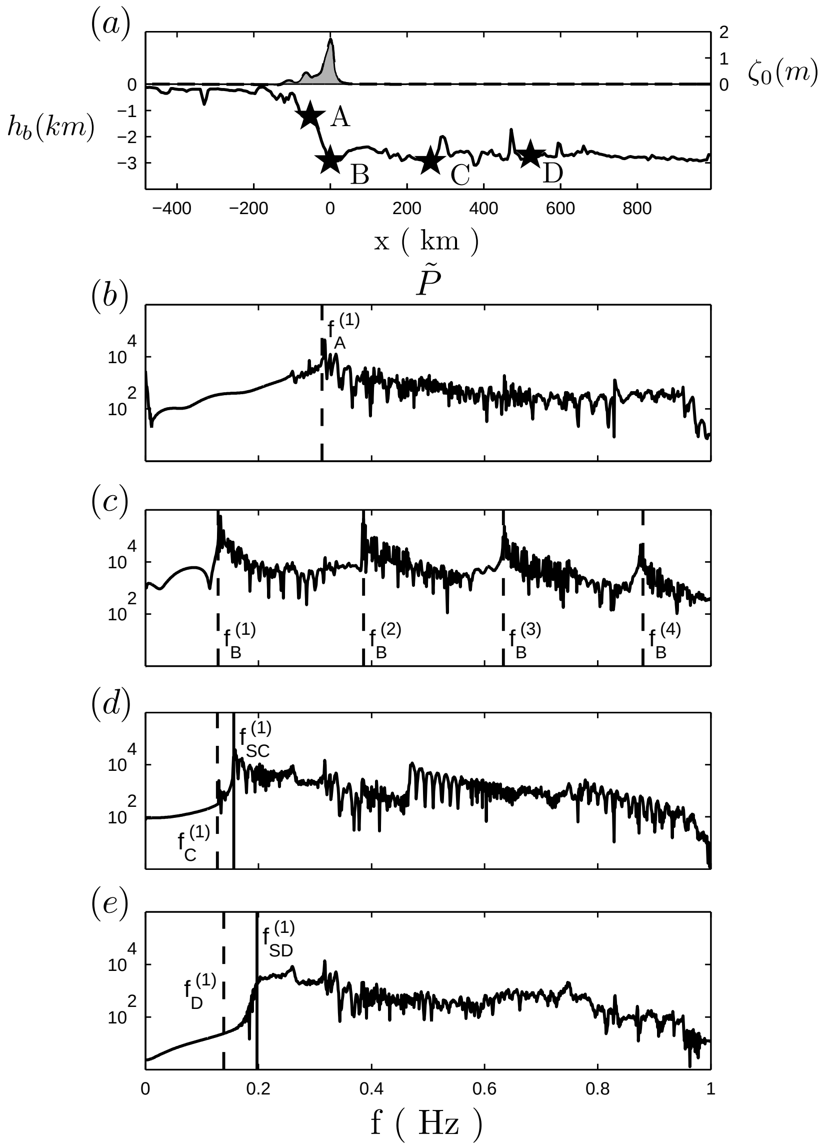

Figure 4.7: Sea bed pressure spectra computed solving the 3D wave equation. The panel (b) to (e) respectively refer to points A (h=1220 m), B (h=2916 m), C (h=2945 m) and D (h=2705 m) along the section reported in the upper panel (a). The dashed lines indicate the natural acoustic frequencies corresponding to observation depth while the solid lines represent the first acoustic mode for the minimum water depth between generation area and observation point.

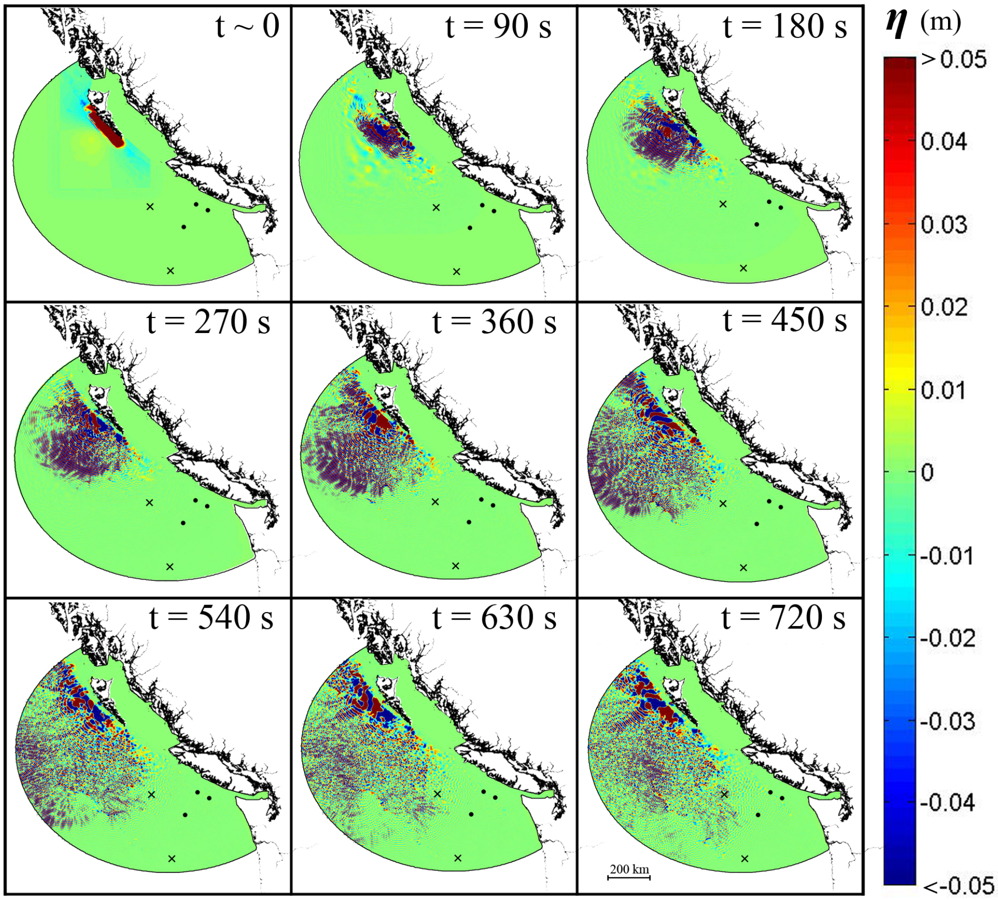
t ~ 0
t = 90 s
t = 180 s
t = 270 s
t = 360 s
t = 450 s
t = 540 s
t = 630 s
t = 720 s
200 km
η (m)
>0.05
0.04
0.03
0.02
0.01
0
-0.01
-0.02
-0.03
-0.04
<-0.05

Figure 4.8: Snapshots of the free surface (η) hydro-acoustic perturbation given by the 2012 Haida Gwaii earthquake. The three points identify the positions of the three Neptune stations, while the two crosses the positions of the DART stations. t = 0 refers to the time of occurrence of the earthquake.

depth of 2950 m. Traveling into shallower water or over sea mounts, the shallower depths do not let the frequencies lower than $f^{(n)}$ to propagate. Panel (b) of Figure 4.7 shows with the vertical dashed line the cut-off frequency of the first mode at the local water depth ($f_A^{(1)}$=0.31 Hz) and it is distinguishable that the pressure signal is filtered for frequencies lower than $f_A^{(1)}$. Panel (c) presents the pressure spectrum at the observation point located on the maximum sea-bed dislocation at 2900 m water depth; here the spectrum presents higher peaks on the first four acoustic modes $f_B^{(1)}$=0.13, $f_B^{(2)}$=0.38, $f_B^{(3)}$=0.64 and $f_B^{(4)}$=0.88 Hz (dashed lines). Propagating away from the source zone, the spectrum can be enriched and filtered by higher frequencies representing shallower water normal modes. To reach point C, only frequencies higher than $0.16Hz$ cross the shallower area. The solid line in panel (d) represents the first acoustic mode for the minimum water depth between generation area and point C with 2400 m water depth ($f_{SC}^{(1)}$=0.16 Hz). Although the first acoustic mode corresponding to local water depth of point C ($f_C^{(1)}$=0.12 Hz), shown by dashed line, allows waves with lower frequencies to pass, the spectrum is previously filtered by the shallower area. Panel (e) emphasizes that a higher barrier before point D with 1900 m water depth has barricaded propagation of pressure waves with frequencies lower than $0.2Hz$ ($f_{SD}^{(1)}$).

In order to correctly reproduce the hydro-acoustic wave field by means of Finite Element Method in the domain of Figure 4.2, a maximum element mesh size of 1 km has been chosen, for a total number of 3,000,000 triangular elements. Solutions were obtained using a high-speed computer equipped with 12 cores i7 3.20 GHz CPU and 64GB RAM. The computational time for solving 720 s with a time step of 0.05 s was about 600 hours. The results of this large scale simulation are shown in Figure 4.8 in term of free-surface elevation, $\eta(x, y, t)$. It can be seen that a complicated perturbation is formed at the free surface and propagates at the sound celerity in water over the entire domain in 12 minute after the event. The wave field shows that the hydro-acoustic waves do not propagate upslope; maximum values of hydro-acoustic wave amplitude are in deeper water close to the generation area. Spectrograms of bottom pressure are presented in Figure 4.9 for three Ocean Neptune Canada observatories and three selected points in front of active fault at different water depths, as shown in Figure 4.4. Each spectrogram is normalized by dividing the maximum value among all six points in order to show the ratio of wave amplitudes at different distances and depths. The local

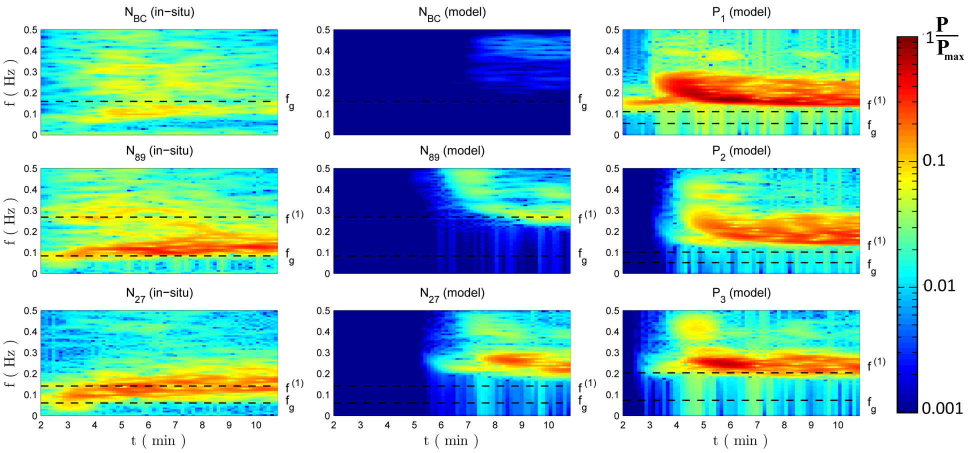

Figure 4.9: Spectrograms of the bottom pressure normalized by dividing by maximum value (P/P_{max}). The first column refer to the in-situ bottom pressure recorded at N_{BC}, N_{89} and N_{27}; the second and third columns of plots refer to the simulated hydro-acoustic bottom pressure at the Neptune stations and at points P_1, P_2, P_3 depicted in Figure 4.4.

characteristic gravitational wave frequency f_g and first acoustic mode $f^{(1)}$ are shown by horizontal lines. The arrival time of low-frequency hydro-acoustic signals, traveling with sound celerity in water from the nearest part of the assumed fault is correctly estimated by the model. Regarding the frequency range of bottom pressure records, we have divided extraction points into three categories: 1. deeper than source area, 2. shallower than source area and 3. within source area depth. The Points P_1 and P_2 fall into category 1 are at 3400 and 3700 m water depths. Therefore, it is expected that points P_1 and P_2 capture all the frequency range generated at the source. At category 2 N_{BC} and N_{89} observatories, where the cut off frequency is higher than the first acoustic mode at source area ($f^{(1)}$=0.31 Hz), the majority of waves cannot reach the observatory stations. In other words, at stations located in a shallow depth like N_{BC}, the model calculates tiny pressure wave with large frequencies. It shows that the spectrum has been filtered while ascending the slope. Similarly, at N_{89} station, the pressure waves with frequencies lower than $f^{(1)}$=0.3 Hz at water depth of 1258 m, has not reached the observatory. Point P_3 (category 3) is located at 1850 m depth, hence, it can capture the

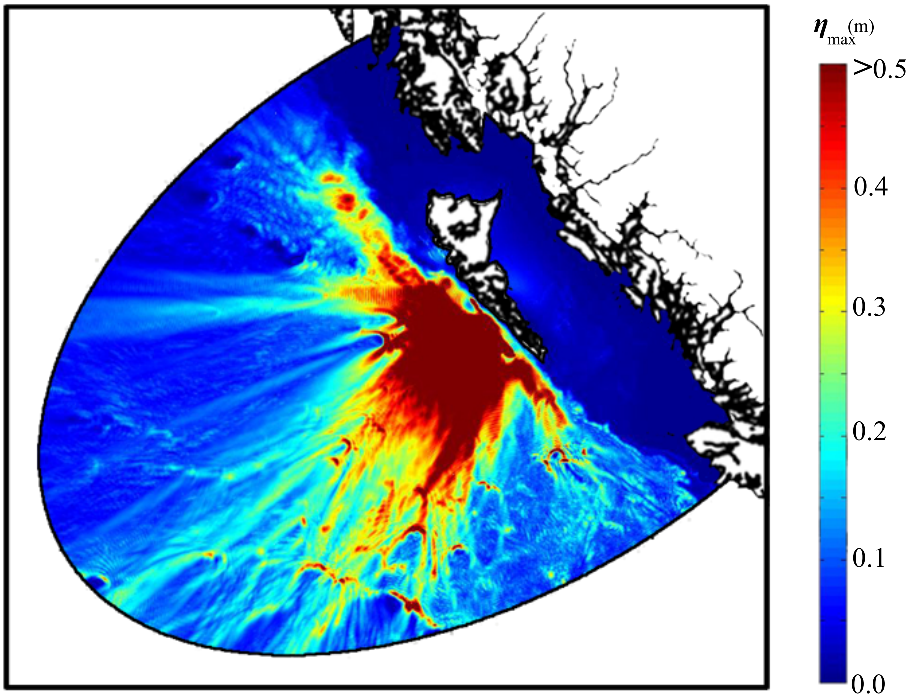

Figure 4.10: Maximum absolute values of the free surface (η_{max}) of the hydro-acoustic wave generated by the Haida Gwaii earthquake on October 28, 2012.

wave frequencies higher than 0.2 Hz. Although the point N_{27} is deep enough to capture wave frequencies larger than 0.14 Hz, it is surrounded by shallower areas and the majority of waves have been filtered before reaching point N_{27}. The results of numerical simulation are shown in Figure 4.10, in terms of maximum absolute water level. Here the propagation path of hydro-acoustic waves towards deep sea orthogonal to fault plane can be interpreted as waves propagate farther, their energy spreads and their intensity decreases. The scattered sea-mounts restrict passage of the lower frequencies.

4.2.2 Tsunami waves

Numerical simulation of the long gravitational waves generated by the 2012 Haida Gwaii earthquake has been performed by solving for the zero mode of the MSEWC (equation 2.16). As for the hydro-acoustic modes equation

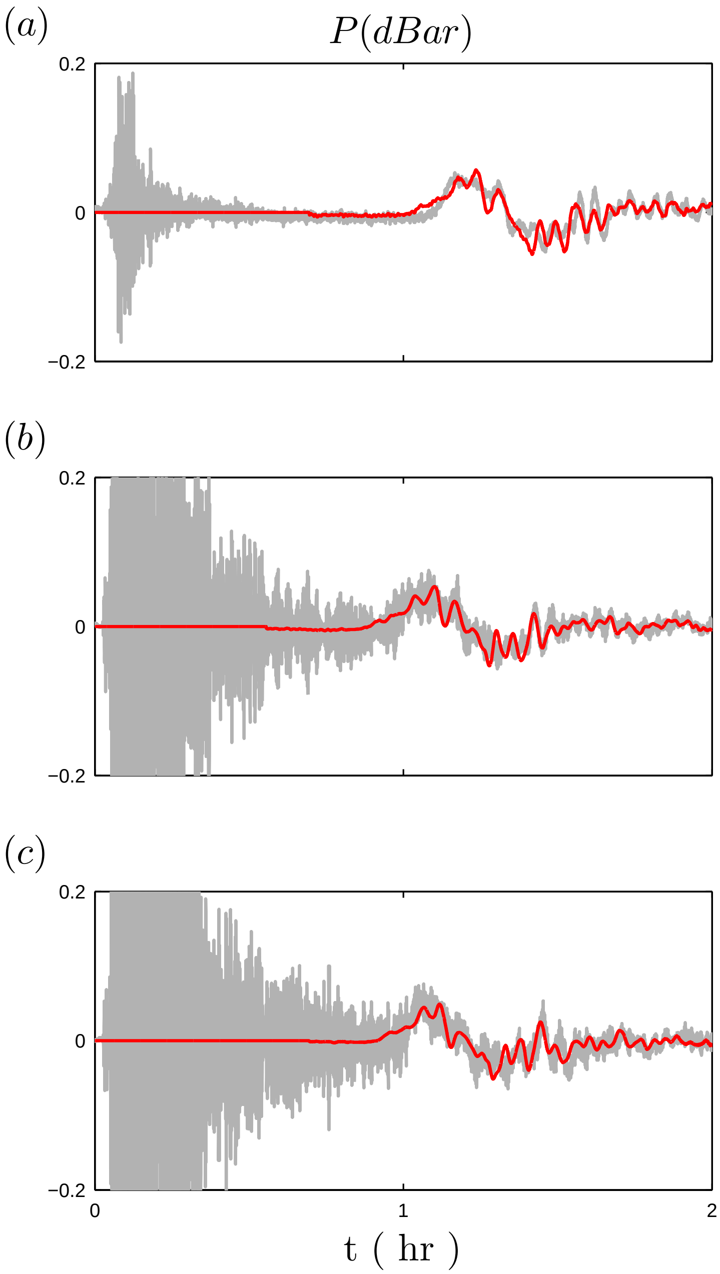

Figure 4.11: Pressure time series as measured by the NEPTUNE observatories (gray lines) and as calculated by the model for gravity wave (red lines). Panels (a), (b) and (c) correspond to N_{BC}, N_{89} and N_{27} respectively. t = 0 refers to the time of occurrence of the earthquake.

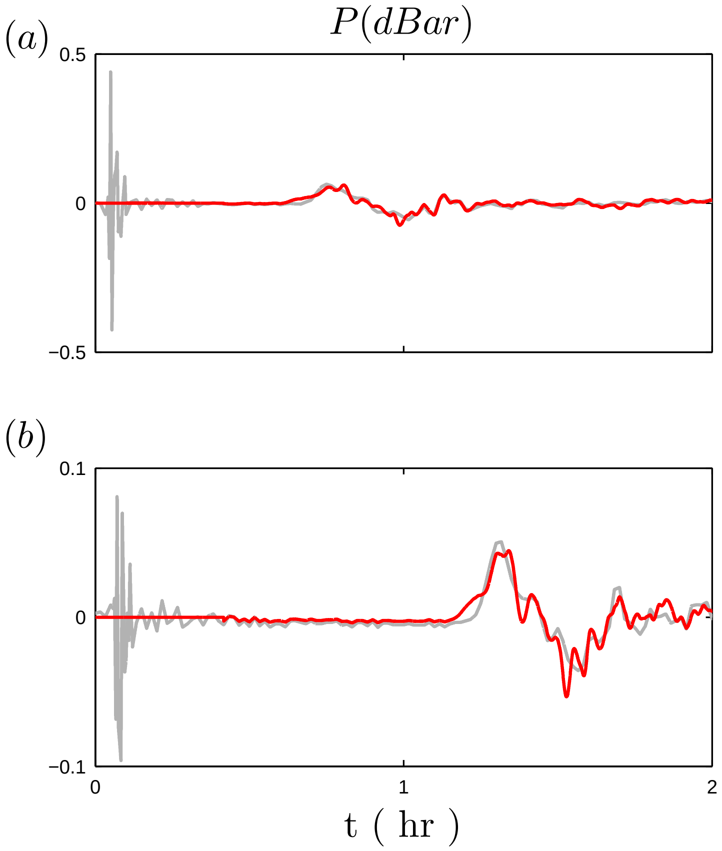

Figure 4.12: Pressure time series as measured at DART buoys (gray lines) and as calculated by the model for gravity wave (red lines). The panels (a) and (b) correspond to D_{19} and D_{04} stations respectively. t = 0 refers to the time of occurrence of the earthquake.

(2.16) is solved by means of Finite Element Method on the numerical domain, which has been discretized in triangular elements with a maximum size of 2.5 km. The computational time is 12 hours (on the same computer described in section 4.2.1) for simulation of 2 hours real time. The frequencies in the range f = 0 - 0.03 Hz, with a df = 0.002 Hz, have been solved to reconstruct the gravitational wave field. Results of the zero mode simulation are presented in Figures 4.11 and 4.12, in terms of bottom pressure time series at the Ocean Network Canada observatories and at the DART buoys respectively. In both figures, the red lines show the results of the numerical model, while the gray lines represent the pressure signals recorded at the instruments. The model simulates the tsunami wave magnitude and arrival time properly compared with observation.

In Figure 4.11 the panels a, b and c refer respectively to the observatories N_{BC}, N_{89} and N_{27}. The comparison between the model and the field data at the Neptune Canada observatories is in good agreement in terms of amplitude, period and arrival time of the pressure signal given by the long gravity wave transit. The field pressure data, however, include the pressure variation given by the ground motion and the precursor waves. Figure 4.12 shows the comparison results at the DART station D_{19}, panel a, and D_{04}, panel b. Both numerical and field data reveal that tsunami waves arrived at point D_{19} and D_{04}, respectively 35 and 70 minutes after the event. Although the sampling frequency of DART records is not sufficient to resolve the fast elastic oscillation and low-frequency hydro-acoustic waves (0.066 Hz), there is some perturbation few minutes after the earthquake. The bottom displacement has not occurred at the mentioned points, keeping in mind that DART stations are far from epicenter and not located on the subduction zone. Even neglecting the missing peaks due to low sampling frequency of DART buoys, the low-frequency wave peaks in the available time series are larger than the following tsunami waves (0.5 and 0.1 dBar correspond to D_{19} and D_{04}). Figure 4.13 depicts the time history of generation and propagation of tsunami waves in the computational domain. The plot shows that the residual bottom dislocation is almost transferred to the sea surface. The wave front starts spreading and covers the entire domain after 2 hours. Comparison between Figures 4.8 and 4.13 shows that, except during the first stages of the generation process, the significant difference between the speed of low-frequency and tsunami waves leads to the different location of hydro-acoustic and tsunami waves fronts in time.

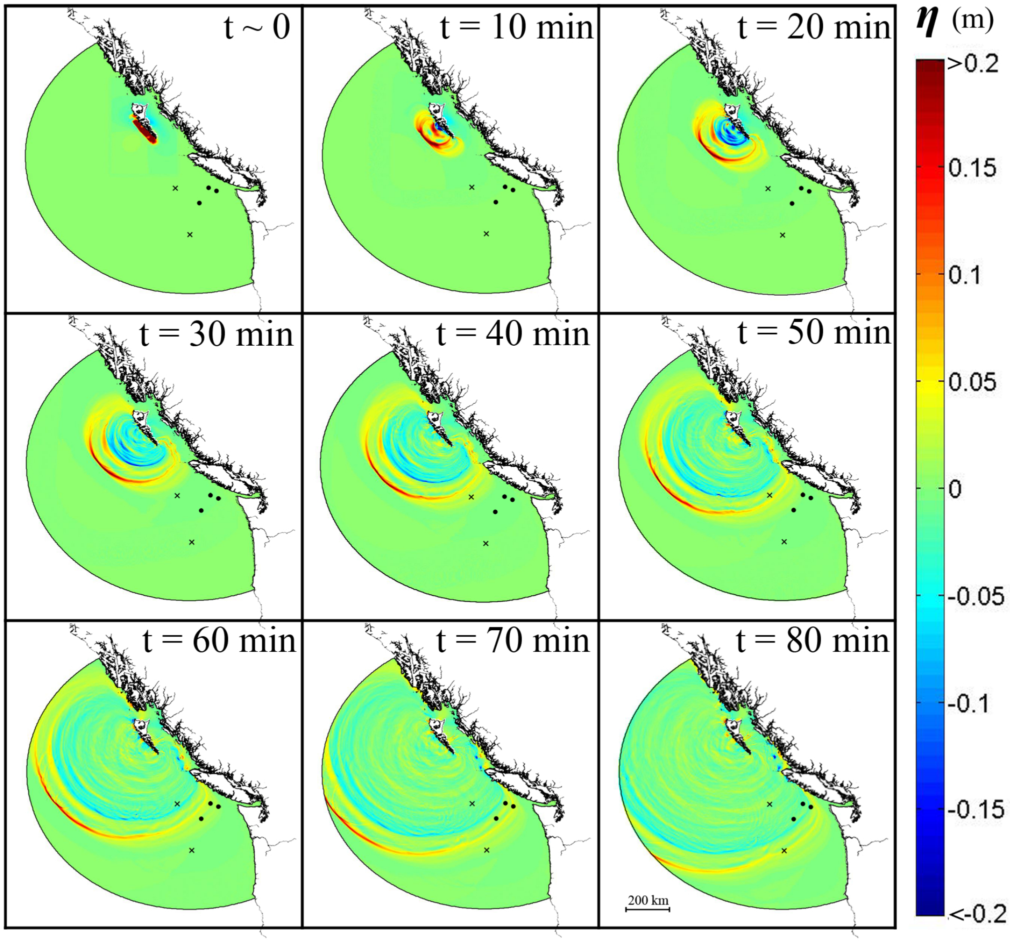
t ~ 0
t = 10 min
t = 20 min
t = 30 min
t = 40 min
t = 50 min
t = 60 min
t = 70 min
t = 80 min
200 km
η (m)
>0.2
0.15
0.1
0.05
0
-0.05
-0.1
-0.15
<-0.2

Figure 4.13: Snapshots of the free surface (η) gravity wave perturbation given by the 2012 Haida Gwaii earthquake. The three points identify the positions of the three Neptune stations, while the two crosses the positions of the DART stations. t = 0 refers to the time of occurrence of the earthquake.

4.3 Conclusions

Reproduction of long gravitational waves spreading proportional to square root of the water depth, and low-frequency hydro-acoustic waves traveling with the sound celerity in water, have been studied for 2012 Haida Gwaii earthquake in the framework of linear potential theory, using a hyperbolic mild-slope equation for weakly compressible fluids (MSEWC, *Sammarco et al.*, 2013). Here we show the second application of MSEWC to numerically reproduce wave generation and propagation in weakly compressible fluid in a large scale domain, overcoming the computational difficulties of three-dimensional models. The numerical model is validated against a fully 3D linear model for the case of varying water depth. The comparison has been done in order to understand the physics of low-frequency propagation in the far-field in order to utilize deep sea observatories for enhancement of TEWS. At present, the 2D numerical model is not able to reproduce the intensity of hydro-acoustic wave field. However, it shows the importance of deep sea observatories where the depth effect does not affect the arriving wave spectrum. It is worth citing that due to the lack of knowledge about spatio-temporal bottom motion in numerical modeling the calculation for hydro-acoustic waves is still a rough estimate of the exact result. In other words, we have assumed sea bottom deformation spreads uniformly from epicenter ($V_r = 2.3km/s$) taken place with mean bottom displacement duration ($\tau = 6.23s$) in a certain rectangular fault. Therefore, the aftershocks and tiny bottom motions along the active fault orientation, responsible for local elastic waves, are neglected. In addition, the role of bottom elasticity of porous sedimentary layer in decay of hydro-acoustic waves (*Chierici et al.*, 2010) is neglected. The underlying sedimentary layer causes a shift of dominant spectral peaks toward lower values (*Abdolali et al.*, 2015b). This behavior depends on sediment thickness and density. More importantly, damping of hydro-acoustic waves due to diffraction at sea bottom and through porous medium is caused by high bulk viscosity of sediment. The bulk viscosity of sediment causes a shift of spectral peaks to lower frequency values as well as damping. For very large bulk viscosity, the result for rigid and porous bottom is the same (*Chierici et al.*, 2010; *Abdolali et al.*, 2015b).This has motivated the research presented in the next chapter where the bottom layer is taken into account. On the other hand, comparison of long gravitational wave records from Ocean Network Canada observatory and DART buoys with numerical results shows that assumption of rigid bottom without sedimentary layers is reasonable for long gravitational wave. Analysis of bottom pressure records shows the role of sea bottom topography on the generation of normal acoustic modes. While the pressure waves spread out, the sea mounts and shallower areas filter the spectrum. This fact demonstrates the necessity of deep-sea observatory for proper hydro-acoustic detection. Results presented in this chapter point out practical suggestions for deep sea observatory deployment near potential tsunamigenic zones. The availability of seismograms recorded at the observatories allows the interpretation of signals in order to distinguish the local generated elastic waves. The complete modeling of these waves could, in principle, dramatically improve the effectiveness of a TEWS (*Chierici et al.*, 2010), given the recent advances in deep-sea measurement technology.

Chapter 5

Depth-Integrated Equation for Hydro-acoustic Waves with Bottom Damping

In this chapter, we present a depth-integrated equation for the mechanics of generation, propagation and dissipation of low frequency hydro-acoustic waves due to sudden bottom displacement in a weakly compressible ocean overlying a weakly compressible viscous sediment layer. The model is validated against a full 3D computational model. Physical properties of these waves are studied and compared with those for waves over a rigid sea bed, revealing changes in frequency spectrum and modal peaks. The resulting model equation can be used for numerical prediction in large-scale domains, overcoming the computational difficulties of 3D models while taking into account the role of bottom dissipation on hydro-acoustic wave generation and propagation.

Although presented depth-integrated model in chapter 2 could reproduce the long gravitational wave field satisfactorily in comparison with observed data during Haida Gwaii 2012 tsunami event (chapter 4), the model could not be able to reconstruct hydro-acoustic wave field correctly. It can be due to lack of knowledge about spatiotemporal sea bed deformation and, more importantly, neglecting the role of the underlying sediment layer.

Section 5.1 provides an overview of results motivating the need to include compressibility effects in the sediment layer. Section 5.2 describes the derivation of the depth integrated model in the mild slope approximation. Verification of the depth-integrated model is carried out for constant and varying geometries against a fully 3D model in Section 5.3. Conclusions are given in Section 5.4.

5.1 The role of the sediment layer

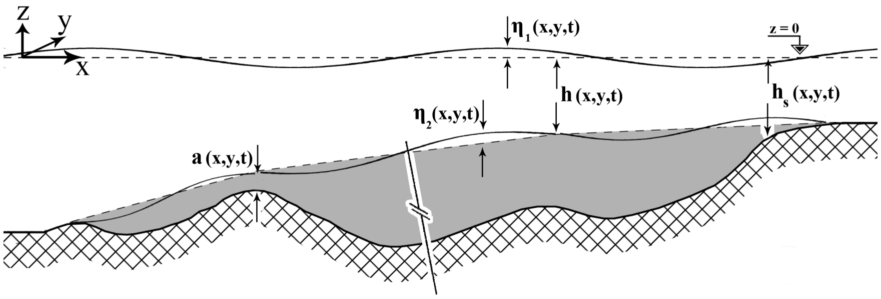

Figure 5.1: schematic view of fluid domain

The role of a porous sea bed in attenuating hydro-acoustic waves has been investigated by *Chierici et al.* (2010). They proposed two theoretical solutions for constant water depth, the first based on compressible sea water and an incompressible sediment layer using Darcy equations. The second model is based loosely on the work of *Buckingham* (1997), who showed that the effect of intergranular stresses in an unconsolidated sediment plays the role of an apparent viscous dissipation added to the dissipation associated with the pore water percolation; this model serves as the basis for the derivation in Section 5.2. *Eyov et al.* (2013) have investigated the role of an elastic sea bed on progressive waves and found that the first acoustic mode ($n = 1$) is the dominant component of the hydro-acoustic wave field. Here, we consider the interaction of a train of hydro-acoustic waves in a water column of depth $h(x, y, t)$ overlying a sediment layer of thickness $a(x, y, t)$, with $h_s = h + a$ where $h_s(x, y, t)$ is the total depth. The vertical coordinate, z, is measured positively upwards from the undisturbed free surface at $z = 0$, and x and y denote horizontal Cartesian coordinates as shown in Fig. 5.1.

The sediment layer causes the damping of hydro-acoustic waves, lowering the whole energy spectrum and shifting the expected frequency peaks toward lower values [*Chierici et al.*, 2010]. In the absence of viscous behaviour of sea bottom, the dominant frequency range in the wave spectrum can be expressed by a discrete set of normal frequencies f_n given by

$$f_n = (2n-1)\frac{c}{4h}, \qquad n = 1, 2, 3, \cdots \tag{5.1}$$

where c is sound speed in water (about 1500 m/s). Introducing the underlying sediment layer acting together with water column causes lowering the spectrum peaks determined from the following transcendent equation [*Nosov et al.*, 2007]:

$$\tan\left[\frac{2\pi\gamma_n h}{c}\right]\tan\left[\frac{2\pi\gamma_n a}{c_s}\right] = \frac{\rho_s c_s}{\rho c} \tag{5.2}$$

where c_s is sound speed in sediment, ρ and ρ_s are water and sediment density respectively, and γ_n denotes the normal mode frequencies for the damped case. Note that in the case of $a = 0$, the set of normal modes described by Eqs. (5.1) and (5.2) coincide.

A sample computation is carried out using a full 3D solver in constant depth. The governing equations within layers and boundary conditions at free surface, interfacial and bottom for sample computation are described in Section 5.2. We use $h = 2200m$, $a = 1000m$, $c = 1500m/s$, $c_s = 2000m/s$, $\rho = 1000kg/m^3$ and $\rho_s = 1850kg/m^3$. The other parameters are for a unit sudden elevation of source area with semi-length $b = 112km$ and rise time $\tau = 1s$. The transient sea bed velocity, h_t, with a residual displacement h_0, is a trigonometric function expressed by

$$h_t = \frac{h_0}{2}\left[1-\cos\left(\frac{2\pi(t-t_0)}{\tau}\right)\right]\left[H(t-t_0) - H(t-t_0-\tau)\right], \tag{5.3}$$

where $H(t)$ is the Heaviside step function. The results are depicted in Fig. 5.2, which show the bottom pressure P and the corresponding frequency spectrum $\tilde{P}$ at 96 km from the epicenter. In panel (a), the light gray line shows the time series of bottom pressure from one layer compressible water model while the black line shows the results from a coupled model of two layers of compressible water and sediment without damping term ($\mu_s = 0$) in lower layer. In panel (b), for one layer model, the frequency peaks coincide with the cut off frequencies for ideal impermeable bottom ($f_1 = 0.17$ and $f_2 = 0.51Hz$, ...) identified by Eq. (5.1). For the case of coupled model, the spectrum is peaked at $\gamma_1 = 0.15$ and $\gamma_1 = 0.407Hz$, representing cut off frequencies evaluated by Eq. (5.2). In order to consider the damping behaviour of the underlying sediment layer, the bulk viscosity (ranging from 10^6 up to 10^{20} Pa s (*Kimura*, 2006; *Van Keken et al.*, 1993)) is fixed at 2×10^8 Pa s. The model results are compared with a one layer model with an additional partially reflective boundary condition at bottom defined by Eq. (5.4)

$$\Phi_z = \frac{1}{c}\frac{K_r - 1}{K_r + 1}\Phi_t, \tag{5.4}$$

where K_r is the amplitude reflection coefficient (*Brekhovskikh et al.*, 2003),

$$K_r = \frac{\rho_s c_p - \rho c}{\rho_s c_p + \rho c}, \tag{5.5}$$

and c_p is the P-wave speed in bottom. This boundary condition causes decay of hydro-acoustic waves peaking at the cut off frequencies (f_n) defined by Eq. (5.1). In panel (c), the light gray line shows the time series of bottom pressure from one layer compressible model with damping coefficient. $c_p = 8000 m/s$ is selected for computations. Thus, the reflection coefficient takes the value of $K_r \approx 0.816$. It can be seen from the plot that the oscillation lasts for 80 s after the earthquake. The lower time series is for a two layers model with dissipation term in sediment (black). The attenuation of hydro-acoustic waves lasts for 500 s. The corresponding frequency spectra are shown in panel (d). Lowering the whole energy spectrum in comparison with panel (b) is distinguishable. Comparison shown in Fig. 5.2 justifies the mismatch between the calculated spectral peaks for impermeable bottom, f_n, and dominant frequencies, γ_n, observed during Tokachi Oki 2003 event (*Nosov et al.*, 2007).

5.2 The mild-slope equation for damped hydro-acoustic waves

We develop a mild slope equation based on the eigenfunction structure for the problem with constant layer depths h and $a = h_s - h$ and with no lower layer damping. We review the governing equations and boundary conditions here and then derive the damped, two-layer mild-slope model using an approach described in *Silva et al.* (2003).

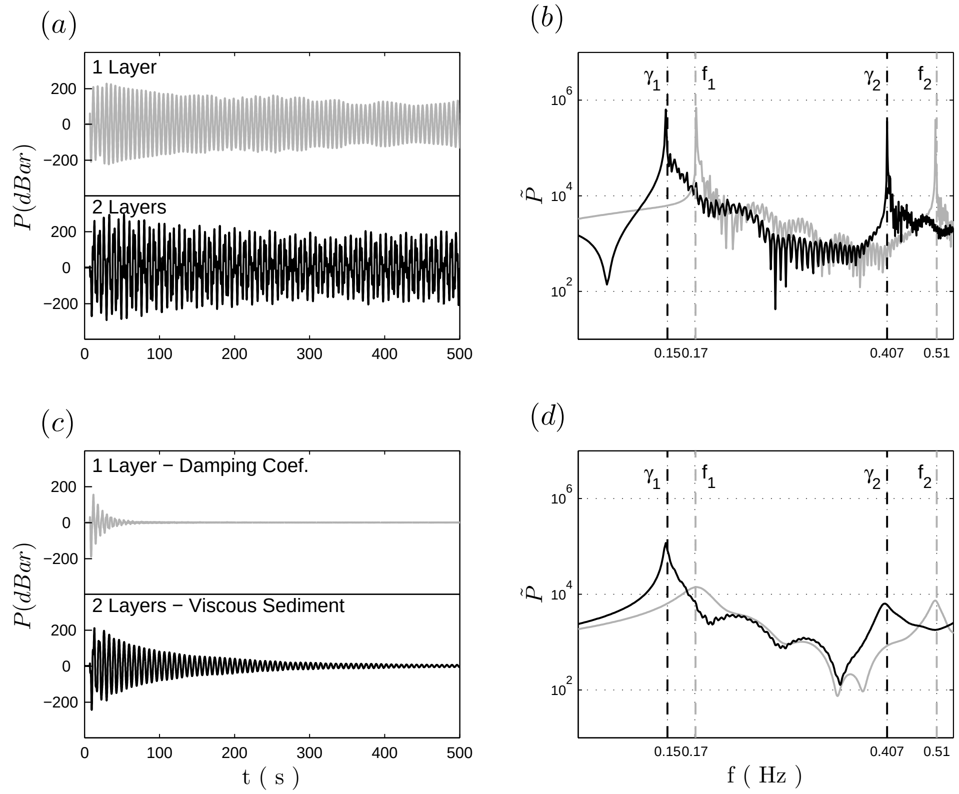

Figure 5.2: Bottom pressure records at a distance of $x = 96km$ from epicenter, results of a sample computation carried out using a 3D flow solver in a constant depth, $h = 2200m$, $a = 1000m$, $c = 1500m/s$, $c_s = 2000m/s$, $\rho = 1000kg/m^3$, $\rho_s = 1850kg/m^3$ for a unit source area with semi-length $b = 112km$ and rising time $\tau = 1\ s$, showing (a) Time series of a one layer compressible water model in light gray and a coupled model of compressible water and inviscid compressible sediment in black, $\mu = 0$, (b) the corresponding frequency spectrum of panel (a), (c) Time series of a one layer compressible water model with partial reflection boundary condition (Eq. 5.4) at bottom in light gray and a coupled model of compressible water and viscous compressible sediment, $\mu_s = 2 \times 10^8 Pas$, in black and ($d$) the corresponding frequency spectrum of panel (c). The vertical dashed lines at panels (b) and (d) represents the frequency peaks calculated by Eqs. (5.1) and (5.2) in light gray and black respectively.

5.2.1 Governing equations

The linearized weakly compressible wave equation governing the fluid potential $\Phi(x, y, z, t)$ in the water layer is given by

$$L(\Phi) = \Phi_{tt} - c^2\nabla^2\Phi = 0; \quad -h + \eta_2(x, y, t) \leq z \leq \eta_1(x, y, t), \tag{5.6}$$

where ∇^2 is the Laplacian in 3D and subscripts on dependent variables denote partial derivatives. The interfacial displacements η_1 and η_2 represent response of the free surface and layer interface to hydro-acoustic disturbances. Following *Buckingham* (1997) and *Chierici et al.* (2010), the weakly compressible wave equation for fluid potential $\mathcal{Q}(x, y, z, t)$ in the viscous sediment layer is given by

$$L_s(\mathcal{Q}) = \mathcal{Q}_{tt} - c_s^2\nabla^2\mathcal{Q} - 2\nu_s(\nabla^2\mathcal{Q})_t = 0; \quad -h_s \leq z \leq -h + \eta_2(x, y, t) \tag{5.7}$$

with apparent sediment kinematic viscosity ν_s. The boundary conditions at free surface and bottom are given by

$$\begin{cases} \Phi_{tt} + g\Phi_z = 0 & \text{at} \quad z = 0 \\ \mathcal{Q}_z + \nabla_h h_s \cdot \nabla_h \mathcal{Q} + h_{s,t} = 0 & \text{at} \quad z = -h_s \end{cases} \tag{5.8}$$

where ∇_h is the horizontal gradient operator and $h_{s,t}$ is the vertical bottom velocity representing displacement of the impermeable substrate. Matching conditions at the water-sediment interface $z = -h + \eta_2$ consist of continuity of pressure and kinematic constraints for each layer. After linearizing with respect to the pressure perturbation and small interface displacement, the resulting conditions are

$$\left\{ \begin{array}{l} (R-1)g\eta_2 = \Phi_t - R\mathcal{Q}_t \\ W_w = W_s = (-h + \eta_2)_t \end{array} \right. \text{at } z = -h \tag{5.9}$$

where $R = \rho_s/\rho$. The normal velocities at the interface inside the water column, W_w, and sediment, W_s, are given by:

$$\left\{ \begin{array}{l} W_w = \Phi_z + \nabla_h h \cdot \nabla_h \Phi \\ W_s = \mathcal{Q}_z + \nabla_h h \cdot \nabla_h \mathcal{Q} \end{array} \right. \text{at } z = -h \tag{5.10}$$

5.2.2 Derivation of the mild slope equation

A nondimensionalization of the sediment layer equation yields a parameter $\epsilon = \omega\nu_s/c_s^2$ characterizing the size of the damping term relative to the undamped wave equation, where ω represents angular wave frequency. For the cases considered here, $\epsilon = O(10^{-1})$, and we treat the damping effect as a perturbation to the leading order inviscid problem. The mild-slope equation is developed using the eigenfunctions for the two-layer, inviscid, compressible fluid problem with constant layer thicknesses h and $a = h_s - h$ and a free surface. Retaining damping in the lower layer eigenfunctions, as in *Silva et al.* (2003), would eliminate the leading order damping term in the model but would involve complex-valued separation constants and resulting complex-valued model coefficients.

The upper and lower layer potentials may be expanded according to

$$\Phi\left(x,y,z,t\right) = \sum_{n=0}^{\infty} \Phi_n\left(x,y,z,t\right) = \sum_{n=0}^{\infty} \psi_n\left(x,y,t\right) M_n\left(z\right) \tag{5.11}$$

for the water column and

$$\mathcal{Q}\left(x,y,z,t\right) = \sum_{n=0}^{\infty} \mathcal{Q}_n\left(x,y,z,t\right) = \sum_{n=0}^{\infty} \psi_n\left(x,y,t\right) N_n\left(z\right) \tag{5.12}$$

in the sediment layer. For simple harmonic motion with frequency ω and separation constant β^2 in the vertical, the eigenfunctions $M_n(z)$ and $N_n(z)$ for the upper and lower layers are given by

$$M_n = \frac{(1-\lambda_n \mathrm{T}_n)\cosh\left(\beta_{w,n}(h+z)\right) + (\lambda_n - \mathrm{T}_n)\sinh\left(\beta_{w,n}(h+z)\right)}{(1-\lambda_n \mathrm{T}_n)\cosh\left(\beta_{w,n}h\right) + (\lambda_n - \mathrm{T}_n)\sinh\left(\beta_{w,n}h\right)} \tag{5.13}$$

$$N_n = \frac{(\lambda_n - \mathrm{T}_n)\cosh\beta_{s,n}(h_s+z)}{\alpha_n \sinh\left(\beta_{s,n}a\right)\left[(1-\lambda_n \mathrm{T}_n)\cosh\left(\beta_{w,n}h\right) + (\lambda_n - \mathrm{T}_n)\sinh\left(\beta_{w,n}h\right)\right]} \tag{5.14}$$

where $\mathrm{T}_n = \tanh\left(\beta_{w,n}h\right)$, $\lambda_n = \omega^2/g\beta_{w,n}$ and $\alpha_n = \beta_{s,n}/\beta_{w,n}$. The separation constants $\beta_{w,n}$ and $\beta_{s,n}$ for water and sediment layers respectively are given by

$$\beta_{w,n}^2 = k_n^2 - \frac{\omega^2}{c^2}; \quad \beta_{s,n}^2 = k_n^2 - \frac{\omega^2}{c_s^2} \tag{5.15}$$

where k_n is the wave number. The eigenfunctions M_n and N_n form a complete Sturm-Liouville basis subject to the orthogonality constraint $I_{mn} + RK_{mn} = 0; m \neq n$, where

$$I_{mn} = \int_{-h}^{0} M_m(z)M_n(z)dz; \quad K_{mn} = \int_{-h_s}^{-h} N_m(z)N_n(z)dz \tag{5.16}$$

M_n and N_n take the following values at the vertical boundaries:

$$\begin{cases} M_n = 1, \quad M_n' = \omega^2/g & \text{at} \quad z = 0 \\ M_n' = N_n' & \text{at} \quad z = -h \\ N_n' = 0 & \text{at} \quad z = -h_s \end{cases} \tag{5.17}$$

The dispersion relation governing $\beta_{w,n}$ and $\beta_{s,n}$ is given by

$$\lambda_n^2(R + \alpha_n \mathrm{T}_n \hat{\mathrm{T}}_n) - \lambda_n R(\mathrm{T}_n + \alpha_n \hat{\mathrm{T}}_n) + (R-1)\alpha_n \mathrm{T}_n \hat{\mathrm{T}}_n = 0 \tag{5.18}$$

where $\hat{\mathrm{T}}_n = \tanh(\beta_{s,n} a)$. Eq. (5.18) is a quartic system in ω describing a doubly-infinite set of surface waves (with horizontal displacements in phase at the layer interface) and internal waves (with horizontal displacements 180° out of phase). The real roots of the dispersion relation ($n = 0$) are responsible for the primary surface and internal gravity waves, while the imaginary separation variables for $n \geq 1$ describe both progressive and spatially decaying hydro-acoustic modes. Due to the presence of damping in the real problem, the internal or interfacial wave modes are expected to be rapidly damped. If $a = 0$, then there is no sediment layer and equations (5.18) reduces to the classical hydro-acoustic dispersion relation given by $\lambda_n = \tanh(\beta_{w,n} h)$. Derivation of dispersion relation for weakly compressible water column overlying a single weakly compressible sedimentary layer is described in Appendix 2.

We multiply the governing equation for each layer by each member of the set of eigenfunctions and integrate over the layer depth, giving

$$\mathrm{I}^m = \int_{-h}^{0} M_m L(\Phi) dz = 0; \qquad \mathrm{II}^m = \int_{-h_s}^{-h} N_m L_s(\mathrm{Q}) dz = 0 \tag{5.19}$$

Each expression is manipulated by introducing the expansions (5.11) and (5.12) and using Leibniz' rule and appropriate boundary conditions. Subsequently, we neglect second-order terms in interfacial and substrate slope, staying within the classic mild-slope framework. The expressions for the two layers become

$$\begin{aligned} \mathrm{I}^m \;=\; & \sum_{n=0}^{\infty} \Bigg\{ \nabla_h \cdot [I_{mn} \nabla_h \psi_n] - \left([\frac{I_{mn}}{c^2} + \frac{1}{g}] \psi_{n,t} \right)_{,t} - J_{mn} \psi_n \\ & - M_m(-h)[M_n'(-h)\psi_n + M_n(-h)\nabla_h h \cdot \nabla_h \psi_n] \\ & + \frac{1}{c^2} M_m(-h) M_n(-h) h_t \psi_{n,t} \Bigg\} \end{aligned} \tag{5.20}$$

for the water layer and

$$\begin{aligned}\mathrm{II}^m \;=\; & \sum_{n=0}^{\infty}\Bigg\{\nabla_h\cdot[K_{mn}\nabla_h\psi_n]-\left(\frac{K_{mn}}{c_s^2}\psi_{n,t}\right)_{,t}-L_{mn}\psi_n-2\epsilon\frac{\omega}{c_s^2}K_{mn}\psi_{n,t}\\ & +N_m(-h)[N_n'(-h)\psi_n+N_n(-h)\nabla_h h\cdot\nabla_h\psi_n]\\ & -N_m(-h_s)[N_n'(-h_s)\psi_n+N_n(-h_s)\nabla_h h\cdot\nabla_h\psi_n]\\ & -\frac{1}{c_s^2}\left[N_m(-h)N_n(-h)h_t-N_m(-h_s)N_n(-h_s)h_{s,t}\right]\psi_{n,t}\Bigg\}\end{aligned}\qquad(5.21)$$

for the sediment layer, where we have introduced the approximation $\nabla^2\mathrm{Q}\approx(1/c_s^2)\mathrm{Q}_{tt}\approx-(\omega^2/c_s^2)\mathrm{Q}$ in the damping term. J_{mn} and L_{mn} in (5.20) and (5.21) are given by

$$\begin{cases} J_{mn}=\int_{-h}^{0}M_m'(z)M_n'(z)dz=\frac{\omega^2}{g}-\beta_{w,n}^2I_{mn}-M_m(-h)M_n'(-h)\\ L_{mn}=\int_{-h_s}^{-h}N_m'(z)N_n'(z)dz=-\beta_{s,n}^2K_{mn}\\ \qquad\qquad+N_m(-h)N_n'(-h)-N_m(-h_s)N_n'(-h_s)\end{cases}\qquad(5.22)$$

Combining (5.20) and (5.21) according to $\mathrm{I}^m+R\mathrm{II}^m=0$ in order to take advantage of orthogonality within the spatial derivative terms, and making use the interfacial kinematic and dynamic boundary conditions, we obtain the desired mild slope equation

$$\begin{aligned}&(I_2^m\psi_{m,t})_t-\nabla_h\cdot[I_1^m\nabla_h\psi_m]+[\omega^2I_2^m-k_m^2I_1^m]\psi_m+2R\epsilon\tfrac{\omega}{c_s^2}K_n\psi_{m,t}\\ &=D_1^mh_t+D_2^mh_{s,t},\end{aligned}\qquad(5.23)$$

where we have further introduced the approximation $\psi_{n,tt}=-\omega^2\psi_n; n\neq m$ in order to eliminate an apparent coupling of the individual model equations arising in the time derivatives. Model coefficients are given by

$$I_1^m=I_{mm}+RK_{mm}\qquad(5.24)$$

$$I_2^m=\frac{I_{mm}}{c^2}+R\frac{K_{mm}}{c_s^2}+\frac{1}{g}\qquad(5.25)$$

$$D_1^m=-[M_m(-h)-RN_m(-h)]\qquad(5.26)$$

$$D_2^m=-RN_m(-h_s),\qquad(5.27)$$

where $I_{mm}(x,y,t)$ and $K_{mm}(x,y,t)$ are given by

$$I_{mm} = \int_{-h}^{0} M_m^2 dz = \frac{h}{2\mathrm{G}_1^m}[(1-2\lambda_m \mathrm{T}_m + \lambda_m^2) + (1-\lambda_m^2)\mathrm{G}_1^m] \quad (5.28)$$

$$K_{mm} = \int_{-h_s}^{-h} N_m^2 dz = \frac{h(\lambda_m - \mathrm{T}_m)^2}{2\alpha_m^3 \mathrm{T}_m \hat{\mathrm{T}}_m} \frac{1+\mathrm{G}_2^m}{\mathrm{G}_1^m} \quad (5.29)$$

with $\mathrm{G}_1^m = 2\beta_{w,m}h/\sinh(2\beta_{w,m}h)$ and $\mathrm{G}_2^m = 2\beta_{s,m}a/\sinh(2\beta_{s,m}a)$. Eq. (5.23) is the final form of the hyperbolic mild slope equation for weakly compressible fluid overlying a sediment viscous layer, MSEDWC. The time-dependence of I_2^m in (5.23) is formally required to obtain a correct energy balance in the time-dependent medium, but in practice is too weak to affect numerical results noticeably. The elliptic version for purely harmonic motion is obtained by taking the Fourier Transform of equation (5.23) and is given by

$$\nabla_h \cdot [I_1^m \nabla_h \Psi_m] + [k_m^2 I_1^m - 2iR\epsilon\frac{\omega}{c_s^2}K_m]\Psi_m = -i\omega D_1^m H - i\omega D_2^m H_s, \quad (5.30)$$

where $\psi_n(x,y,t) = \Psi_n(x,y)e^{i\omega t}$, $h(x,y,t) = H(x,y)e^{i\omega t}$ and $h_s(x,y,t) = H_s(x,y)e^{i\omega t}$. For specific conditions the Eqs. (5.23) and (5.30) give the same solution as that previously proposed by other authors, for example: if $R = 1$ or $a = 0$, then there is no sediment layer, and Eqs. (5.23) and (5.30) reduce to the equation (2.16).

5.3 Sample computations

Sample computations have been carried out to verify whether the model equation (5.23) can be safely applied in place of a more computationally expensive 3D treatment. We present results for three different domains consisting of vertical sections in x, z through laterally uniform domains with no y-dependence, first with a constant water depth and sediment thickness and the two others with varying water and sediment. Frequency bands of width $\Delta f = 0.02Hz$ have been selected to discretize the forcing spectrum. For the first case, the numerical solvers are applied on a computational domain 200 km long; given the symmetry of the problem about the middle

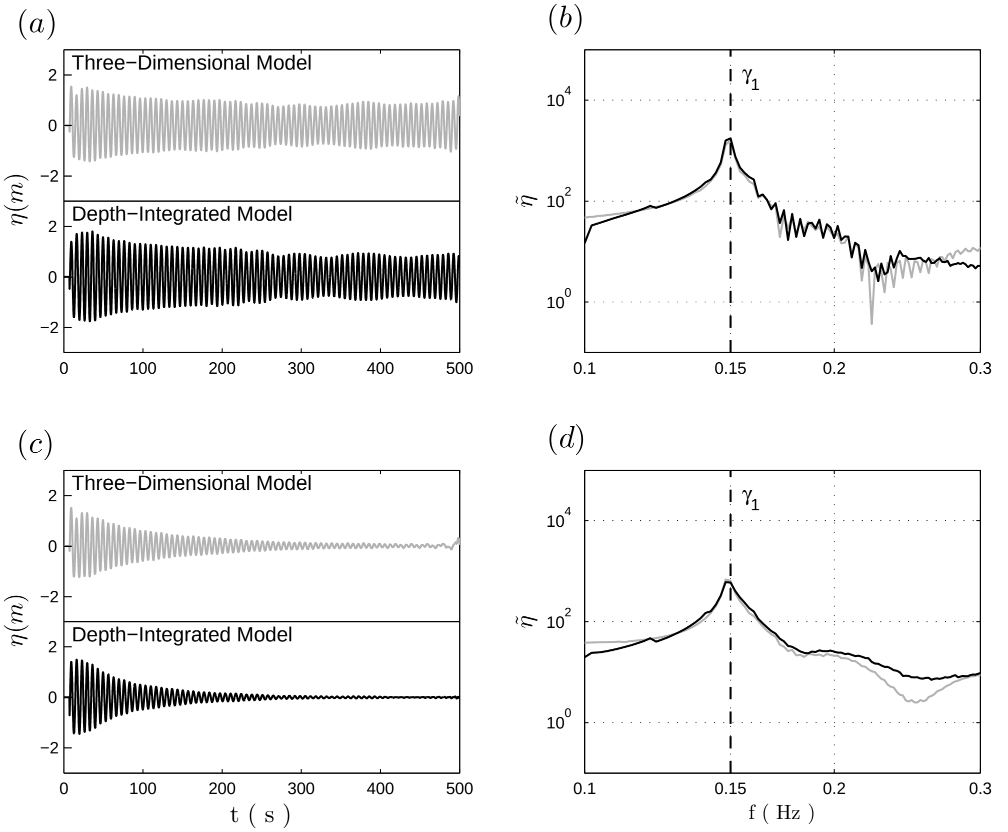

Figure 5.3: Results for the free surface elevation time series at 96 km from tsunamigenic source from 3D (light gray) and depth integrated (black) models in a constant depth, $h_p = 2200m$, $a = 1000m$, $c = 1500m/s$, $c_s = 2000m/s$, $\rho = 1000kg/m^3$, $\rho_s = 1850kg/m^3$, for a unit source area with semi-length $b = 112km$ and rising time $\tau = 1\ s$. (a, b) Time series and corresponding spectra of free surface elevation where $\mu_s = 0$ and (c, d) $\mu_s = 2 \times 10^8 Pas$ with $\gamma_1 = \omega_1/2\pi = 0.15Hz$.

of the earthquake ($x = 0$), computations are undertaken only for half of the physical domain. The Sommerfeld radiation condition is applied at the open end of the domain, so that the waves leave the domain freely. At x=0, a fully reflective boundary condition is used in order to preserve symmetry. To correctly reproduce the wave field, the maximum mesh size is 200 m, for a total of 1000 elements in the case of the depth-integrated model (5.23), and more than 30000 elements for the 3D one (5.6 and 5.7). The time step is $t = 0.1$ s and the computational time to reproduce 500 s of real-time simulation was about 10 minutes for (5.23) and about 3 hours for (5.6 and 5.7); a computer equipped with an i7 3.2 GHz CPU and 64GB RAM has been used. The simplified earthquake effect is modeled as a displacement in the vertical direction of the bottom with duration $\tau = 1\ s$ and bottom velocity defined by Eq. (5.3); The results are presented in the Fig. 5.3 in terms of free surface elevation η and corresponding spectrum $\tilde{\eta}$. Results are shown for a virtual surface gauge at x=96 km over a 112 km semifault where water depth and sediment thickness are $h_p = 2200$ and $a = 1000m$ respectively. In panel (a, b) the results are related to the case of inviscid sediment. The 3D model (light gray) and depth integrated model (black) are in optimal agreement. The peak frequency is at $\gamma = 0.15Hz$, corresponding to the first cut off frequency for the coupled system defined by Eq (5.2). The hydro-acoustic waves remain at the same order of the generated ones until the end of computations. In lower panels (c, d), we add the dissipation term into the equation ($\mu_s = 2 \times 10^8 Pas$). The generated hydro-acoustic waves are attenuated gradually during 500 s.

In the second case, a varying sea water depth overlying a varying sedimentary layer is considered; the domain's geometry, depicted in the upper plot of Fig. 5.4, has a 220 km long region with a 2 km depth in each layer, a region 50 km long with a sloping bottom, and another region 230 km long with constant water depth of 3.5 km and sediment thickness of 0.5 km. In whole 500 km long domain, the total depth $h_s = 4km$. Ground motion occurs in a patch 15 km long at the left edge of the shallow area, shown in Panel (a) of Fig. 5.4; it moves vertically with a bottom velocity and total displacement of 1 m given by (5.3). The maximum mesh size is again 200 m, for a total of 2500 elements in the case of the depth-integrated model (5.23), and 130000 triangular elements for the 3D one (5.6 and 5.7). The time step and the discretization of the spectra are the same of the constant depth case. The computational time to reproduce 1000 s of real-time simulation was about 20 minutes for (5.23) and about 5 hours for (5.6 and 5.7), using the same

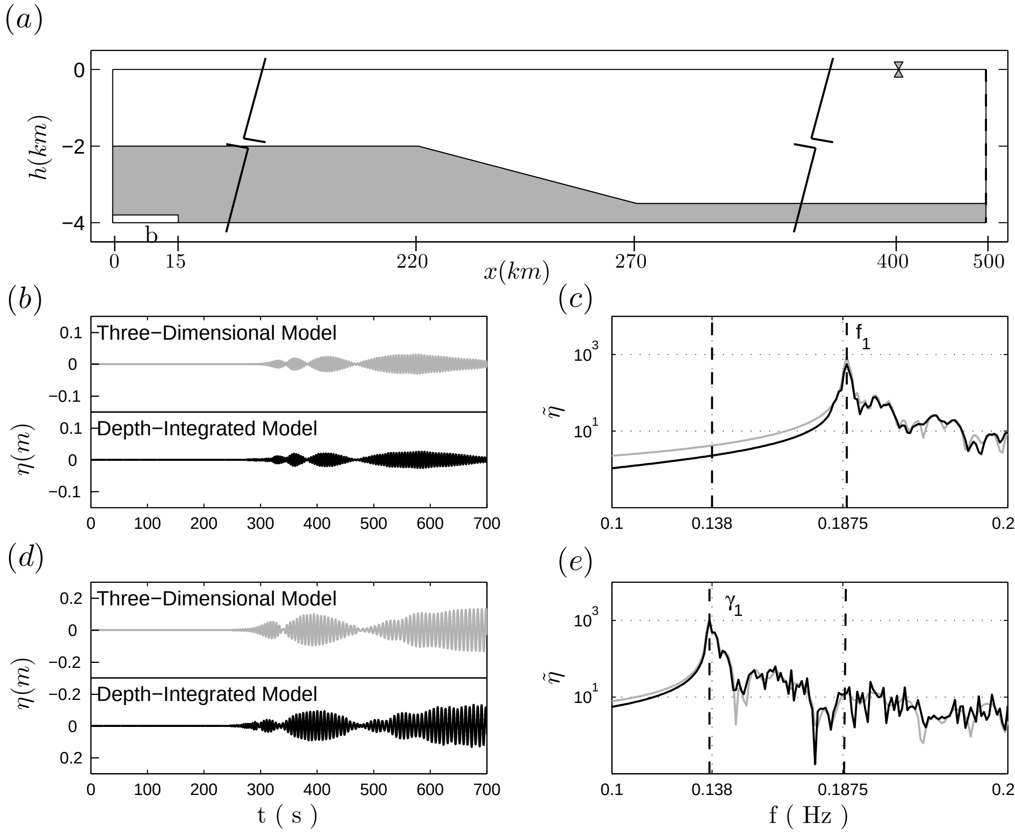

Figure 5.4: The case of varying sea bottom and sediment thickness with tsunamigenic source at shallower part. (a) The computational domain. Results for the free surface elevation time series at 400 km from tsunamigenic source from 3D (light gray) and depth integrated models (black), $c = 1500m/s$, $c_s = 2000m/s$, $\rho = 1000kg/m^3$, $\rho_s = 1850kg/m^3$ and $\mu_s = 0$ for a unit source area with semi-length $b = 15km$ and rising time $\tau = 1\ s$. (b, c) Results for impermeable sea bottom and (d, e) for coupled model.

computer of the previous simulation. The results are presented in Fig. 5.4 in terms of time series of free surface elevation η and corresponding spectra $\tilde{\eta}$, at a distance x=400 km from the moving sea bed area. The two time series are in good agreement, both in terms of amplitude and modulation of the signal. The comparison results show that the peak frequency shifts from $f_1 = 0.1875 Hz$ for impermeable bottom to $\gamma_1 = 0.138$ for coupled water and sediment model.

In the third case, model performance has been investigated for the case of earthquake on the deeper part of continental shelf in order to reveal the transmission and reflection properties of hydro-acoustic wave field in deep and shallow waters. The domain is depicted in panel (a) of Fig. 5.5 where earthquake occurs in the deeper area (3.5 km water depth over 0.5 km sediment) with the same physical characteristics of water and sediment and tsunamigenic source as previous cases. The results are presented in Fig. 5.5 in terms of time series of free surface elevation η and corresponding spectra $\tilde{\eta}$ at point A, 100 km from epicenter at 3.5 km water depth (black) and point B, 400 km from tsunamigenic source at 2 km water depth (light gray) obtained from depth integrated models for impermeable, (b, c) and permeable (d, e) sea-bottom. It can be seen from model results that the hydro-acoustic waves cannot propagate upslope. Lower hydro-acoustic wave frequencies than corresponding cut off frequency of observatory depth has been filtered. As a results, wave amplitudes decreased from point A to B. The reflected waves from slope superimposed to arriving wave trains and changed the wave pack modulation. This result point out the importance of deep sea observatories for hydro-acoustic wave detection as ponted out in Chapter 3.

5.4 Conclusions

The correct detection of hydro-acoustics waves in a real ocean consisting of a variable-depth water column overlying a sediment layer could enhance significantly the efficiency and promptness of Tsunamis Early Warning Systems (TEWS). In this regard, a numerical model able to reproduce the main features of hydro-acoustic waves generated by sudden displacement of the ocean bottom is necessary. We have therefore considered a weakly compressible inviscid fluid coupled with a compressible viscous sedimentary layer in which waves are generated by a moving bottom and then propagate

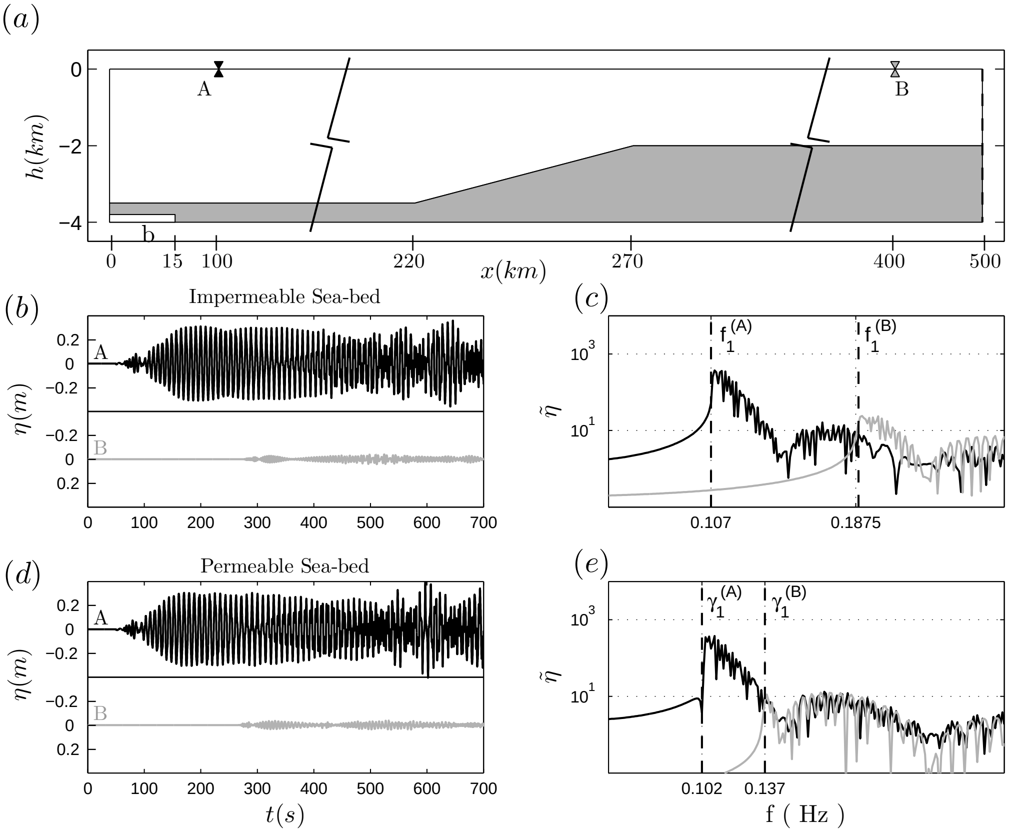

Figure 5.5: The case of varying sea bottom and sediment thickness with tsunamigenic source at deeper part. (a) The computational domain. Results for the free surface elevation time series at point A, 100 km from tsunamigenic source at 3.5 km water depth (black) and point B, 400 km from tsunamigenic source at 2 km water depth (light gray) obtained from depth integrated models. The water and sediment characteristics are the same as Fig. 5.4. (b, c) results for impermeable sea bottom and (d, e) for coupled model.

over a mildly sloped sea bed. Via a proper application of the averaging technique, we have derived the hyperbolic Mild Slope Equation for Dispersive Weakly Compressible fluids, MSEDWC. Solution of the equation allows the description of all the mechanics in the x, y plane, overcoming at the same time both analytical and numerical difficulties. Indeed on the one hand, by expanding in series of the vertical eigenfunctions, the MSEDWC can be applied to more complex geometries other than the horizontal or piecewise horizontal in the x, z vertical plane as in the seminal work of *Chierici et al.* (2010) and *Eyov et al.* (2013). On the other hand, because computational time is one order of magnitude smaller than for a fully numerical 3D model, systematic applications supporting a TEWS in regions of geophysical interest will be viable.

Chapter 6

Stratified Sedimentary Layer role on Formation and Dissipation of Hydro-acoustic Waves

In this chapter, we investigate the role of a viscous compressible sedimentary layer underlying sea water on the formation, propagation and attenuation of hydro-acoustic waves. The analysis of low frequency pressure waves can be used for evaluation of stratified sediment structure. Section 6.1 describes the model equations and explains dominant frequency spectrum for different number of sedimentary layers. Damping behaviour is investigated in Section 6.2. Conclusions are given in Section 6.3.

6.1 hydro-acoustic wave model for multi-layer system

Consider the interaction of a train of hydro-acoustic waves in an inviscid water layer of depth $h(x, y, t)$ with the sound celerity of c and water density ρ overlying stratified viscous sediment layers of thickness $a^{(i)}(x, y, t)$, with $h_s^{(i)} = h + \sum\limits_{n=1}^{i} a^{(n)}$ where $h_s^{(i)}(x, y, t)$ is the total depth. $c_s^{(i)}$ is celerity of sound within sediment with density of $\rho_s^{(i)}$ and apparent sediment kinematic

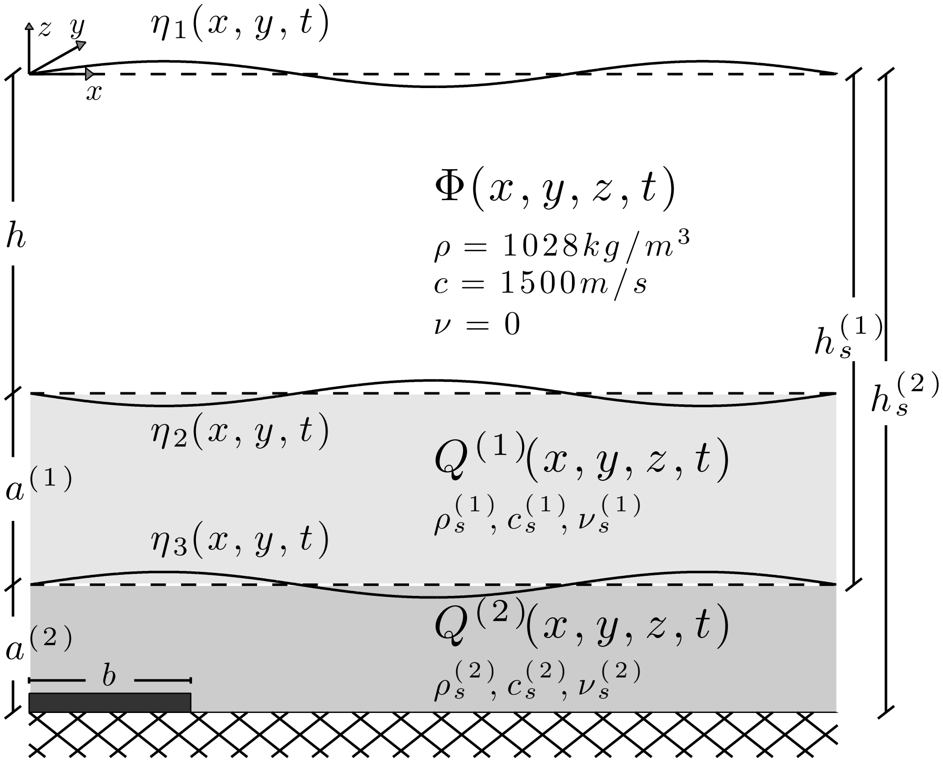
z
y
x
$\eta_1(x,y,t)$
$\Phi(x,y,z,t)$
$\rho = 1028kg/m^3$
$c = 1500m/s$
$\nu = 0$
h
$h_s^{(1)}$
$h_s^{(2)}$
$\eta_2(x,y,t)$
$Q^{(1)}(x,y,z,t)$
$a^{(1)}$
$\rho_s^{(1)}, c_s^{(1)}, \nu_s^{(1)}$
$\eta_3(x,y,t)$
$Q^{(2)}(x,y,z,t)$
$a^{(2)}$
b
$\rho_s^{(2)}, c_s^{(2)}, \nu_s^{(2)}$

Figure 6.1: Schematic view of fluid domain.

viscosity of $\nu_s^{(i)}$. g is the gravitational acceleration. The vertical coordinate, z, is measured positively upwards from the undisturbed free surface at $z = 0$, and x and y denote horizontal Cartesian coordinates as shown in Fig. 6.1. The other parameters are for sudden displacement of source area with semi-length b and rise time τ. The transient sea bed velocity, ζ_t, with a residual displacement ζ_0, is a trigonometric function expressed by

$$\zeta_{s,t}^{(i)} = \frac{\zeta_0}{2}[1 - \cos(\frac{2\pi(t-t_0)}{\tau})][H(t-t_0) - H(t-t_0-\tau)], \tag{6.1}$$

where $H(t)$ is the Heaviside step function. The time series of bottom displacement and velocity are shown in Fig. 6.2. For the case of two sedimentary layers, the linearized weakly compressible wave equations governing the fluid potential $\Phi(x,y,z,t)$ in the water layer and $\mathcal{Q}^{(i)}(x,y,z,t)$

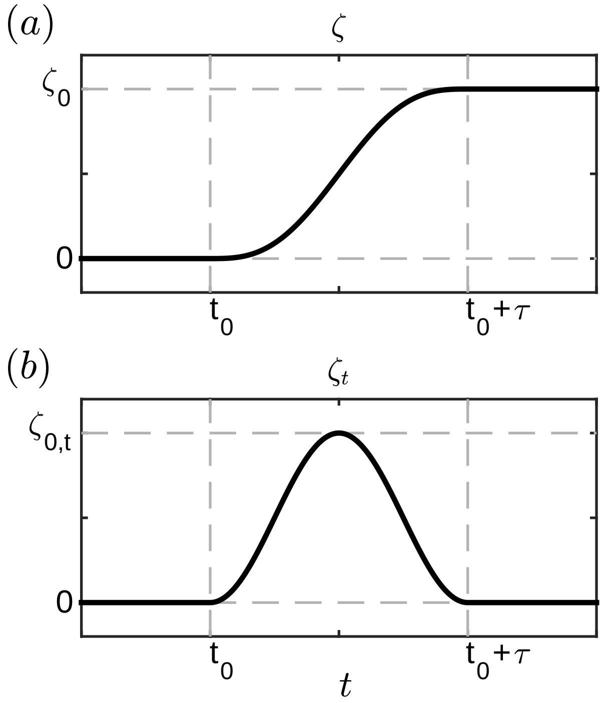

Figure 6.2: Rising mechanism starting at $t = t_0$ for period of τ with residual displacement of ζ_0. (a) Bottom displacement time series. (b) bottom velocity time series.

in the stratified viscous sediment layers, are given by

$$\begin{aligned}
&\Phi_{tt} - c^2\nabla^2\Phi = 0; && -h+\eta_2 \leq z \leq \eta_1 \\
&\mathcal{Q}^{(1)}_{tt} - {c^{(1)}_s}^2\nabla^2\mathcal{Q}^{(1)} - 2\nu^{(1)}_s(\nabla^2\mathcal{Q}^{(1)}_t) = 0; && -h^{(1)}_s+\eta_3 \leq z \leq -h+\eta_2 \\
&\mathcal{Q}^{(2)}_{tt} - {c^{(2)}_s}^2\nabla^2\mathcal{Q}^{(2)} - 2\nu^{(2)}_s(\nabla^2\mathcal{Q}^{(2)}_t) = 0; && -h^{(2)}_s \leq z \leq -h^{(1)}_s+\eta_3
\end{aligned} \tag{6.2}$$

where ∇^2 is the Laplacian in 3D and subscripts on dependent variables denote partial derivatives. The interfacial displacements $\eta_i(x, y, t)$; $i = 1, 2, 3$, represent response of the free surface and layers interface to hydro-acoustic disturbances. The apparent sediment kinematic viscosity is $\nu^{(i)}_s = \mu^{(i)}_s/\rho^{(i)}_s$. The bulk viscosity $\mu^{(i)}_s$ ranges from 10^6 up to 10^{20} Pa s (*Kimura*, 2006; *Van Keken et al.*, 1993). The boundary conditions at free surface and at the bottom for two sedimentary layers are given by

$$\begin{cases} \Phi_{tt} + g\Phi_z = 0 & \text{at} \quad z = 0 \\ \mathcal{Q}_z^{(2)} + \nabla_h h_s^{(2)} \cdot \nabla_h \mathcal{Q}^{(2)} + h_{s,t}^{(2)} = 0 & \text{at} \quad z = -h_s^{(2)} \end{cases} \tag{6.3}$$

where ∇_h is the horizontal gradient operator and $h_{s,t}^{(2)}$ is the vertical bottom velocity representing displacement of the impermeable substrate. Matching conditions at the water-sediment $z = -h + \eta_2$ and sediment-sediment interfaces $z = -h_s^{(1)} + \eta_3$ consist of continuity of pressure and kinematic constraints for each layer. After linearizing with respect to the pressure perturbation and small interface displacement, the resulting conditions are

$$\begin{cases} (R^{(1)} - 1)g\eta_2 = \Phi_t - R^{(1)}\mathcal{Q}_t^{(1)} \\ W_w = W_s^{(1)} = (-h + \eta_2)_t \end{cases} \text{at } z = -h \tag{6.4}$$

and

$$\begin{cases} (R^{(2)} - 1)g\eta_3 = \mathcal{Q}_t^{(1)} - R^{(2)}\mathcal{Q}_t^{(2)} \\ W_s^{(1)} = W_s^{(2)} = (-h_s^{(1)} + \eta_3)_t \end{cases} \text{at } z = -h_s^{(1)} \tag{6.5}$$

where $R^{(1)} = \rho_s^{(1)}/\rho$ and $R^{(2)} = \rho_s^{(2)}/\rho_s^{(1)}$. The normal velocities at the interface inside the water column, W_w, and sedimentary layers, $W_s^{(i)}$, are given by:

$$\begin{cases} W_w = \Phi_z + \nabla_h h \cdot \nabla_h \Phi \\ W_s^{(1)} = \mathcal{Q}_z^{(1)} + \nabla_h h \cdot \nabla_h \mathcal{Q}^{(1)} \end{cases} \text{at } z = -h \tag{6.6}$$

and

$$\begin{cases} W_s^{(1)} = \mathcal{Q}_z^{(1)} + \nabla_h h_s^{(1)} \cdot \nabla_h \mathcal{Q}^{(1)} \\ W_s^{(2)} = \mathcal{Q}_z^{(2)} + \nabla_h h_s^{(1)} \cdot \nabla_h \mathcal{Q}^{(2)} \end{cases} \text{at } z = -h_s^{(1)} \tag{6.7}$$

In the absence of viscous behaviour of sea bottom, the dominant frequency range in the wave spectrum can be expressed by a discrete set of normal frequencies $f^{(n)}$ given by

$$f^{(n)} = (2n - 1)\frac{c}{4h}, \qquad n = 1, 2, 3, \cdots \tag{6.8}$$

Introducing a single underlying sediment layer ($i = 1$) acting together with water column, it lowers the spectral peak frequencies, which are determined from the following transcendent equation (*Nosov et al.*, 2007):

$$\tan\left[\frac{2\pi\gamma_1^{(n)}h}{c}\right]\tan\left[\frac{2\pi\gamma_1^{(n)}a^{(1)}}{c_s^{(1)}}\right] = \frac{\rho_s^{(1)}c_s^{(1)}}{\rho c} \tag{6.9}$$

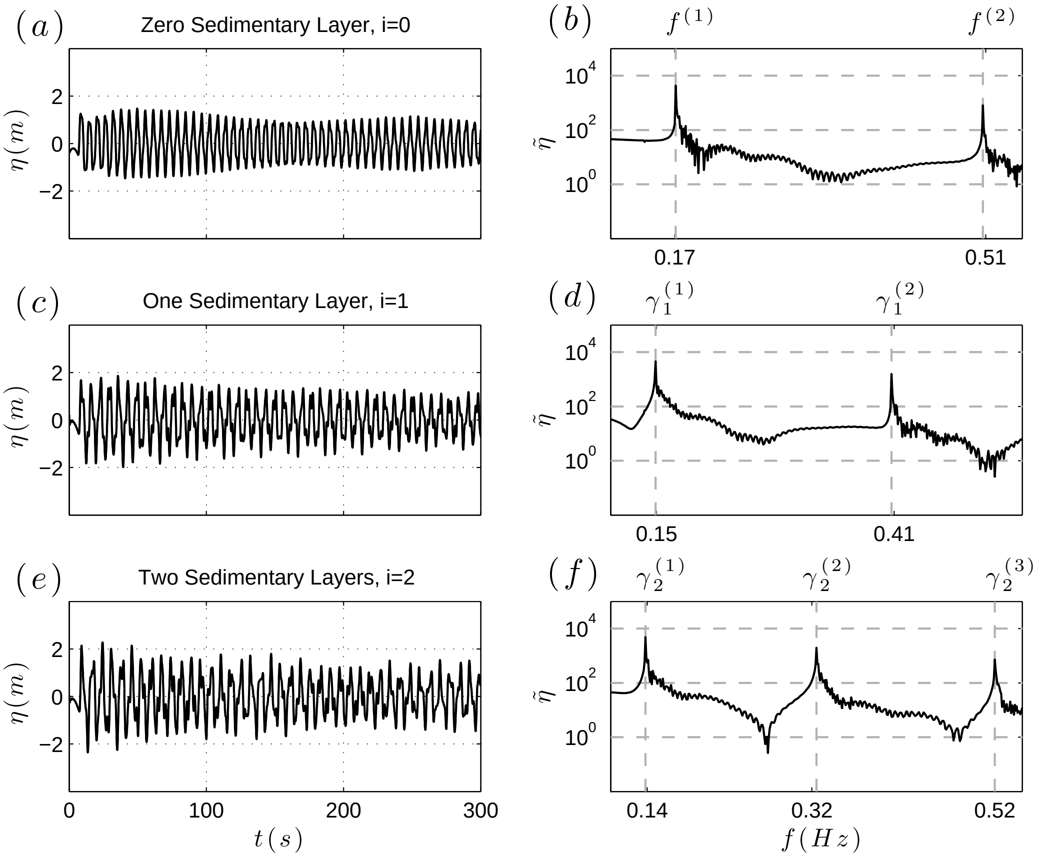

Figure 6.3: Results for the free surface elevation time series (left column) and their relative frequency spectra (right column) at a distance of $x = 96$ km from epicenter, results of a sample computation carried out using a 3D flow solver with computation parameters reported in Tab. 6.1. Panels show the case of (a, b) no sedimentary layer, $i = 0$, compressible water model with rigid bottom; (c, d) a coupled model of compressible water and a viscous compressible sediment, $i = 1$, $\mu_s^{(1)} = 0$; (e, f) a coupled model of compressible water and two viscous compressible sedimentary layers, $i = 2$, $\mu_s^{(1,2)} = 0$. The vertical dashed lines at the right column of panels represent the peak frequencies $f^{(n)}$ calculated by Eq. (6.8) at panel (b), $\gamma_1^{(n)}$ calculated by Eq. (6.9) at panel (d) and $\gamma_2^{(n)}$ calculated by Eq. (6.10) at panel (f).

Table 6.1: Sample computation parameters

Layer	Density (kg/m^3)	Sound Celerity (m/s)	Thickness (m)
Water	$\rho = 1028$	$c = 1500$	$h = 2200$
Sed.($i = 1$)	$\rho_s^{(1)} = 1850$	$c_s^{(1)} = 2000$	$a^{(1)} = 1000$
Sed. ($i = 2$)	$\rho_s^{(2)} = 2200$	$c_s^{(2)} = 2500$	$a^{(2)} = 1000$

Duration (s)	Start Time (s)	Fault Length (km)	Res. Disp. (m)
$b = 112$	$t_0 = 5$	$\tau = 2$	$\zeta_0 = 1$

Table 6.2: Spectral peak frequencies for $i = 0, 1, 2$ sedimentary layer(s) given by Eqs. 6.8, 6.9 and 6.10, relative to the first three hydro-acoustic modes

Sediment Layer(s)	1^{st} mode (Hz)	2^{nd} mode (Hz)	3^{rd} mode (Hz)
0 Layer	$f^{(1)} = 0.17$	$f^{(2)} = 0.51$	$f^{(3)} = 0.85$
1 Layers	$\gamma_1^{(1)} = 0.15$	$\gamma_1^{(2)} = 0.41$	$\gamma_1^{(3)} = 0.60$
2 Layers	$\gamma_2^{(1)} = 0.14$	$\gamma_2^{(2)} = 0.32$	$\gamma_2^{(3)} = 0.52$

where $\gamma_1^{(n)}$ denotes the normal mode frequencies for the coupled case. Note that in the case of $a^{(1)} = 0$, the set of normal modes described by Eqs. (6.8) and (6.9) coincide. Adding a second sedimentary layer ($i = 2$), natural frequencies, $\gamma_2^{(n)}$ toward lower values further shifts according to

$$\frac{\frac{\rho_s^{(2)}c_s^{(2)}}{\rho_s^{(1)}c_s^{(1)}} - \tan[\frac{2\pi\gamma_2^{(n)}a^{(1)}}{c_s^{(1)}}]\tan[\frac{2\pi\gamma_2^{(n)}a^{(2)}}{c_s^{(2)}}]}{\tan[\frac{2\pi\gamma_2^{(n)}a^{(2)}}{c_s^{(2)}}] + \frac{\rho_s^{(2)}c_s^{(2)}}{\rho_s^{(1)}c_s^{(1)}}\tan[\frac{2\pi\gamma_2^{(n)}a^{(1)}}{c_s^{(1)}}]} = \frac{\rho c}{\rho_s^{(1)}c_s^{(1)}}\tan[\frac{2\pi\gamma_2^{(n)}h}{c}] \tag{6.10}$$

Note that in the case of $a^{(2)} = 0$, the set of normal modes described by Eqs. (6.9) and (6.10) coincide.

Observation during *Tokachi-Oki* 2003 event shows that the dominant peak frequencies are lower than values estimated by Eq. (6.8), for one single water column with rigid bottom assumption (*Nosov et al.*, 2007). This suggests to investigate the role of sedimentary layers in formation of standing waves, developed vertically between the sea bottom and the water surface.

A sample computation is carried out using a full 3D solver for three computational domains (rigid bottom/one sedimentary layer ($i = 1$)/two sedimentary layers coupled with water column, $i = 2$). The model parameters

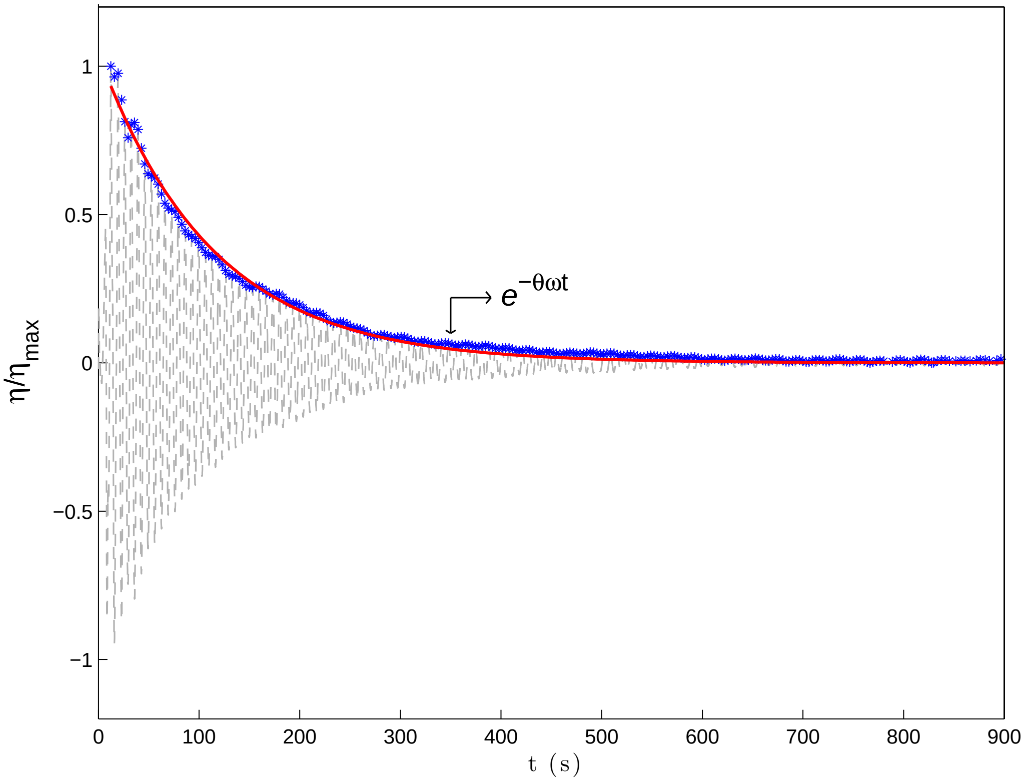

Figure 6.4: Time series of free surface elevation normalized by the maximum value (η/η_{max}) for the case of $h = 2200\ m$ water column overlying a single sedimentary layer ($a^{(1)} = 1000\ m$). The other parameters are $c = 1500\ m/s$, $c_s^{(1)} = 2000\ m/s$, $\rho = 1028\ kg/m^3$, $\rho_s^{(1)} = 1850\ kg/m^3$ and $\mu_s^{(1)} = 2 \times 10^8$ for a unit source area with semi-length $b = 112\ km$ and rising time $\tau = 2\ s$. Blue dots represent temporal variation of the peak amplitudes. Red line is the fitting curve representing an exponential function ($e^{-\theta\omega t}$).

are shown in Tab. 6.1. The results are depicted in Fig. 6.3, which shows the free surface elevation time series η (left column) and the corresponding frequency spectrum $\tilde{\eta}$ (right column) at 96 km from the epicenter. In panels (a, b) one layer of compressible water model with impermeable sea bottom is considered. The numerical spectrum and analytical calculation for natural modes expressed by Eq. (6.8) are essentially identical. In panels (c, d) and for the case of a sedimentary layer underlying the water column, the dominant frequencies match the roots of Eq. (6.9). In panels (e, f) where two sedimentary layers are coupled with water layer, the natural modes are in good agreement with values estimated by Eq. (6.10). The first three peak frequencies for different models are presented in Tab. 6.2. The comparison shows that in order to properly model the shifts in peak frequencies, it is essential to consider the underlying layers. In the following section, the effective sediment thickness is explored.

6.2 Damping Behaviour

In the framework of hydro-acoustic wave theory, the underlying sedimentary layer can be treated as introduced in Section 6.1, as a "Fluid-Like" medium coupled with water column at the interface (*Chierici et al.*, 2010; *Abdolali et al.*, 2015b). In this regard, sediment intergranular friction governs the sound propagation field leading to change in natural frequencies and evanescence of hydro-acoustic waves. A nondimensionalization of the sediment layer equation yields a parameter $\epsilon = \omega \nu_s / c_s^2$ characterizing the size of the damping term relative to the undamped wave equation. A series of computations have been carried out to reveal to what extent the damping term ϵ can affect the damping rate and dominant peak frequencies. The water depth, sediment thickness, densities and sound speeds within water and sediment and source parameters are the same as Figure 6.3 with different bulk viscosities ($10^6 < \mu_s^{(1)} < 10^{20}$ Pas). As an example, the results of one simulation for $\mu_s^{(1)} = 2 \times 10^8 Pas$ in term of free surface elevation at $x = 96$ km from source is shown in Fig. 6.4. The time series is normalized by the maximum free surface elevation. As is shown in the plot, hydro-acoustic wave amplitude decreases gradually. An exponential fitting curve (red line) is extrapolated among the blue dots representing peak amplitudes

$$\frac{\eta}{\eta_{max}} = e^{-\theta \omega t} \tag{6.11}$$

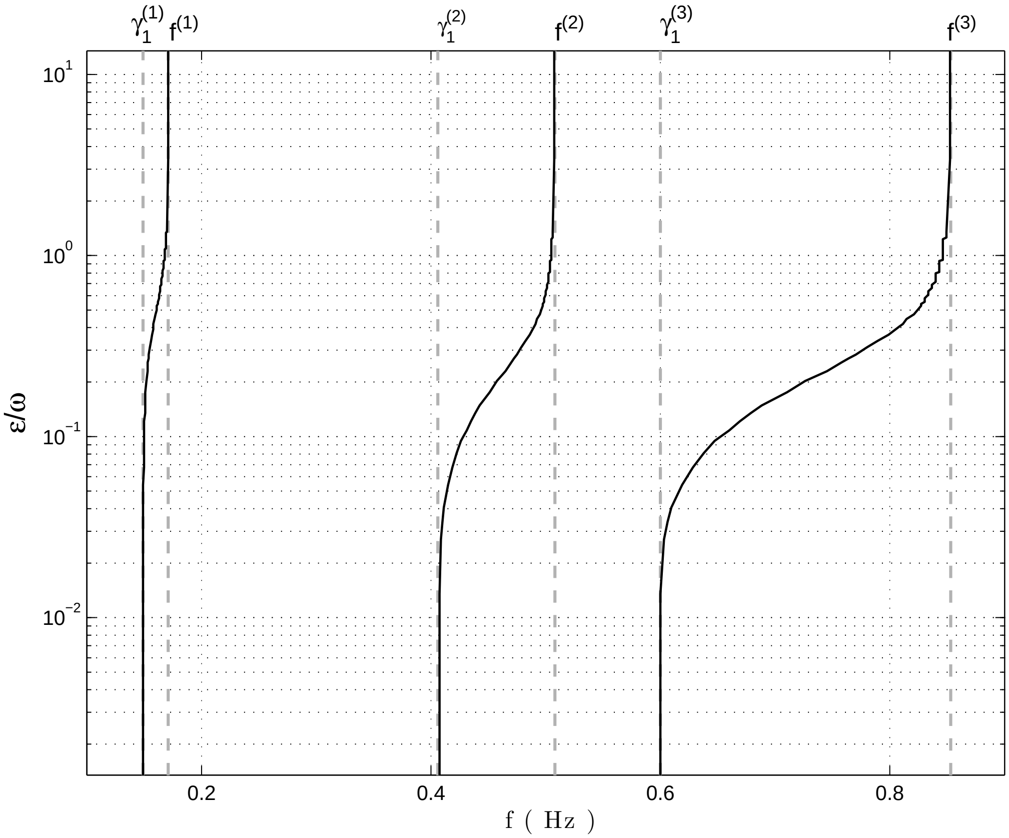

Figure 6.5: Variation of peak frequencies for different damping term (ϵ). The light gray dashed lines represent the natural modes for rigid bottom $f^{(n)}$ and two layered system $\gamma_1^{(n)}$ shown in Tab.6.2.

where θ is dimensionless damping rate. In Fig. 6.5, the variation of the first three peak frequencies is plotted for different damping terms ϵ. It can be seen from the plot that for small $\epsilon/\omega < 0.02$, the dominant frequencies are close to those estimated by Eq. (6.9) for inviscid sediment case. Then, the peak frequencies increase to reach those estimated from Eq. (6.8) for rigid bottom ($\epsilon/\omega > 2$). The damping rate variation is plotted in Fig. 6.6. Where the damping term is small ($\epsilon < 10^{-4}$), sediment acts like an inviscid fluid. In this condition, the coupled system consists of two fluids with different densities/sound speeds. As a result, the long lasting hydro-acoustic waves are not absorbed due to internal losses at grain-to-grain contacts. The damping rate increases while the damping term is rising from $\epsilon = 10^{-4}$ to 8×10^{-2}. Crossing the maximum damping rate θ, the permeability of underlying layer decreased gradually. It reaches $\epsilon > 10^2$ where model result is similar to one water column with rigid bottom. Overall, taking the damping term into account leads to temporal damping of hydro-acoustic waves. In addition, depending on the damping term magnitude, it can change the dominant peak frequencies. From a practical point of view, the analysis of measured time series during tsunamigenic events reveals the sedimentary layer characteristics and justify the mismatch between one layer/multi-layers assumptions. It can be used to optimize the number of sedimentary layers considered for numerical modeling of wave fields. The accurate thickness, density and sound speed within stratified sedimentary layers, taken from presented analysis, improve the accuracy of model results.

6.3 Conclusions

Considering the stratified sedimentary layers in numerical modeling of hydro-acoustic waves can improve the accuracy of model results. The permeable sea bottom causes hydro-acoustic wave attenuation and leads to a shift in dominant peak frequencies. However, due to existence of uncertainties about sediment structure in real ocean with variable-water/sediment depth, a careful analysis is needed to optimize the number of layers required to obtain reasonable results and choose appropriate density and sound speed of each layer. In this regard, a series of computations have been carried out to extract the range of effective sediment characteristics on hydro-acoustic wave field. It can be used in the analysis of measured time series during past tsunamigenic events and used in future modeling.

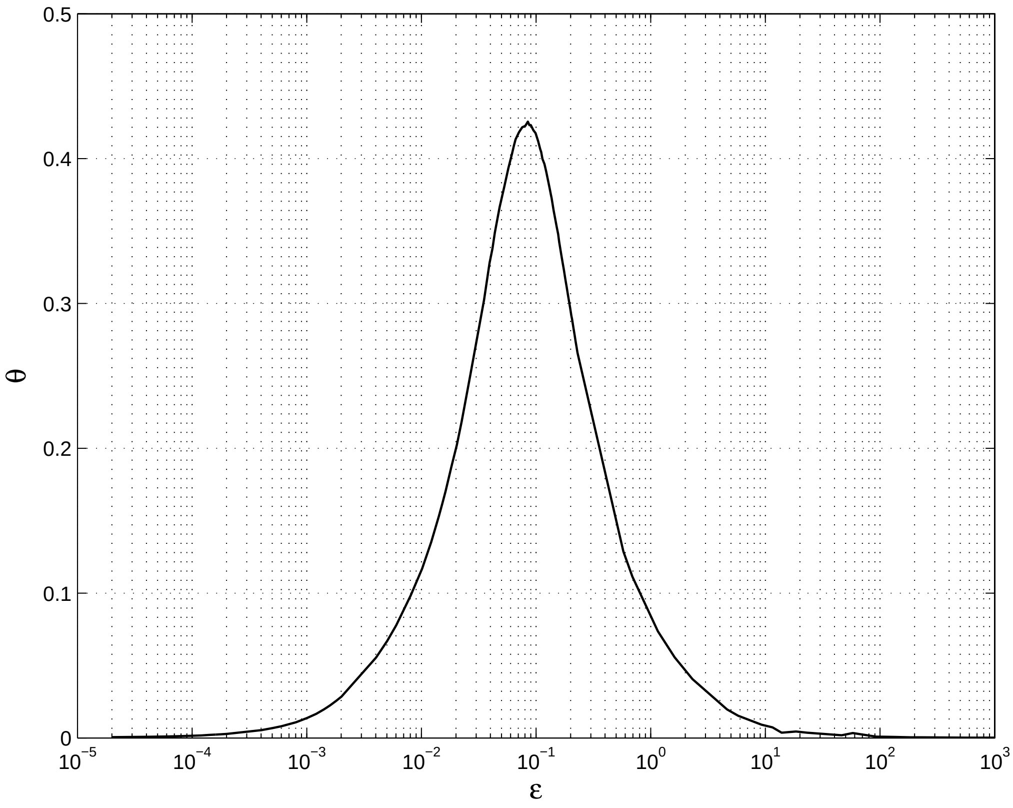

Figure 6.6: Variation of dimensionless damping rate θ as is shown in Fig. 6.4 for different damping terms ϵ.

Chapter 7

Summary

7.1 Conclusion Remarks

To show the need and value of an efficient numerical model for studying hydro-acoustic waves generated by tsunamigenic earthquakes for TEWS design, a detailed literature review of previous works was conducted revealing there exists a few number of studies for compressible sea.

Via a proper application of the averaging technique, two depth integrated equations, namely MSEWC and MSEDWC, are derived for rigid and permeable sea bottom assumptions respectively. The presented models allow the description of all the mechanics in the x, y plane for complex geometries overcoming difficulties of fully three dimensional numerical models which are unreasonably expensive and to avoid the limits of available analytical solutions.

The hyperbolic Mild Slope Equation for Weakly Compressible fluids, MSEWC, has been used to reconstruct the hydro-acoustic wave propagation generated by two main tsunamigenic destructive historical earthquakes occurred in the Mediterranean Sea: the 365 AD Crete event and the 1693 Sicily event. The model results proposed suggestions for deep sea observatory deployment to capture the precursor tsunami components appropriate for TEWS.

The same model has been used for a more recent 2012 Haida Gwaii event where there exists deep sea observations. Model results comparison with time series collected from deep sea pressure gauges and seismometers revealed the importance of underlying sedimentary layers on formation and attenuation of hydro-acoustic waves. The model performed well for long gravitational waves (tsunamis).

Considering the stratified sedimentary layers in numerical modeling of hydro-acoustic waves can improve the accuracy of model result. The permeable sea bottom causes hydro-acoustic wave attenuation and leads to a shift in dominant peak frequencies. Subsequently, the hyperbolic Mild Slope Equation for dissipative Weakly Compressible fluids, MSEDWC, has been derived to fulfill the requirements.

This study demonstrated the benefit of depth integrated model simulations of compressible sea as an aid in decision making for Tsunami Early Waring Systems (TEWS).

In addition, considering the water compressibility can improve our understanding of the physics of tsunami generation and propagation and reveal the correlation between observed signals and the source parameters. Moreover, it helps us to interpret collected data during tsunami events.

7.2 Future Outlook

The present research provided an initial glimpse into the possibilities of using hydro-acoustic waves detection for enhancement of available Tsunami Early Warning Systems. Furthermore it identified a range of obstacles that need improvement to make compressible fluid simulations more feasible, accurate, effective, and reliable. Improvements are necessary not only for the model system but also for the availability and quality of data to both develop and verify the models. Given that resources and man-power are available for future studies, the following improvements are suggested:

- Considering lower layer being a viscoelastic medium so that the interfacial waves correspond to Rayleigh waves. It would be interesting to see if we could reproduce the initial depression observed in long distance signals (like the Tohoku 2011 signals observed by the west coast and south American DART observatories) which are thought to be elastic ground deformation in front of the usual positive hydrodynamic surge.

- Derivation of a depth-integrated model which considers multiple sediment layers.

- Using the MSEDWC model for reconstruction of a recent event where the bottom pressure records and sediment structure are available (i.e. Tokachi Oki 2003, Haida Gwaii 2012 and Tohoku Oki 2011).
- Taking variation of sound speed in water column into account to see its role on acoustic signals and the convergence of acoustic waves in SOFAR channel.
- Investigating the hydro-acoustic waves generated by submarine landslides and examining the performance of presented depth integrated models for landslide generated acoustic signals.
- Taking the advantage of High Performance Computing (HPC) and parallel computing to resolve the problem with finer resolution leading to estimate higher frequencies.
- Improving the Spatiotemporal bottom motion assumptions for real case applications which have a deep influence on hydro-acoustic wave field.
- Analysis of collected time series of hydrophone mounted at the sea bottom and SOFAR channel during recent events.

Appendix A

Dispersion Relation for One Layer System

The propagation of small amplitude wave for compressible, irrotational fluid, in a constant depth sea bottom, is expressed by the following linear fluid velocity potential problem

$$\begin{cases} \phi_{tt} - c_s^2 \nabla^2 \phi = 0 \\ \phi_{tt} + g\phi_z = 0 \qquad at \quad z = 0 \\ \phi_z = 0 \qquad\qquad\quad at \qquad z = -h \end{cases} \tag{A.1}$$

The problem can be rewritten in the frequency domain as

$$\begin{cases} -\omega^2 \Phi - c_s^2 \nabla^2 \Phi = 0 \\ \omega^2 \Phi + g\Phi_z = 0 \qquad at \quad z = 0 \\ \Phi_z = 0 \qquad\qquad\quad at \qquad z = -h \end{cases} \tag{A.2}$$

which can be derived by applying the Fourier Transform of the fluid velocity potential

$$\Phi\left(x, z, \omega\right) = \int\limits_{-\infty}^{\infty} \phi\left(x, z, t\right) e^{-i\omega t} dt \tag{A.3}$$

or by assuming a time harmonic motion and therefore writing the fluid potential as

$$\Phi\left(x, z, \omega\right) = Real\left\{\varphi(x, z) e^{-i\omega t}\right\} \tag{A.4}$$

The problem can be solved by the separation of variables methods, which means seeking the solution in the form

$$\Phi\left(x, z; \omega\right) = \Psi\left(x; \omega\right) f\left(z; \omega\right) \tag{A.5}$$

The problem can be rewritten as

$$\begin{cases} \frac{\omega^2}{c_s^2} + \frac{\Psi_{xx}}{\Psi} + \frac{f_{zz}}{f} = 0 \\ -\omega^2 + g\frac{f_z}{f} = 0 \qquad at \quad z = 0 \\ \frac{f_z}{f} = 0 \qquad\qquad at \qquad z = -h \end{cases} \tag{A.6}$$

The second term of the first equation of problem (A.6) depends on x, while the third depends only on z; this equation is valid only if

$$\Psi_{xx} + \left(\frac{\omega^2}{c_s^2} + \beta^2\right)\Psi = 0 \tag{A.7}$$

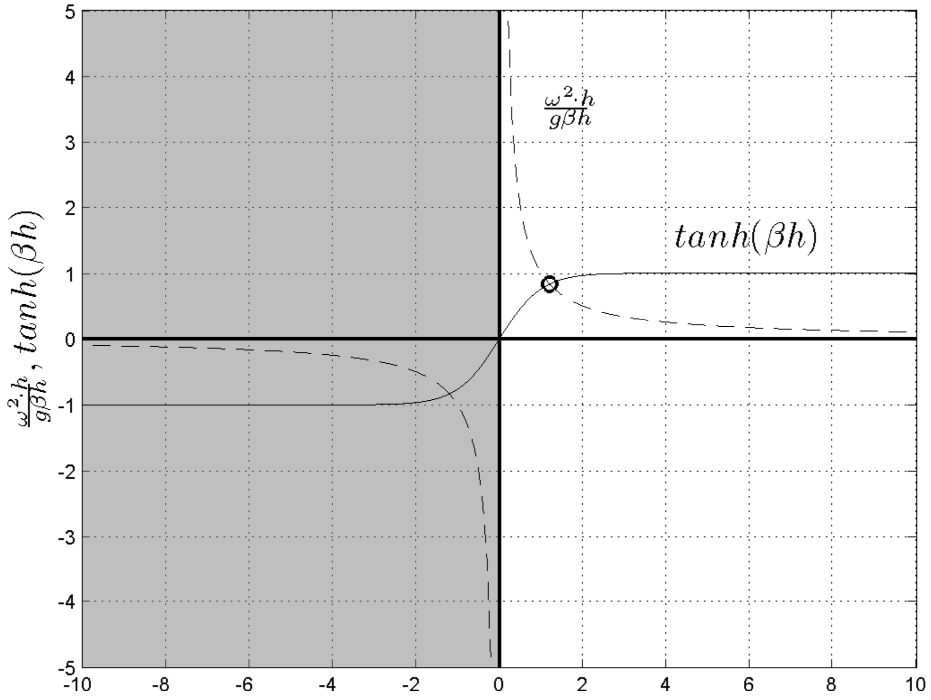

Figure A.1: Dispersion relation for β real greater that zero

$$f_{zz} - \beta^2 f = 0 \tag{A.8}$$

where β^2 is the separation constant. Now equations (A.7) and (A.8) are ordinary differential equations, and may be solved separately. Let consider two cases: the first where β is real and greater than zero; the second where β is imaginary. In the first case the general solution of (A.8) is:

$$f(z) = A\cosh(\beta z) + B\sinh(\beta z) \tag{A.9}$$

The coefficients A and B can be found using the boundary conditions of the problem (A.6). The bottom boundary condition states that the derivative of f at $z = -h$ is equal to zero, and therefore:

$$-A\beta\sinh\left(\beta h\right)+B\beta\cosh\left(\beta h\right)=0 \tag{A.10}$$

from which the relation between A and B can be found

$$B=A\tanh\left(\beta h\right) \tag{A.11}$$

From the free surface boundary condition it can be achieved that:

$$-\frac{\omega^2}{g}A+\beta B=0 \tag{A.12}$$

and therefore

$$\omega^2=g\beta\tanh\left(\beta h\right) \tag{A.13}$$

It can be proved that exist only one positive value of real β which satisfy the dispersion relation (A.13), see the Figure A.1. Let's call it β_0.

At this point the function $f\left(z\right)$ can be found as

$$\begin{aligned} &f\left(z\right)=A\cosh\left(\beta_0 z\right)+B\sinh\left(\beta_0 z\right)\\ &=A\cosh\left(\beta_0 z\right)+A\tanh\left(\beta_0 h\right)\sinh\left(\beta_0 z\right)\\ &=A\cosh\left(\beta_0 z\right)\cosh\left(\beta_0 h\right)+A\sinh\left(\beta_0 h\right)\sinh\left(\beta_0 z\right)\\ &=\tfrac{A}{\cosh\left(\beta_0 h\right)}\cosh\left(\beta_0\left(h+z\right)\right)\end{aligned} \tag{A.14}$$

Then consider equation (A.8) where $\beta=i\bar{\beta}$ is imaginary

$$f_{zz}+\bar{\beta}^2 f=0 \tag{A.15}$$

in this case the general solution is of the form:

$$f\left(z\right)=C\cos\left(\bar{\beta}z\right)+D\sin\left(\bar{\beta}z\right) \tag{A.16}$$

Again the coefficients C and D can be found using the boundary conditions of the problem (A.6). The bottom boundary condition states that:

$$C\beta\sin\left(\bar{\beta}h\right)+D\beta\cos\left(\bar{\beta}h\right)=0 \tag{A.17}$$

from which the relation between C and D can be found

$$D=-C\tan\left(\bar{\beta}h\right) \tag{A.18}$$

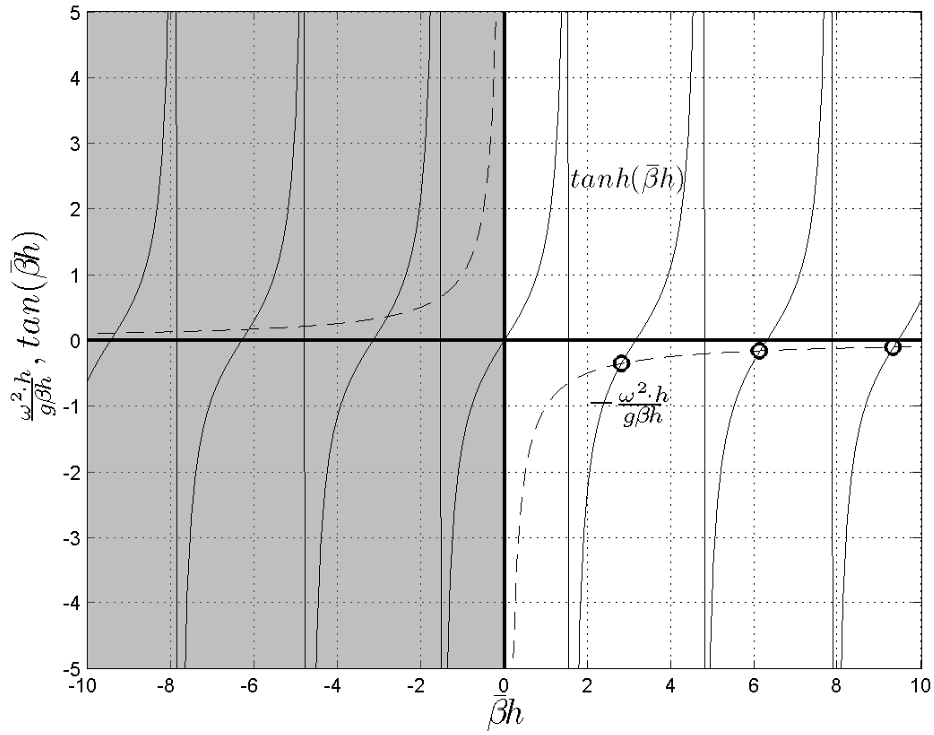

Figure A.2: Dispersion relation for β imaginary, $\beta = i\bar{\beta}$

From the free surface boundary condition it can be achieved that:

$$-\frac{\omega^2}{g}C + \bar{\beta}D = 0 \tag{A.19}$$

and therefore

$$\omega^2 = -g\bar{\beta}\tan\left(\bar{\beta}h\right) \tag{A.20}$$

The solution of the dispersion relation (A.20) now are infinite values of $\bar{\beta}$ and therefore of β, see figure A.2.

The function $f\left(z\right)$ depends on the $\bar{\beta}_n$, with $n = 1, 2, ...$ and can be found as

$$\begin{aligned}
&f_n\left(z\right) = C\cos\left(\bar{\beta}_n z\right) + D\sin\left(\bar{\beta}_n z\right) = \\
&= C\cos\left(\bar{\beta}_n z\right) + C\tan\left(\bar{\beta}_n h\right)\sin\left(\bar{\beta}_n z\right) = \\
&= C\cos\left(\bar{\beta}_n z\right)\cos\left(\bar{\beta}_n h\right) + C\sin\left(\bar{\beta}_n h\right)\sin\left(\bar{\beta}_n z\right) = \\
&= \tfrac{C}{\cos\left(\bar{\beta}_n h\right)}\cos\left(\bar{\beta}_n\left(h+z\right)\right)
\end{aligned} \tag{A.21}$$

In general we can say that the function $f\left(z\right)$ is given by the summation of different infinitive modes, $n = 0, 1, 2, ..., \infty$. The first one $n = 0$ correspond to real value of β all the other to imaginary values. It can be written in general:

$$\omega_n^2 = g\beta_n \tanh(\beta_n h) \tag{A.22}$$

$$f_n = \frac{\cosh\left[\beta_n\left(h+z\right)\right]}{\cosh}(\beta_n h) \tag{A.23}$$

both equations (A.22) and (A.23) for $n = 0$ and β_0 real turns out to be equal to equations A.13 and A.14, while for $n = 1, 2, ..., \infty$, $\beta_n = i\bar{\beta}_n$ the equations become

$$\omega_n^2 = -g\bar{\beta}_n \tan(\bar{\beta}_n h) \tag{A.24}$$

$$f_n = \frac{\cos\left[\bar{\beta}_n(h+z)\right]}{\cos(\bar{\beta}_n h)} \tag{A.25}$$

which correspond to equations A.20 and A.21 Now in order to find the solution in term of velocity potential, we have to solve the equation (A.7). Let's write it as:

$$\Psi_{xx} + k^2\Psi = 0 \tag{A.26}$$

where $k^2 = \frac{\omega^2}{c_s^2} + \beta^2$. The solution of equation (A.26) depends on the value of k, which we already know that are infinite, $k = k_n$ because $\beta = \beta_n$. For $n = 0$, β_0 is real and positive and therefore even k_0 is real and positive. For $n = 1, 2, ..., \infty$, β_n are imaginary and are equal to $i\bar{\beta}_n$, therefore k_n can be real and imaginary, depending on the β_n^2 values relative to the ratio ω^2/c_s^2

$$k_n^2 = \frac{\omega^2}{c_s^2} - \bar{\beta}_n^2 \begin{cases} > 0 & if \quad \bar{\beta}_n^2 < \frac{\omega^2}{c_s^2} \\ < 0 & if \quad \bar{\beta}_n^2 > \frac{\omega^2}{c_s^2} \end{cases} \tag{A.27}$$

The solution of Ψ has the form of:

$$\begin{cases} \Psi_0 = e^{\pm ik_0x} \quad for \quad n = 0 \\ \Psi_n = e^{\pm i|k_n|x} \quad for \quad n = 1, 2, ..., N \\ \Psi_n = e^{\pm |k_n|x} \quad for \quad n = N+1, N+2, ... \end{cases} \tag{A.28}$$

which leads to propagating modes for $n = 0, 1, 2, ..N$ and to evanescent modes for $n = N + 1, ...$

The fluid velocity potential can therefore be obtained as

$$\Phi = \sum_{n=0}^{\infty} \Psi_n f_n \tag{A.29}$$

and in the time domain can be obtained by applying the inverse Fourier Transform of eq. (A.29)

Appendix B

Dispersion Relation for Two Layers System

The linearized weakly compressible wave equation governing the fluid potential $\Phi(x,y,z,t)$ in the water layer and $\mathcal{Q}(x,y,z,t)$ in the viscous sediment layer with apparent sediment kinematic viscosity ν_s are given by

$$\begin{cases} \Phi_{tt} - c^2\nabla^2\Phi = 0; \quad -h + \eta_2(x,y,t) \le z \le \eta_1(x,y,t) \\ \mathcal{Q}_{tt} - c_s^2\nabla^2\mathcal{Q} - 2\nu_s(\nabla^2\mathcal{Q})_t = 0; \quad -h_s \le z \le -h + \eta_2(x,y,t) \end{cases} \tag{B.1}$$

where ∇^2 is the Laplacian in 3D and subscripts on dependent variables denote partial derivatives. The interfacial displacements η_1 and η_2 represent response of the free surface and layer interface to hydroacoustic disturbances. The boundary conditions at free surface and bottom are given by

$$\begin{cases} g\eta_1 + \Phi_t = 0 \\ \eta_{1t} - \Phi_z = 0 \end{cases} \text{at } z = 0 \tag{B.2}$$

Combination of kinematic and dynamic boundary conditions at free surface leads to:

$$\Phi_{tt} + g\Phi_z = 0 \quad \text{at} \quad z = 0 \tag{B.3}$$

Bottom boundary condition is given by

$$\mathcal{Q}_z + \nabla_h h_s \cdot \nabla_h \mathcal{Q} + h_{s,t} = 0 \quad \text{at} \quad z = -h_s \tag{B.4}$$

For flat bottom case

$$\mathcal{Q}_z = 0 \quad \text{at} \quad z = -h_s \tag{B.5}$$

where ∇_h is the horizontal gradient operator and $h_{s,t}$ is the vertical bottom velocity representing displacement of the impermeable substrate. Kinematic boundary condition at interface is given

$$\begin{cases} \eta_{2t} + \nabla_h\eta_2 \cdot \nabla_h\Phi = -\Phi_z \quad \text{at} \quad z = -h \\ \eta_{2t} + \nabla_h\eta_2 \cdot \nabla_h\mathcal{Q} = -\mathcal{Q}_z \quad \text{at} \quad z = -h \end{cases} \tag{B.6}$$

For flat bottom case

$$\eta_{2t} = -\Phi_z = -\mathcal{Q}_z \quad \text{at} \quad z = -h \tag{B.7}$$

Dynamic boundary condition at interface is given

$$\rho g\eta_2 + \rho\Phi_t = \rho_s g\eta_2 + \rho_s\mathcal{Q}_t \quad \text{at} \quad z = -h \tag{B.8}$$

The upper and lower layer potentials may be expanded according to

$$\Phi\left(x,y,z,t\right)=\sum_{n=0}^{\infty}\Phi_n\left(x,y,z,t\right)=\sum_{n=0}^{\infty}\psi_n\left(x,y,t\right)M_n\left(z\right)\tag{B.9}$$

for the water column and

$$\mathcal{Q}\left(x,y,z,t\right)=\sum_{n=0}^{\infty}\mathcal{Q}_n\left(x,y,z,t\right)=\sum_{n=0}^{\infty}\psi_{s,n}\left(x,y,t\right)N_n\left(z\right)\tag{B.10}$$

in the sediment layer.

Eq. B.7 can be rewriten as:

$$M'(-h)\psi=N'(-h)\psi_s\tag{B.11}$$

where ψ and ψ_s are arbitrary functions of (x,y,t). Since $M'(-h)$ and $N'(-h)$ are constants, these expressions are the same at all (x,y,t) only if $\psi=\psi_s$ everywhere. Thus, the (x,y,t) dependence for the two layers cannot be different. Look at the constant depth solutions

$$\begin{cases}\Phi=M(z)\psi(x,y,t)\\ \mathcal{Q}=N(z)\psi(x,y,t)\\ \eta_1=\hat{\eta}_1\psi(x,y,t)\\ \eta_2=\hat{\eta}_2\psi(x,y,t)\end{cases}\tag{B.12}$$

Govering equation for water column expressed in B.1 can be rewriten as

$$c^2(\frac{M''}{M})-c^2k^2+\omega^2=0\tag{B.13}$$

where $\psi_{tt}=-\omega^2\psi$ and ${\nabla_h}^2\psi=-k^2\psi$. Eq. B.13 can be rewriten:

$$M''-{\beta_w}^2M=0\tag{B.14}$$

where ${\beta_w}^2=k^2-\frac{\omega^2}{c^2}$. The solution is

$$M=A\cosh\beta_w(h+z)+A\sinh\beta_w(h+z)\tag{B.15}$$

Govering equation for sedimentary layer expressed in B.1 can be rewriten as

$$(1-2i\epsilon)\frac{N''}{N}-[k^2-\frac{\omega^2}{{c_s}^2}-2i\epsilon k^2]=0 \tag{B.16}$$

where $\epsilon = \omega\nu_s/{c_s}^2$ which is about 10^{-1} in our example. Therefore, we can define it as undamped sediment.

Eq. B.16 can be rewriten:

$$N''-{\beta_s}^2N=2i\epsilon(N''-k^2N)=0 \tag{B.17}$$

where ${\beta_s}^2=k^2-\frac{\omega^2}{c_s^2}$. The solution is

$$N=C\cosh\beta_s(h_s+z) \tag{B.18}$$

In principle, we could include the damping here as:

$$N''-\tilde{\beta_s}^2N=0 \tag{B.19}$$

where

$$\tilde{\beta_s}^2\simeq\frac{k^2(1-2i\epsilon)-\frac{\omega^2}{c_s^2}}{1-2i\epsilon}\simeq k^2-\frac{1}{1-2i\epsilon}\frac{\omega^2}{c_s^2} \tag{B.20}$$

For $\epsilon << 1$, $\tilde{\beta_s}^2\simeq\beta_s^2+2i\epsilon(\frac{\omega^2}{c_s^2})$.

The damped sedimentary layer assumption makes all the solution with complex terms. So, in order to make everything simpler, we have assumed the sedimentary layer undamped as defiend by Eq. B.
Using free surface boundary condition gives A in term of B.

$$gM'(0)-\omega^2M(0)=0 \tag{B.21}$$

Therefore

$$B=A\frac{\lambda-\mathrm{T}}{1-\lambda\mathrm{T}} \tag{B.22}$$

where $\lambda=\frac{\omega^2}{g\beta_w}$ and $\mathrm{T}=\tanh(\beta_wh)$. Thus, Eq. B becomes

$$M(z)=A[\cosh\beta_w(h+z)+\frac{\lambda-\mathrm{T}}{1-\lambda\mathrm{T}}\sinh\beta_w(h+z)] \tag{B.23}$$

Kinematic Match condition at the water-sediment interface

$$\Phi_z = \mathcal{Q}_z; \quad M' = N' \quad \text{at} \quad z = -h \tag{B.24}$$

Therefore

$$A\beta_w \frac{\lambda - \mathrm{T}}{1 - \lambda\mathrm{T}} = \beta_s C \sinh(\beta_s a) \tag{B.25}$$

where $a = h_s - h$ is sediment thickness. Dynamic Match condition at the water-sediment interface

$$g(1 - R)\hat{\eta}_2 = i\omega[A - RC\cosh(\beta_s a)] \tag{B.26}$$

where $R = \rho_s/\rho > 1$. We need to eliminate $\hat{\eta}_2$. Use

$$\hat{\eta}_{2,t} = \mathcal{Q}_z \quad \text{at} \quad z = -h \tag{B.27}$$

$\hat{\eta}_2$ can be expressed as

$$\hat{\eta}_2 = C\frac{i\beta_s}{\omega}\sinh(\beta_s a) \tag{B.28}$$

combining Eqs. B and B leads to

$$\lambda A = C\cosh(\beta_s a)[\lambda R + (1 - R)\alpha\tilde{\mathrm{T}}] \tag{B.29}$$

where $\alpha = \beta_s/\beta_w$ and $\tilde{\mathrm{T}} = \tanh(\beta_s a)$.

by using Eq. B in B to get final disperssion relation

$$\lambda^2(R + \alpha\mathrm{T}\tilde{\mathrm{T}}) - \lambda R(\mathrm{T} + \alpha\tilde{\mathrm{T}}) + (R - 1)\alpha\mathrm{T}\tilde{\mathrm{T}} = 0 \tag{B.30}$$

Proceed by forcing $M(0) = 1$, means $\Phi(x, y, 0, t) = \psi(x, y, t)$, leads to derive $M(z)$ and $N(z)$.

$$M(z) = \frac{(1 - \lambda\mathrm{T})\cosh(\beta_w(h + z)) + (\lambda - \mathrm{T})\sinh(\beta_w(h + z))}{(1 - \lambda\mathrm{T})\cosh(\beta_w h) + (\lambda - \mathrm{T})\sinh(\beta_w h)} \tag{B.31}$$

$$N(z) = \frac{(\lambda - \mathrm{T})\cosh\beta_s(h_s + z)}{\alpha\sinh(\beta_s a)[(1 - \lambda\mathrm{T})\cosh(\beta_w h) + (\lambda - \mathrm{T})\sinh(\beta_w h)]} \tag{B.32}$$

Bibliography

Abdolali, A., C. Cecioni, G. Bellotti, and P. Sammarco (2014), A depth-integrated equation for large scale modeling of tsunami in weakly compressible fluid, *Coastal Engineering Proceedings, ASCE, Seoul, Korea*, *1*(34).

Abdolali, A., C. Cecioni, G. Bellotti, and J. T. Kirby (2015a), Hydro-acoustic and tsunami waves generated by the 2012 haida gwaii earthquake: Modeling and in situ measurements, *Journal of Geophysical Research: Oceans*, *120*(2), 958–971, doi:10.1002/2014JC010385.

Abdolali, A., J. T. Kirby, and G. Bellotti (2015b), Depth-integrated equation for hydro-acoustic waves with bottom damping, *Journal of Fluid Mechanics*, *766*, doi:10.1017/jfm.2015.37.

Abdolali, A., C. Cecioni, J. T. Kirby, P. Sammarco, G. Bellotti, and L. Franco (2015c), Numerical modeling of low frequency hydro-acoustic waves generated by submarine tsunamigenic earthquake, in *Proceedings of the 25th International Ocean and Polar Engineering Conference ISOPE, Kona, Big Island, Hawaii, USA.*

Berkhoff, J. (1974), *Computation of combined refraction-diffraction*, Delft Hydraulics Laboratory.

Bolshakova, A., S. Inoue, S. Kolesov, H. Matsumoto, M. Nosov, and T. Ohmachi (2011), Hydroacoustic effects in the 2003 tokachi-oki tsunami source, *Russ. J. Earth Sci*, *12*.

Brekhovskikh, L., I. Lysanov, and Y. Lysanov (2003), *Fundamentals of Ocean Acoustics*, Springer.

Buckingham, M. J. (1997), Theory of acoustic attenuation, dispersion, and pulse propagation in unconsolidated granular materials including marine sediments, *Journal of the Acoustical Society of America*, *102*(5), 2579–2596.

Cassidy, J. F., G. C. Rogers, and R. D. Hyndman (2014), An overview of the 28 october 2012 mw 7.7 earthquake in haida gwaii, canada: A tsunamigenic thrust event along a predominantly strike-slip margin, *Pure and Applied Geophysics*, pp. 1–9.

Cecioni, C., and G. Bellotti (2010a), Modeling tsunamis generated by submerged landslides using depth integrated equations, *Applied Ocean Research*, *32*(3), 343–350.

Cecioni, C., and G. Bellotti (2010b), Inclusion of landslide tsunamis generation into a depth integrated wave model, *Natural Hazards and Earth System Science*, *10*(11), 2259–2268.

Cecioni, C., G. Bellotti, A. Romano, A. Abdolali, and P. Sammarco (2014), Tsunami early warning system based on real-time measurements of hydro-acoustic waves, *Procedia Engineering*, *70*(C), 311–320.

Cecioni, C., A. Abdolali, G. Bellotti, and P. Sammarco (2015), Large-scale numerical modeling of hydro-acoustic waves generated by tsunamigenic earthquakes, *Natural Hazards and Earth System Science*, *15*(3), 627–636, doi:10.5194/nhess-15-627-2015.

Chierici, F., L. Pignagnoli, and D. Embriaco (2010), Modeling of the hydroacoustic signal and tsunami wave generated by seafloor motion including a porous seabed, *Journal of Geophysical Research*, *115*(C03015), doi:10.1029/2009JC005522.

Ewing, M., I. Tolstoy, and F. Press (1950), Proposed use of the t phase in tsunami warning systems, *Bulletin of the Seismological Society of America*, *40*(1), 53–58.

Eyov, E., A. Klar, U. Kadri, and M. Stiassnie (2013), Progressive waves in a compressible-ocean with an elastic bottom, *Wave Motion*, *50*(5), 929 – 939, doi:http://dx.doi.org/10.1016/j.wavemoti.2013.03.003.

Hendin, G., and M. Stiassnie (2013), Tsunami and acoustic-gravity waves in water of constant depth, *Physics of Fluids (1994-present)*, *25*(8), 086,103.

Kadri, U., and M. Stiassnie (2012), Acoustic-gravity waves interacting with the shelf break, *Journal of Geophysical Research: Oceans (1978–2012)*, *117*(C3).

Kimura, M. (2006), Shear wave velocity in marine sediment, *Japanese journal of applied physics*, *45*(5S), 4824.

Kozdon, J. E., and E. M. Dunham (2014), Constraining shallow slip and tsunami excitation in megathrust ruptures using seismic and ocean acoustic waves recorded on ocean-bottom sensor networks, *Earth and Planetary Science Letters*, *396*, 56–65.

Landau, L., and E. Lifshitz (1987), Fluid mechanics, v. 6 of course of theoretical physics, 2nd english edition. revised.

Lay, T., L. Ye, H. Kanamori, Y. Yamazaki, K. F. Cheung, K. Kwong, and K. D. Koper (2013), The october 28, 2012 mw 7.8 haida gwaii underthrusting earthquake and tsunami: Slip partitioning along the queen charlotte fault transpressional plate boundary, *Earth and Planetary Science Letters*, *375*(0), 57 – 70, doi: http://dx.doi.org/10.1016/j.epsl.2013.05.005.

Maeda, T., and T. Furumura (2013), FDM simulation of seismic waves, ocean acoustic waves, and tsunamis based on tsunami-coupled equations of motion, *Pure and Applied Geophysics*, *170*(1-2), 109–127.

Maeda, T., T. Furumura, S. Noguchi, S. Takemura, S. Sakai, M. Shinohara, K. Iwai, and S.-J. Lee (2013), Seismic-and Tsunami-Wave Propagation of the 2011 Off the Pacific Coast of Tohoku Earthquake as Inferred from the Tsunami-Coupled Finite-Difference Simulation, *Bulletin of the Seismological Society of America*, *103*(2B), 1456–1472.

Matsumoto, H., S. Inoue, and T. Ohamachi (2012), Some features of water pressure change during the 2011 Tohoku earthquake, *Proceeding of the International Symposium on Engineerng Lessons Learned from 2011 Great East Japan Earthquake, Tokyo, Japan.*

Miyoshi, H. (1954), Generation of the tsunami in compressible water (part i), *J. Oceanogr. Soc. Jpn*, *10*(1-9).

Nosov, M. (1999), Tsunami generation in compressible ocean, *Physics and Chemistry of the Earth, Part B: Hydrology, Oceans and Atmosphere*, *24*(5), 437–441.

Nosov, M., and S. Kolesov (2007), Elastic oscillations of water column in the 2003 tokachi-oki tsunami source: in-situ measurements and 3-d numerical modelling, *Natural Hazards and Earth System Science*, *7*(2), 243–249.

Nosov, M., S. Kolesov, A. Denisova, A. Alekseev, and B. Levin (2007), On the near-bottom pressure variations in the region of the 2003 tokachi-oki tsunami source, *Oceanology*, *47*(1), 26–32, doi: 10.1134/S0001437007010055.

Okada, Y. (1985), Surface deformation due to shear and tensile faults in a half-space, *Bulletin of the Seismological Society of America*, *75*(4), 1135–1154.

Renzi, E., and F. Dias (2014), Hydro-acoustic precursors of gravity waves generated by surface pressure disturbances localised in space and time, *Journal of Fluid Mechanics*, *754*, 250–262, doi:10.1017/jfm.2014.398.

Riccobene, G. (2012), Towards acoustic uhe neutrino detection in the mediterranean sea, *Nuclear Instruments and Methods in Physics Research Section A: Accelerators, Spectrometers, Detectors and Associated Equipment*, *692*, 197–200.

Sammarco, P., C. Cecioni, G. Bellotti, and A. Abdolali (2013), Depth-integrated equation for large-scale modelling of low-frequency hydroacoustic waves, *Journal of Fluid Mechanics*, *722*, R6.

Sells, C. (1965), The effect of a sudden change of shape of the bottom of a slightly compressible ocean, *Philosophical Transactions of the Royal Society of London. Series A, Mathematical and Physical Sciences*, *258*(1092), 495–528.

Shaw, B., et al. (2008), Eastern mediterranean tectonics and tsunami hazard inferred from the ad 365 earthquake, *Nature Geoscience*, *1*(4), 268–276.

Silva, R., P. Salles, and G. Govaere (2003), Extended solution for waves travelling over a rapidly changing porous bottom, *Ocean Engineering*, *30*(4), 437–452.

Simeone, F., and S. Viola (2011), The smo project: a submarine multidisciplinary observatory in deep-sea, in *Mobile Adhoc and Sensor Systems (MASS), 2011 IEEE 8th International Conference on*, pp. 898–903, IEEE.

Stiassnie, M. (2010), Tsunamis and acoustic-gravity waves from underwater earthquakes, *Journal of Engineering Mathematics*, *67*(1-2), 23–32.

Synolakis, C. E., J.-P. Bardet, J. C. Borrero, H. L. Davies, E. A. Okal, E. A. Silver, S. Sweet, and D. R. Tappin (2002), The slump origin of the 1998 papua new guinea tsunami, *Proceedings of the Royal Society of London. Series A: Mathematical, Physical and Engineering Sciences*, *458*(2020), 763–789.

Tinti, S., A. Maramai, and L. Graziani (2004), The new catalogue of italian tsunamis, *Natural Hazards*, *33*(3), 439–465.

Tolstoy, I. (1963), The theory of waves in stratified fluids including the effects of gravity and rotation, *Reviews of Modern Physics*, *35*(1).

Tonini, R., A. Armigliato, G. Pagnoni, F. Zaniboni, and S. Tinti (2011), Tsunami hazard for the city of catania, eastern sicily, italy, assessed by means of worst-case credible tsunami scenario analysis (wctsa), *Natural Hazards and Earth System Sciences*, *11*, 1217–1232.

Van Keken, P., C. Spiers, A. Van den Berg, and E. Muyzert (1993), The effective viscosity of rocksalt: implementation of steady-state creep laws in numerical models of salt diapirism, *Tectonophysics*, *225*(4), 457–476.

Yamamoto, T. (1982), Gravity waves and acoustic waves generated by submarine earthquakes, *International Journal of Soil Dynamics and Earthquake Engineering*, *1*(2), 75–82.

Yamazaki, Y., Z. Kowalik, and K. F. Cheung (2009), Depth-integrated, non-hydrostatic model for wave breaking and run-up, *International Journal for Numerical Methods in Fluids*, *61*(5), 473–497.